PREPARATION AND CHARACTERIZATION OF ZINC TUNGSTATE AND COMPOSITE AS ANODE MATERIAL FOR LITHIUM-ION BATTERY

Thesis

Submitted in partial fulfilment of the requirements for the degree of

DOCTOR OF PHILOSOPHY

By

BRIJESH K

(Register Number: 165141PH16F03)

DEPARTMENT OF PHYSICS
NATIONAL INSTITUTE OF TECHNOLOGY KARNATAKA, SURATHKAL, MANGALORE-575025

May, 2021

PREPARATION AND CHARACTERIZATION OF ZINC TUNGSTATE AND COMPOSITE AS ANODE MATERIAL FOR LITHIUM-ION BATTERY

Thesis

Submitted in partial fulfilment of the requirements for the degree of
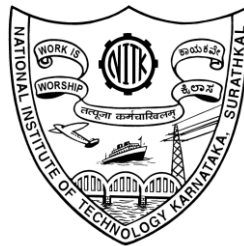
DOCTOR OF PHILOSOPHY

By

BRIJESH K

(Register Number: 165141PH16F03)
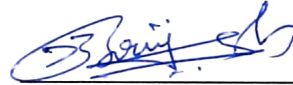
Under the Guidance of

Dr. Nagaraja. H. S

DEPARTMENT OF PHYSICS
NATIONAL INSTITUTE OF TECHNOLOGY KARNATAKA,
SURATHKAL, MANGALORE-575025

May, 2021

DECLARATION

I hereby declare that the Research Thesis entitled **"PREPARATION AND CHARACTERIZATION OF ZINC TUNGSTATE AND COMPOSITE AS ANODE MATERIAL FOR LITHIUM ION BATTERY"** which is being submitted to the National Institute of Technology Karnataka, Surathkal in partial fulfilment of the requirements for the award of the Degree of **Doctor of Philosophy** in **Physics** is a *bonafide report of the research work carried out by me*. The material contained in this Research Thesis has not been submitted to any University or Institution for the award of any degree.

BRIJESH K

(Register No. 165141PH16F03)

Department of Physics

Place: NITK, Surathkal

Date: 22/10/2021

CERTIFICATE

This is to *certify* that the Research Thesis entitled **"PREPARATION AND CHARACTERIZATION OF ZINC TUNGSTATE AND COMPOSITE AS ANODE MATERIAL FOR LITHIUM ION BATTERY"** submitted by **Brijesh K.** (Register Number: **165141PH16F03**) as the record of the research work carried out by him, is accepted as the Research Thesis submission in partial fulfilment of the requirements for the award of degree of **Doctor of Philosophy**.

Dr. H. S. Nagaraja

Research Guide

Department of Physics

NITK, Surathkal

Date:

Chairman-DRPC

ASSOCIATE PROFESSOR & HEAD
Physics Department
NITK Surathkal, Mangalore-575025
KARNATAKA

Acknowledgement

I dedicate my sincere thanks to my research supervisor Dr. H S Nagaraja, Associate Professor, Department of Physics, NITK for providing me an opportunity to pursue research work. His constant inspiration, academic support and motivation are highly appreciated.

I would like to extend my sincere gratitude to the H.O.D, and all other faculty members of Department of Physics, NITK for their support and encouragement. I am also thankful to the non-teaching staff for their technical support. I take this opportunity to thank my RPAC members, Dr. P Parthiban, Associate Professor, Department of Electrical and Electronics Engineering and Dr. Partha Prathim Das, Assistant Professor, Department of Physics, NITK, for their valuable suggestions and critical remarks during progress assessment.

I would like to thank for the assistance of characterization facilities in the Department of physics-NITK, DST-PURSE Mangalore University, BIT Bangalore, STIC-SAIF Cochin, Department of Chemistry, NITK, Department of Chemical Engineering, NITK for providing sophisticated instruments.

I also thank Dr. Bindu K for assisting my manuscript and thesis writing. I thank Kavya K Nayak for help in compiling the thesis. In this small space I would like to thank my friends, lab mates and colleagues notably Dr. Sreejesh M, Amudha A, Dhanush Shanbhag, Mukesh, Laxmi Sagar, Achyutha K, Pavitra Rao, Mahendra, Brian, Bharath SP, Anupriya James, Navaneetha, Nimith KM, Sterin, Khasim, Dr. Sibi, Rizwan, Safir TK, Dhanush, Vinayraj, Sona and Veena for their invaluable help and memorable company.

My deepest gratitude goes to my parents for their everlasting support throughout my thesis work. I am grateful to my parents Kumaran and Shalini for their love, care and support. I also extend my thanks to my sister and brother in-law.

Finally, I conclude with a profusion of thanks to all those who have helped me directly or indirectly in making this dissertation a possibility.

(Brijesh K)

ABSTRACT

The thesis entitled "preparation and characterization of zinc tungstate and composite as anode material for lithium-ion battery" cover the preparation, characterization and electrochemical analysis as anode material for Lithium-ion battery (LIB) of zinc tungstate and their composites ($ZnWO_4/SnO_2$, $ZnWO_4/GeO_2$ and $ZnWO_4/SiO_2$) via solvothermal and microwave method. The structural, elemental and morphological properties of the prepared samples are characterized using x-ray diffraction (XRD), scanning electron microscopy (SEM), energy-dispersive X-ray spectroscopy (EDAX), high-resolution transmission electron microscopy (HR-TEM), Brunauer-Emmett-Teller (BET) measurements, Raman spectroscopy and X-ray photoelectron spectroscopy (XPS) techniques.

Prepared $ZnWO_4$ and $ZnWO_4$@r-GO nanocomposite delivered initial discharge capacity of 746 and 1158 mAh g^{-1} respectively at current density of 100 mA g^{-1} and potential window 0.02 - 3 V versus Li/Li^+ at room temperature. Further, $ZnWO_4/SnO_2$ and $ZnWO_4/GeO_2$ are tested as anode material for LIB. Increasing percentage of SnO_2 increases the specific capacity of the $ZnWO_4/SnO_2$ composite and GO further boosts the specific capacity of the composite. The capacity of the first discharge curve of ZWSN-5, ZWSN-10 and ZWSN-10/GO nanocomposite is noticed as 882, 1316 and 1486 mAh g^{-1} respectively. While in the case of $ZnWO_4/GeO_2$, the initial discharge capacity of ZWGE5, ZWGE10 and ZWGEC nanocomposites were 761, 825, and 930 mAh g^{-1}, respectively. Further, CNT boosts the performance of the $ZnWO_4/GeO_2$ composite.

$ZnWO_4/SiO_2$ is prepared via microwave method and used as an anode material for LIB. The initial charge discharge capacity of the ZWSO5 nanocomposites is 570 and 314 mAh g^{-1} respectively at 10 mA g^{-1}. The discharge capacity of the ZW, ZWSO1, ZWSO2, ZWSO3 and ZWSO4 are 145, 265, 278, 363 and 453 mAh g^{-1} respectively. The increasing amount of SiO_2 in the $ZnWO_4/SiO_2$ composite increases the overall performance of the $ZnWO_4/SiO_2$ composite.

Keywords: Zinc tungstate; hybrid metal oxides; anode material; lithium ion battery; electrochemical studies;

Dedicated to my father, mother and my sister

CONTENT

CHAPTER 5 ZnWO$_4$/GeO$_2$@CNT nanocomposite for lithium ion battery application   83-96

APPENDIX

LIST OF FIGURES

CHAPTER 1

CHAPTER 2

CHAPTER 3

CHAPTER 6

LIST OF TABLES

CHAPTER 1

CHAPTER 2

CHAPTER 3

CHAPTER 4

CHAPTER 6

CHAPTER 7

ABBREVIATIONS

LIB	Lithium ion battery
EES	Electrochemical energy storage
CNM	Carbon based nanomaterials
CNT	Carbon nanotubes
SWCNT	Single-wall carbon nanotubes
MWCNT	Multiwall carbon nanotubes
SCCNTs	Stacked-cup carbon nanotubes
GO	Graphene oxide
rGO	Reduced graphene oxide
XRD	X-ray diffraction
XPS	X-ray photoelectron spectroscopy
FESEM	Field emission scanning electron microscopy
HRTEM	High-resolution transmission electron microscopy
SAED	Selected area electron diffraction
CV	Cyclic voltammograms
EIS	Electrochemical impedance spectroscopy
TGA	Thermogravimetric analysis
GCD	Galvanostatic charge-discharge
EDS	Energy dispersive X-ray spectroscopy
EDLC	Electrochemical double layer capacitance
BET	Brunauer-Emmett-Teller analysis
SOH	State of health

NOMENCLATURE

Z	Complex impedance
Z′	Real part of impedance
Z″	Imaginary part of impedance
h k l	Miller indices
m	Active mass
C_s	Specific capacity
CE	Coulombic efficiency
F	Faraday's constant
Rs	Solution resistance
R_{ct}	Charge-transfer resistance
C_{dl}	Double layer capacitance
W	Warburg impedance

CHAPTER 1
INTRODUCTION

CHAPTER 1

INTRODUCTION

This chapter includes the introduction to the energy storage systems along with types of energy storage systems. And also, contains the fundamentals of nanotechnology, which includes metal oxides and metal tungstates nanomaterials. It also covers the literature survey followed by the scope and objectives of the present thesis.

1.1 ENERGY STORAGE SYSTEMS

The production and storage of energy are very important in the current fast growing, digitized and miniaturized world. Currently, we depend on the fossil fuels for the production of energy which, increase the green-house effect produced by the emission of carbon dioxide (CO_2). Increasing world population demands the higher energy which will increase the CO_2 concentration resulting in the climate warming [1-4]. Thus, we must develop the ways of using of renewable energies like wind, biomass, solar and geothermal for the energy production [5-9]. It is very important to consider how produced energy can be used more efficiently and find reliable conversion also storage of energy with widely applicable and low cost. For this, we need efficient thermo-electrical and photovoltaic systems which convert heat and light into electricity, respectively. To minimize the joule effect, we required electronic conductors like superconductors. Finally, energy storage systems like batteries/supercapacitors to store energy in chemical forms and convert it back to electricity[10,11].

Energy storage systems store energy in different forms such as kinetic, electromagnetic, thermal, electrochemical, pressure, chemical and potential[12,13]. Using output and energy density, the performance of energy storage devices can be defined. Energy storage devices can be differentiated on the basis of charge-discharge efficiency, energy density, eco-friendliness of the devices and life span. To assess the battery efficiency, charge-discharge efficiency plays a major role. The amount of energy that can be stored in a single system per unit volume or per unit weight is known as energy density. Further, life span and eco-friendliness are the important performance elements of energy storage devices[14,15]. In electrochemical energy storage system (EES) is used to store electricity under a chemical form. This storage system benefits from the fact that both electrical and chemical energy share the same carrier, the

electron[16,17]. EES can be attained by the use of electrochemical cells. Basically, any electrochemical cell contains the movements of an electric current from an electronically conducting medium to an ionically conducting medium and back to the electronic medium. So, it consists of two electronic-ionic interfaces at the two electrodes separated by an ionic medium. At the interface, chemical reaction will take place during the passage of direct current from electronic to ionic medium. Chemical reduction reaction will take place at cathode because electrons will enter the cell from the electrode. And also, at anode oxidation reaction will take place due to electrodes at which electrons liberate the cell [18]. This conversion of chemical energy to electrical or vice versa can be done by the electrochemical devices like fuel cells, supercapacitors and batteries[18,19].

1.1.1 Fuel Cell:

Fuel cell is an electrochemical cell that converts the chemical energy into electricity through a pair of redox reaction. A fuel cell consists of anode and cathode surrounded by the electrolyte. In the fuel cell, fuels are conveyed to the anode and oxygen or air (oxidant) to the cathode. Under specific catalytic conditions, fuels are oxidized and oxidants are reduced while, through the external circuit electrons being transferred from anode to the cathode. The anions and cations roam through electrolyte from the cathode to anode and anode to cathode respectively [20-23]. The block diagram of fuel cell is shown in the Figure 1.1.
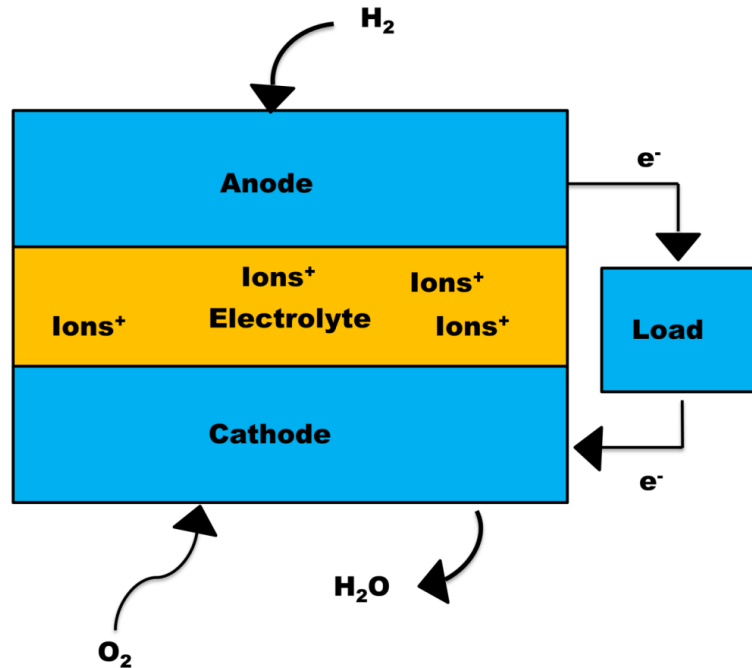
Figure 1.1: Schematic representation of Fuel Cell

Commercial application of fuel cells has some drawbacks to overcome [24-27]

- o Fuel cells are expensive due to platinum based catalyst, mild membrane fabrication techniques and coating and plate material of bipolar plates.
- o Low durability of fuel cell
- o Hydrogen safety concerns
- o Delicate thermal and water management
- o Large system size and weight

Fuel cells provide ultrahigh energy density but are restricted by low power density (slow kinetics) and the necessity of expensive precious metal catalysts[28].

1.1.2 Supercapacitor:

The supercapacitor is also known as double layer capacitor or ultra-capacitor, which differ from the regular capacitor, due to its very high capacitance. A capacitor stores energy by static charge as opposed to an electrochemical reaction [29-31]. In super-capacitors, the energy is stored as adsorbed ionic species at the interface between the porous carbon electrode and the

electrolyte. The ions are quickly delivered to the electrode surface through a liquid electrolyte, and the electrons are rapidly transported through the highly conductive carbon electrode to an external circuit. As a result, supercapacitors typically exhibit rapid charge or discharge behavior with a high power density. However, the total number of ions that can be stored on the surface is limited and thus the overall energy density is low. Supercapacitor can be classified into three types according to their charge storage. They are (1) double layer capacitor (Electrostatically – Helmholtz layer), (2) Pseudo-capacitors (Electrochemically – Faradaically), (3) Hybrid capacitors (Electrostatically and Electrochemically)[32,33]. Block diagram of supercapacitor is represented in the Figure 1.2.

Supercapacitors are mainly used in camera, telecommunications, and electric vehicles. Also, supercapacitor used in the transmission line due to deviations in power demand a storage device become essential. Further, it finds application in UPS and hybrid electric vehicles. There are few disadvantages of supercapacitor for the commercial application [34-37]

- o Energy density is very low
- o Supercapacitor have high self-discharge rate compared to batteries.
- o For some applications, full energy spectrum cannot be used.
- o Low voltage cells (serial connections are needed for high voltage)
- o Voltage balancing needed.
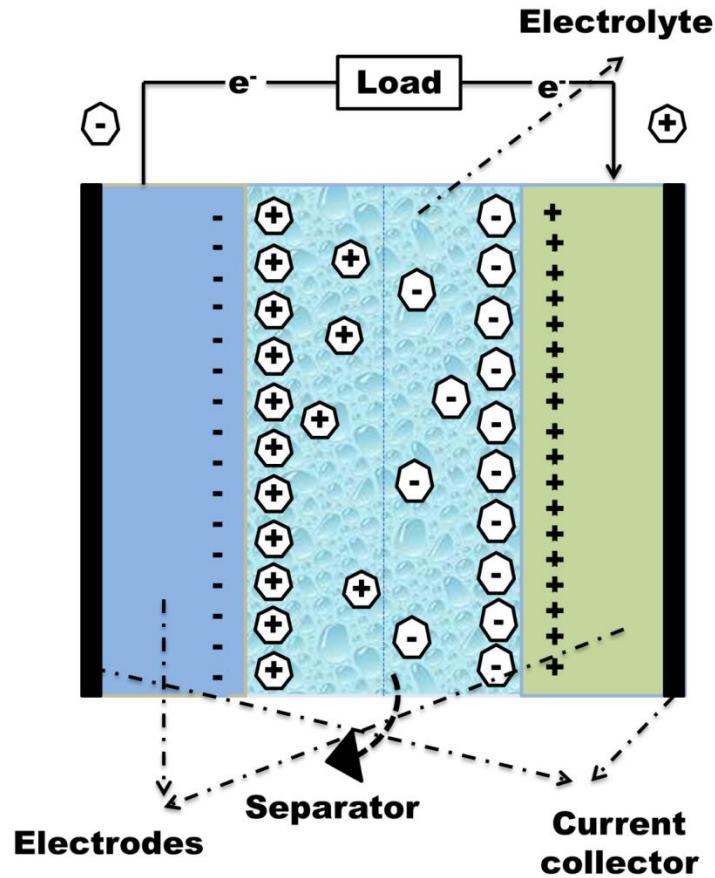
Figure 1.2: Schematic representation of supercapacitor

1.1.3 Batteries:

Finally and importantly batteries, which can store and deliver electrical energy spawned from reversible redox reactions that may transpire in the constituent materials of their electrodes. Battery has cathode (positive plate) and an anode (negative plate) which are separated by a separator and immersed in an electrolyte that allows the ions to pass between the electrodes[38,39]. The block diagram of battery is given in the figure 1.3. Batteries are mainly classified into two types.
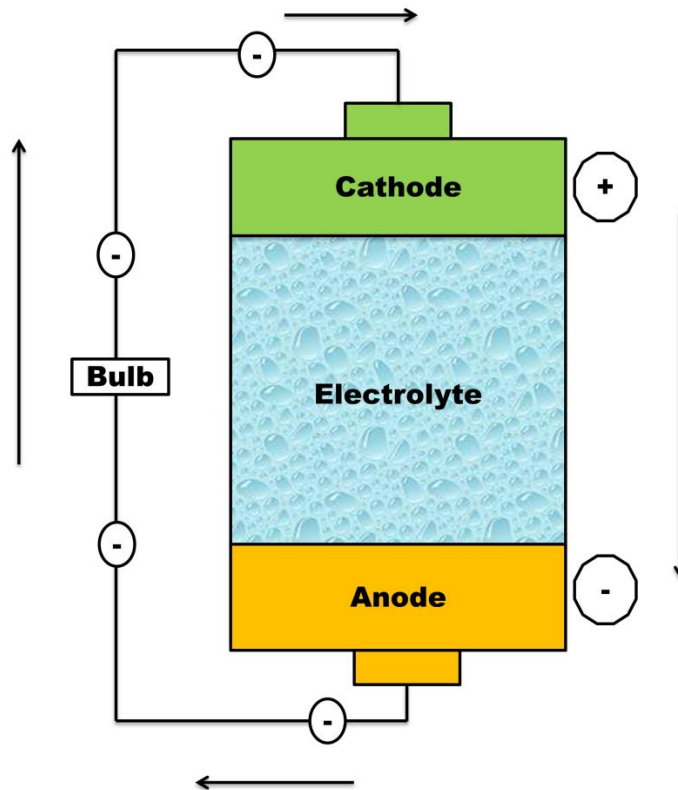
Figure 1.3 Schematic representation of battery

1.1.3.1 Primary batteries:

They are single use cell because they cannot be recharged. Once the cell has exhausted the energy, then the cell would be discarded. Their chemical reactions are not reversible [40,41]. The widely used primary cell is dry cell (zinc-carbon battery).

1.1.3.2 Secondary battery:

Secondary batteries are chargeable. Their chemical reactions can be reversed by applying electric current to the cell. This cell can be used multiple times by charging repeatedly. The examples for secondary batteries are nickel-cadmium (NiCd), lead acid and lithium ion batteries. Among them, Lithium ion batteries are the most popular rechargeable batteries and are widely used in the portable electronic devices. In lithium ion battery, lithium ions transmit from the anode to the cathode during discharge and reverse back when charged. The lithium ion battery consists of three primary functional components; positive (cathode) and negative (anode) electrodes and electrolyte. In general, anode of the conventional lithium ion battery is

6

made from carbon. The cathode is normally metal oxides. The electrolyte typically is lithium salt in an organic solvent [42-44].

Lithium ion operation is same as that of the other rechargeable batteries. During discharge, electrical charge transmits through an external circuit between the electrodes of battery. To balance the charge transfer within the cell, positively charged lithium-ions move through an internal electrolyte circuit between the positive and negative electrodes. During re-charge the process reverses and lithium-ions move back through the electrolyte [45-47]. The schematic of LIB is shown in the Figure 1.4.
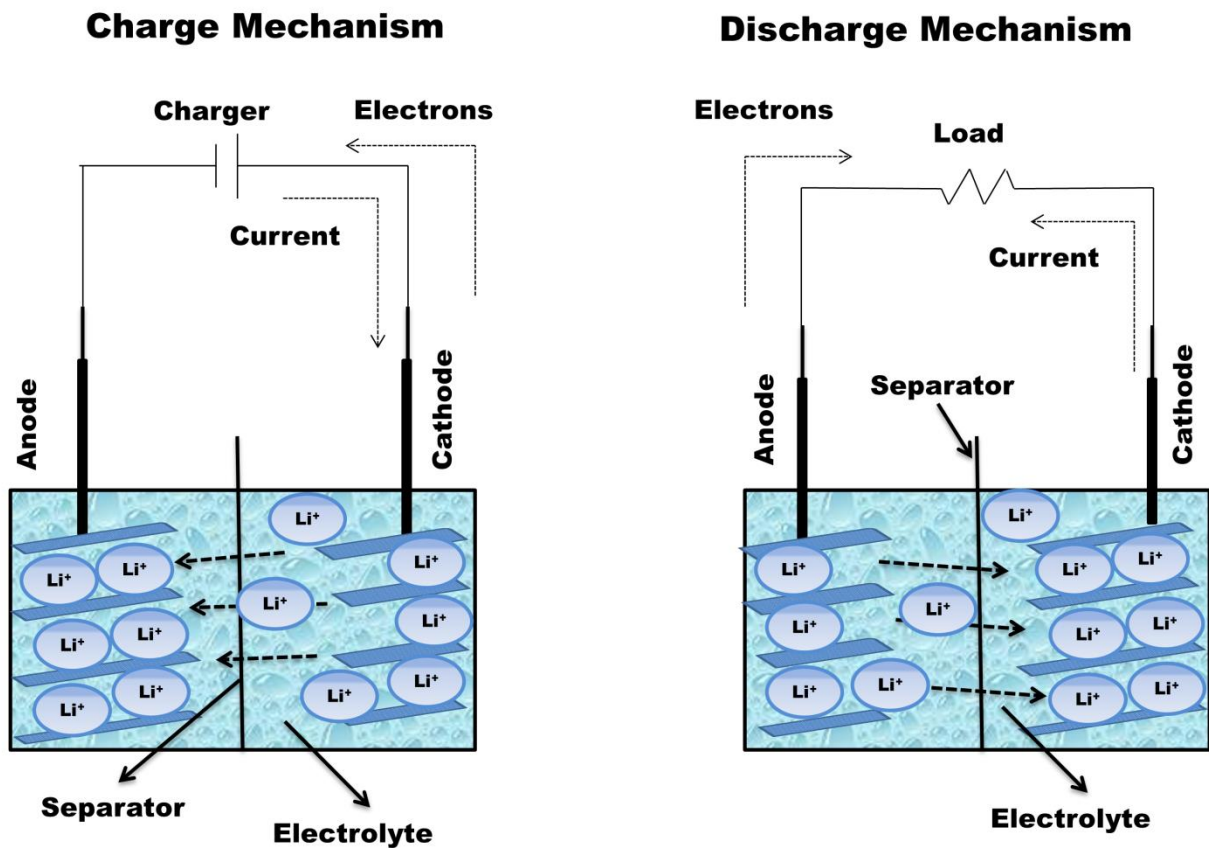
Figure 1.4: Schematic representation of lithium ion battery

The main functional components of lithium ion battery are cathode, electrolyte, separator and anode. Electrodes play major role in the overall enactment of a LIB. Typically, mixture of organic carbonates such as diethyl carbonate or ethylene carbonate containing complex of

7

lithium ions are used as electrolytes for the lithium ion battery. A prominent selection of electrolyte has to contain the following features [48,49]`

- o Chemically compatible with electrodes
- o Stable over the operating potential window
- o Should not allow charge accumulation or polarization
- o Thermally stable
- o Strong ionic conductivity
- o No electric conductivity

Separator, as the name indicates separates the contact between building blocks (anode and cathode) of LIB. Separator promotes the movement of ions from cathode to anode on charge and anode to cathode while discharge. Separator plays a role as an isolator with no electrical conductivity. Separator does not involve in the chemical reaction directly, but it is very essential element which influences the performance like power density and safety of the LIB. The separator should have chemical and thermal stability, mechanical strength and porosity for ionic conductivity [50-52].

To construct a high performance LIB, selection of anode and cathode materials are very important. Cathode is a positive or oxidizing electrode and generally one of these three materials: Lithium cobalt oxide (layered oxide), lithium ion phosphate (polyanion) or lithium manganese oxide (a spinal). To select the cathode material, one should consider the following features [53-56]

- o Stable when in contact with electrolyte
- o Efficient oxidizing agent
- o Easy to fabricate
- o Low cost

Anode is a negative electrode and Graphite is popularly used anode material for the commercial LIB with a theoretical capacity of $372\, mAh\ g^{-1}$[57]. The increasing demand of commercialization of LIBs required anode material with high energy density, high specific capacity, decent rate capability, low-cost and environmental-friendliness. Therefore, searching

for new anode material with notable electrochemical performance and high theoretical capacity is in demand. To select the anode material, following features need to be considered [58-63],

- o High theoretical capacity
- o Good electrical conductivity
- o High mechanical stability
- o High structural stability

During charge/discharge cycles, Li-ion intercalates with the anode and may cause increase in the volume and structural deformation of anode material. To prevent this, porous and nanomaterial are preferred as anode material for LIB [64-67].

1.2 NANOTECHNOLOGY

Nano-science and Nano-technology are the study and application of extremely small things ranging from 1 to 100 nanometers, which are normally labeled as nanomaterials [68-71]. They play an important role in fast growing, digitalized and miniaturized world covering all the fields like medicine, energy generation, electrical and electronics industries etc. due to their unique properties. Today's scientists and engineers are finding a wide variety of ways to deliberately prepare materials at the nanoscale and to take advantage of their enhanced properties such as higher strength, lighter weight, increased control of light spectrum and greater chemical reactivity than their larger-scale counterparts[72,73]. The properties of materials can be different at the nanoscale for two main reasons. First, nanomaterials have a relatively larger surface area when compared to the same mass of material produced in bulk form. This property makes the material chemically more reactive (in some cases materials that are inert in their larger form are reactive, when produced in their nanoscale form), and affect their strength or electrical properties [74-76]. Second, quantum effects can begin to dominate the behavior of matter at the nanoscale - particularly at the lower end - affecting the optical, electrical and magnetic behavior of materials. Nanomaterials can be produced in one dimension, in two dimensions or in all three dimensions [77,78].

The technology for making materials into nano-sized particles has been studied energetically in recent years. Nano-technology has been used to remarkably improve the performance of nano-sized materials. Nanostructured materials have several applications, one among them is

in the field of electrochemistry. Nano structured electrodes showed improved rate capabilities relative to thin-film control electrodes prepared from the same material. Also discharge potential of the nanostructured material become higher than the micro structured material[79,80].

In periodic table more than 75% of elements are metallic in nature such as gold, silver, platinum, mercury, uranium, aluminum, sodium and calcium. Metals are placed on the left side of periodic table. Group 1 to 12 includes alkali metal, alkaline earth metal and transition metals. Generally, metals are shiny solids having high melting points and densities. They have maximum atomic radius in across the period. Due to this, they have low ionization potential and low electronegativity. Due to their malleable and ductile properties, they can be deformed without breaking and drawn into wire. Because of low ionization potential, metals can easily lose electron and hence are good conductors of heat and electricity. Metals can combine with other metal and non-metal to form alloys which are widely used in many industries. Metals can form halides, oxide, carbonate, nitride and other compound with suitable reagent.

1.3 METAL OXIDES

The metallic compounds which are formed with metal and oxygen in the form of oxide ion (O^{2-}) are called as metal oxide. They are named in two words where first word is the name of metal with oxidation number in parenthesis followed by oxide. The formula of metal oxide has to be written in two words; first write the symbol of first element with oxidation number then write symbol of oxygen 'O' with an oxidation number -2[81]. Metallic oxides are basic in nature and often exist as solids at room temperature. Generally, metal oxides are insoluble in water and produce salts with acids. Metal oxides can be classified into alkali metal oxides, alkaline earth metal oxides and transition metal oxides[82]. Metal oxide nanoparticles have found several applications due to their high reactivity, high surface area-to-volume ratio and good size distribution[83]. Metal oxide nanoparticles can show matchless physical and chemical properties than bulk oxides[84]. Over the past decade immense research has been focused on the preparation and characterization of the transition metal oxides and hydroxides due to their unique and wealthy nature for the electrochemical applications. We know that transition metal oxides are generally classified into three categories: (1) Single metal oxides

such as NiO, MnO$_2$, MgO$_2$, CuO$_2$, etc. (2) Binary metal oxides such as ZnWO$_4$, CuWO$_4$, CaO–ZnO, ZnOAl$_2$O$_3$, etc. (3)   Hybrid metal oxide materials such as Ni(OH)$_2$/MnO$_2$, NiWO$_4$/Co$_3$O$_4$,etc. Among these categories, Binary metal oxides and Hybrid metal oxides are synthesized due to their high electrical conductivity and various oxidization states than single metal oxides. The design and synthesis of novel binary transition metal oxides with high electron conductivity and good electrochemical performances are still a research hot spot[85]. Further, binary metal oxides such as tungstate have drawn wide attention for its excellent catalytic and electrochemical characteristics.

Metal tungstate nanostructures with diverse morphologies have received significant research interest in the past years due to their technologically important applications[86]. Metal tungstates with the formula of M(WO$_x$) where M is a bivalent cation, have attracted much attention due to their structure. Based on the nature and ionic radii of the metal ions, the MWO$_4$ type compounds possess a wide range of structure types, namely scheelite, zircon, monazite, anhydrite, baryite, wolframite and various silica analog structure types including a wide variety of related structures[87]. The tungstate usually crystallizes in the tetragonal scheelite structure or in the monoclinic wolframite structure.
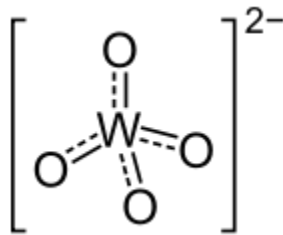
Figure 1.5 Structure of Metal Tungstates

Tungstates of larger cations ($r_A > 0.90$ Å) crystallize in the scheelite type crystal structure (M = Ba, Ca, Eu, Pb, Sr), whereas tungstates of smaller cations ($r_A < 0.90$ Å) crystallize in the wolframite structure (M = Co, Cd, Fe, Mg, Ni, Zn). Every Tungsten atom is surrounded by four oxygen atoms in the scheelite structure while in the wolframite structure six oxygen atoms surround every Tungsten atom[88]. Nanostructures of metal tungstates in different crystal structures including nanorods, nanoparticles, hollow clusters and others can be prepared by physical and chemical methods. Members of oxy-salts of tungsten, such as FeWO$_4$, ZnWO$_4$, MnWO$_4$, CoWO$_4$, NiWO$_4$, and CdWO$_4$ are widely used for electrochemical applications.

Among them, $ZnWO_4$ is also suitable for ion intercalation. However, $ZnWO_4$ anode materials have some disadvantages like, pulverization of electrodes, capacity fading during cycling, poor electrical conductivity and intense volume changes leading to poor rate capability. Therefore, to improve the properties of anode material, researchers have focused on hybrid metal oxide. Some examples showing electrochemical performance of metal oxides as anode material for LIB is listed in the Table 1.1.

Table 1.1 Few metal oxide-based anode material for LIB from literature.

Author and Year	Results	Reference
Jun Chen et al. 2005	The α-Fe_2O_3 nanotubes are prepared by a templating method. The electrochemical reaction of the α-Fe_2O_3 nanotubes is evaluated. The discharge capacity of the α-Fe_2O_3 nanotubes is 1415, 1115, and 890 mAh g^{-1} for 1st, 10th and 20th cycles respectively.	[89]
Hasigaowa Guan et al. 2012	The CoO octahedral nanocages are prepared via simple solution method and tested as anode material for LIB. The first discharge capacity of the CoO octahedral nanocages is 1263.2 mAh g^{-1}. CoO octahedral nanocages shows good cycling performance, enhanced lithium storage capacity and good rate capability.	[90]
Jia Hong Pan et al. 2013	Flowerlike Hierarchical NiO Microspheres synthesized via chemical solution method. The NiO Microspheres delivers 1295 mAh g^{-1} high initial capacity. Hierarchical NiO Microspheres shows high charge discharge capacity and stability than nanoflakes.	[91]
Zachary Favors et al. 2014	SiO_2 nanotubes are prepared via two step hard-template method. SiO_2 nanotubes are used as anode material for lithium ion battery and studied the electrochemical property of the SiO_2 nanotubes.	[92]

	SiO$_2$ nanotubes reveal stable reversible capacity of 1266 mAhg^{-1} after 100 cycles with insignificant capacity fading.	
Yuxin Tang et al. 2014	Bending TiO$_2$–based nanotubes are prepared via stirring hydrothermal process. Prepared elongated TiO$_2$ bending nanotube is used as anode for LIB. Initial charge discharge capacity of the TiO$_2$ nanotube is 368 and 279 mAh g^{-1} at C/4 current density (1 c = 335 mA g^{-1}).	[93]
Hang Su et al. 2015	Hierarchical Mn$_2$O$_3$ hollow microspheres synthesized via solvent-thermal method. The first discharge and charge capacity of hierarchical Mn$_2$O$_3$ hollow microspheres is 1210 mAh g^{-1} and 760 mAh g^{-1} respectively.	[94]
Xin-Yao Yu et al. 2015	Rutile TiO$_2$ submicroboxes are synthesized using a templating method. Rutile TiO$_2$ submicroboxes exhibits 225 mAh g^{-1} discharge capacity and 213 mAh g^{-1} charge capacity in the second cycle. The Rutile TiO$_2$ submicroboxes have improved lithium storage property and stable capacity retention.	[95]
Wenhui Zhang et al. 2016	Prepared ZnO nanocrystals via thermal decomposition method. Compared the performance of commercial available ZnO nanoparticles and prepared ZnO nanocrystals. Prepared ZnO nanocrystals exhibits initial charge/discharge capacity of 709/1563 mAh g^{-1} which is higher than commercial available ZnO nanoparticles. Prepared ZnO nanocrystals showed higher lithium storage capacity than commercial available ZnO nanoparticles.	[96]

Guo-An Li et al. 2016	GeO$_2$ nanoparticles are prepared via optimized sol–gel process. GeO$_2$ nanoparticles produces 982 mAh g^{-1} in 2nd cycle and for 50th cycles it shows 856 mAh g^{-1} with 87% capacity retention.	[97]
Mojtaba Sadati Faramarzi et al. 2018	SnO$_2$ nanoribbons (NRs) are synthesized on catalyst free-SS substrate via vapor-solid (VS) growth approach. SnO$_2$ nanoribbons shows high initial discharge/charge capacity of 1818/929 mAh g^{-1} at 300 mA g^{-1} current density.	[98]
Lifeng Zhang et al. 2018	The MnO$_2$ is prepared via sol-gel method. Prepared MnO$_2$ is used as anode material for LIB. The MnO$_2$ exhibits high capacity of 1000 mAh g^{-1}, high columbic efficiency of 94.5% and 464 mAh g^{-1} at 2000 mA g^{-1} good rate capability.	[99]

1.4 CARBON BASED NANOCOMPOSITES

Carbon nanotubes, fullerenes, graphene, graphene oxide (GO) and mesoporous carbon structures constitute a new class of carbon nanomaterials (CNM) with properties that differ significantly from other forms of carbon such as graphite and diamond. Conventional carbon nanotubes are made of seamless cylinders of hexagonal carbon networks and are synthesized as single-wall (SWCNT) or multiwall carbon nanotubes (MWCNT). Stacked-cup carbon nanotubes (SCCNTs) consisting of truncated conical graphene layers represent a new type of nanotubes.

Carbon nanomaterials generally have high aspect ratio, tensile strength, low mass density, high electric and thermal conductivity, a large surface area and a versatile electronic behavior including high electron conductivity and facilitate the fast electron transfer[100,101]. In metal oxide-CNM nanocomposites, the carbon material either acts as a functional component or a substance for immobilization of other components[102]. In the case of graphene composites, graphene facilitates the mechanical strength, charge transfer and redox reaction, because of its large surface area and conductive structure[103-105]. In the case of carbon nanotube

composites, interaction between CNT and attached nanoparticles contributes to the unique physical and chemical properties. Carbon nano material-metal oxide nanocomposite can be tailored to exhibit electrical, magnetic and optical properties of guest metal oxide nanoparticles, along with the functional properties of carbon nano structure [106-108]. The electrochemical properties of these materials facilitate modulation of their charge transfer properties and aid in the design of catalyst for electrochemical, water splitting, electrodes of supercapacitors and LIB [109-114]. Application of metal tungstates as negative electrodes in lithium-ion batteries are still hindered by two major problems: the high initial irreversible capacity and severe volume expansion during the alloying and de-alloying process of Li–Zn, which leads to poor cycling performance. Hence, finding solution to the problems of poor electronic conduction and volume changes has been a key issue for the research and development of tungstate anode materials [115,116]. Considerable efforts have been devoted to overcome these problems, including the preparation of nano-architectured materials, core–shell structured materials and transition metal oxide/CNM composites, in which the inactive phase serves as a buffer and partly alleviates mechanical stress caused by the volume change of the active phase. Few examples of metal oxide/CNM composites used as anode for LIB listed in the Table 1.2.

Table 1.2 Carbon based composite with metal oxide as anode material for LIB from literature.

Author and Year	Results	Reference
Wei-Ming Zhang et al. 2008	Carbon-coated Fe_3O_4 nanospindles are prepared via hydrothermal treatment method. Prepared Fe_3O_4–C composite is compared with commercial Fe_3O_4 particles and pure a-Fe_2O_3 spindle. The first specific charge capacity of Fe_3O_4–C composite is 749 mAh g^{-1}. The Fe_3O_4–C composite shows better performance than commercial Fe_3O_4 particles and pure a-Fe_2O_3 spindle.	[117]

Yi Zhang et al. 2013	Graphene/α-MnO$_2$ nanocomposites (GMC) are prepared via hydrothermal method and used as anode material for LIB. The GMC produces reversible specific capacity of 998 mAh g^{-1} at 60 mA g^{-1} current density after 30 cycles, and produces rate capabilities of 590 mAh g^{-1} at 12 A g^{-1} current density.	[118]
Huawei Song et al. 2014	The SnO$_2$/MWCNTs hybrid are prepared via hydrothermal treatment method and used as anode for LIB. SnO$_2$/MWCNTs hybrid delivered 800 mAh g^{-1} reversible capacity. The SnO$_2$/MWCNTs composite exhibits long lifespan more than 1000 cycles.	[119]
Yanhong Zhao et al. 2014	The Graphene/ZnO composite with different contents of ZnO is prepared using liquid phase route. The Graphene/ZnO composite delivers specific capacity of 1155.27 mAh g^{-1} at 100 mA g^{-1}.	[120]
Ali Jahel et al. 2014	A nano-GeO$_2$/mesoporous carbon (GeO$_2$/MC) composite material is prepared by a soft templating method. The GeO$_2$/MC composite delivers 1380 and 492 mAh g^{-1} discharge and charge capacity for initial cycle. The GeO$_2$/MC composite retains 93% of its initial capacity after 380 cycles.	[121]
Yufan Ma et al. 2015	NiO/carbon shell/SWCNT composites prepared by heat treating the SWCNT samples synthesized by arc discharge method. The sample delivers 1168.2 and 527.3 mAh g^{-1} initial discharge and charge capacity respectively.	[122]

Wenying Li et al. 2015	The SnO$_2$-RGO composite is synthesized using one-pot route. Prepared SnO$_2$-RGO composite used as an anode material for LIB. SnO$_2$-SRGO composite delivers 1673 mAh g^{-1} and 955 mAh g^{-1} initial discharge and charge capacity respectively which is higher than pure SnO$_2$.	[123]
Xia He et al. 2017	Multichannel carbon fiber with amorphous GeO$_2$ (GeO$_2$/MCNF) are fabricated via electro-spinning method. The GeO$_2$/MCNF produces initial specific discharge and charge capacity of 1101.6 and 718 mAh g^{-1} respectively.	[124]
Ling-hongYin et al. 2017	The SiO$_2$@carbon-graphene (SiO$_2$@C-G) hybrids are prepared via ultrasonic-assisted hydrothermal method. SiO$_2$@C-G delivers the specific discharge capacity of 906 mAh g^{-1} for first cycle. Graphene plays an important role to construct SiO$_2$@C-G, which improves the cyclic performance and structural stability of the composite.	[125]
Min Su Jo et al. 2019	Prepared Coral-Like Yolk–Shell-Structured Nickel Oxide/Carbon Composite Microspheres using spray pyrolysis. The discharge capacity of the CYS-NiO/C is 1124 mAh g^{-1} and charge capacity is 778 mAh g^{-1}. The CYS-NiO/C microsphere exhibits good electrochemical property for Li$^+$ storage, due to their high electrical conductivity and high structural stability.	[126]

Moumita Rana et al. 2019	Synthesized hybrid MnO_2@CNT fabric and used as anode material for LIB. Initial specific capacity of MnO_2@CNTF hybrid is 2175 mAh g^{-1} at 25 mA g^{-1} current density.	[127]

1.5 LITERATURE ON METAL TUNGSTATE AND ELECTROCHEMICAL APPLICATION

The physical parameters (pH, temperature, concentration of the precursor solution and pressure) and preparation method influence the size, structure and performance of the nanoparticles. Zinc tungstate and compounds are used in a verity of fields like electrochemical energy storage, electronic and optical, humidity sensors, photoluminescence and scintillator materials. Among them electrodes for supercapacitor, water splitting and anode for LIB are the current interests of research. Few examples for preparation and high performance electrochemical applications of Zinc tungstates are listed below in the Table 1.3.

Table 1.3 electrochemical applications as anode material of zinc tungstate

Author and Year	Preparation method	Results	Reference
Chen et al. 2003	Synthesized metal tungstates in ethylene glycol (EG, bp=198 °C) with the reaction of $MCl_2 \cdot nH_2O$ (M=Ca, Sr, Ba, Cd, Zn, Pb) and Na_2WO_4 powders in an autoclave at 180 °C under self-generated pressure.	The solvent ethylene glycol played a key role and the reaction temperature also affected the crystallization and purity of the final products. The simplicity of the process and high yield made it suitable for industrial application.	[128]
Parhi et al. 2008	Synthesized a wolframite and scheelite structured tungstates by novel solid state metathetic	They prepared well crystalline phases of scheelite type tungstates, MWO_4 (M = Ca,	[129]

	approach (SSM) (ACl2 +Na2WO$_4$→AWO$_4$ + 2NaCl, A= Ca, Sr, Ba, Zn, Mn, Ni) assisted by microwave energy.	Sr, Ba) have been synthesized where the characteristics of SSM reaction and the formation of high lattice energy by-product NaCl drives the reaction toward completion. Among wolframite-type tungstates, single-phase ZnWO$_4$ is synthesized by SSM reactions at ambient conditions and MWO$_4$ (M = Ni, Mn) are synthesized after subjecting the amorphous product to moderate temperature of heating (around 500 ◦C for 6 h).	
Montini et al. 2010	Tungstates of divalent transition metals (M^{II} WO$_4$, M = Co^{II}, Ni^{II}, Cu^{II}, Zn^{II}) are prepared by reaction of transition metal nitrates with sodium tungstate by simple precipitation method. The precipitates were then calcined at 500 ºC.	ZnWO$_4$ has the largest band gap. ZnWO$_4$ presents the highest photocatalytic activity among the CoWO$_4$, NiWO$_4$ and CuWO$_4$ in the degradation of Methylene Blue（MB) and Methyl Orange (MO) due to their high band gap.	[130]
Hyun-Woo Shim et al. 2011	Wolframite-structure zinc tungstate (ZnWO$_4$) was synthesized using a facile hydrothermal process.	The initial discharge capacity observed was 1140 mAh g^{-1}. They mentioned that, ZnWO$_4$ nanorods exhibits 420 mAh g^{-1} reversible specific capacity	[131]

		after 150 cycles at a rate of C/5. Also mentioned that ZnWO$_4$ nanorods sustained their 1D nanostructure morphologies after 30 cycles.	
Wang Xiao et al 2013	Cuboid like ZnWO$_4$ is prepared by adding Na$_2$WO$_4$ powders into the graphene oxide/Zn aqueous solution followed by a hydrothermal treatment.	The discharge capacity of 566.6 mAh g^{-1} at 100 mA g^{-1} current density is reported for ZnWO$_4$/RGO, which is higher than that for bare ZnWO$_4$. Also, 477.3 mAh g^{-1} capacity is obtained after 40 cycles at a current density of 100 mA g^{-1}.	[132]
Li-Li Xing et al. 2013	SnO$_2$/ZnWO$_4$ core–shell nanorods were prepared by two step method. Initially, ZnWO$_4$ nanorods were synthesized via hydrothermal method. Then, via chemical method ZnWO$_4$ nanorods were coated with SnO$_2$ nanoparticles.	A SnO2/ZnWO4 core–shell nanorod produces high reversible lithium storage capacity. The high lithium storage is due to the synergetic effect between SnO$_2$ and ZnWO$_4$ nanostructure. The reversible capacity of SnO$_2$ nanoparticles activates the electrochemical activity of the ZnWO$_4$ nanorods.	[133]
Bingkun Guan et al. 2013	ZnWO$_4$ nanowall arrays were grown on Ni foam via hydrothermal treatment and used for supercapacitor application.	The ZnWO$_4$ nanowall arrays exhibited decent electrochemical properties with high areal capacitance 1250 F g^{-1} at 10 A g^{-1}. The ZnWO$_4$ nanowall arrays show electrochemical stability and	[134]

		rate property upto 100 mA cm^{-2}.	
Rao et al. 2014	Prepared a graphene oxide (GO) by hummers method. The graphene-Zinc tungstate (GZW) was prepared by a one-pot solvothermal method.	They reported that, GZW shows much higher photocatalytic activity than ZnWO$_4$ for MB degradation under UV light. They conclude that, the enhanced photocatalytic activity was induced by the higher adsorption activity and higher migration efficiency of photo-induced electrons due to the addition of graphene.	[135]
Linsen Zhang et al 2014	Sol-gel method was used to prepare the ZnWO$_4$/CNTs composite.	ZnWO$_4$/CNTs composite exhibits high reversible capacity of 466.9 mAh g^{-1} at 50 mA g^{-1}. And also shows good cycle stability after 50 cycles and superior rate capability.	[136]
Sivasankara Rao Ede et al. 2015	ZnWO$_4$ nanoparticles having aggregated chain like morphology are produced using sodium tungstate salt and zinc nitrate salt in the presence of DNA via microwave irradiation for 5 min.	DNA-ZnWO$_4$ nanoparticles show good electrochemical property with high specific capacitance value ~72 F g^{-1} at 5 mVs^{-1}. And also, they produce 70% specific capacitance after 1000 cycles.	[137]
Yang et al. 2016a	synthesized a zinc tungstate-carbon nanoparticle with a	The prepared zinc tungstate carbon electrode	[116]

	uniform particle size about 10nm by one step hydrothermal reaction using glucose as the carbon source followed by heat treatment at 550ºC	demonstrated a higher initial discharge capacity of 990 mAh g^{-1} when compared to a pure zinc tungstate electrode with a current density of 50 mA g^{-1}. They concluded that, the zinc tungstate–carbon nanoparticles provided significantly improved cycling stability compared to pure zinc tungstate, this implies it is a promising anode candidate for lithium-ion batteries.	
Yang et al. 2016b	Synthesized a new three-dimensional (3D) nanoporous $ZnWO_4$ nanoparticles with WCl_6 and $Zn(NO_3)_2 \cdot 6H_2O$ as the precursors by electro-spinning through a simple and facile progress of electro-spinning.	The 3D nanoporous $ZnWO_4$ nanoparticles(3DN $ZnWO_4$) were used as the electrode for supercapacitor application, and the electrochemical performance was analyzed, indicating the 3DN $ZnWO_4$ supercapacitor is an ideal electrode material with an outstanding cycle, high specific capacitance and excellent rate capacitance, especially it can resist a high current charge and discharge with a little capacitance fading(specific capacitance decreases only 10% with the	[138]

		current density being increased from 40 A g^{-1} to 100 A g^{-1}).	
Shi Nianxiang et al. 2016	Hydrothermally synthesized ZnWO$_4$ hierarchical hexangular microstars. Calcinated the obtained powder at 500 °C for 2 h in Ar atmosphere.	The ZnWO$_4$ HHMs exhibits 777 and 585 mAhg^{-1}, discharge and charge capacity respectively. Concluded that, after calcination, ZnWO$_4$ HHMs shows good rate performance and cyclic stability compared to previous reports.	[139]
Luo et al. 2017	Synthesized hybrid hierarchical CO$_3$O$_4$@ZnWO$_4$ core/shell nanowire arrays (NWAs) on nickel foam through a simple two-step hydrothermal method followed by the heat treatment.	Prepared composite was used as electrode material for the supercapacitor and it shows a high areal capacitance 4.08 F cm^{-2} (1020.1 F g^{-1}) at the current densities of 2 mA cm^{-1} and excellent cycling stability (99.7% of its initial capacitance remain after 3000 cycles). They conclude that, the superior electrochemical performance is because of its unique core/shell nanostructures and synergistic effects between CO$_3$O$_4$ and ZnWO$_4$ materials. The prepared CO$_3$@ZnWO$_4$ hybrid electrode material is suitable for supercapacitor	[140]

		and other energy storage devices.	
Tarugu Anitha et al. 2019	Cauliflower-like $ZnWO_4@WS_2$ composite was prepared on the Ni foam surface by two step hydrothermal method.	The cauliflower like $ZnWO_4@WS_2$ composite exhibits an extremely large specific capacitance of 1280.7 $F\ g^{-1}$ at 3 A g^{-1}, due to their structural stability, electrical conductivity and strong synergetic effects of $ZnWO_4$ and WS_2. The authors claim that, $ZnWO_4@WS_2$ composite have extremely large specific capacitance and excellent cyclic stability than that of $ZnWO_4$ electrode.	[141]
J. Yesuraj et al. 2019	$ZnWO_4$ nanomaterials have been produced through DNA template approach with variable hydrothermal reaction time.	The $ZnWO_4$ nanomaterial revealed high specific capacitance value of 552 Fg^{-1} at 5 mVs^{-1} and 91% capacitance retention after 2000 cycles at a scan rate of 100 mVs^{-1} shows good cyclic stability.	[142]

1.6 SCOPE AND OBJECTIVES

Zinc tungstates are very good material for electrochemical application because both Zn and W are electrochemically active materials. Tungstate oxide is a good pseudo capacitive material due to its high conductivity and high specific area. Tin oxide and Germanium dioxide are also good electrochemical active materials. The composite Tin oxide and Germanium dioxide

enhances the electrochemical properties. There are few works regarding hybrid metal oxide composite with $ZnWO_4$ for electrochemical applications. The thorough electrochemical property of the Tin oxide/Zinc tungstate and Germanium dioxide/Zinc tungstate along with carbon nanotubes needs to be studied. This thesis discusses about Zinc tungstate nanomaterial, hybrid metal oxide ($ZnWO_4/SnO_2$, $ZnWO_4/GeO_2$ and $ZnWO_4/SiO_2$) and carbon composite as anode material for lithium ion battery.

1.6.1 Objectives

Proposed objectives are,

1. Preparation of nanostructured transition metal oxides using hydrothermal or solvothermal method.

2. Preparation of transition metal oxide – CNM composites.

3. To study the structural, compositional and electrochemical properties of prepared composites.

4. To study the electrochemical applications for energy devices like battery and supercapacitor of the prepared composite samples.

1.7 OUTLINE OF THE THESIS

Chapter 1: This chapter gives an introduction to energy storage systems, electrode material, zinc tungstate nanomaterial and carbon nanocomposites and their applications. The detailed literature review on Zinc tungstate material and their applications in supercapacitor and lithium ion batteries are also included in this chapter.

Chapter 2: In this chapter we included the preparation, experimental and characterization procedure.

Chapter 3: The preparation of zinc tungstate and r-GO composite via solvothermal method and application as anode material for lithium ion batteries are discussed in this chapter in detail.

Chapter 4: This chapter includes the preparation of $ZnWO_4/SnO_2$ nanocomposite and $ZnWO_4/SnO_2@r$-GO nanocomposite using solvothermal method, their electrochemical properties and application in anode material for lithium ion battery discussed.

Chapter 5: In this chapter, preparation of $ZnWO_4/GeO_2$ nanocomposite and $ZnWO_4/GeO_2@$ CNT nanocomposite via solvothermal method and detailed study of electrochemical property of the same are discussed.

Chapter 6: This chapter contains the preparation and characterization of hybrid metal oxides ($ZnWO_4/SiO_2$ nanocomposite) using microwave radiation method and their use as anode material for lithium ion battery.

Chapter 7: This chapter covers overall Summary and conclusions along with the future directions.

CHAPTER 2

EXPERIMENTAL METHODS
AND CHARACTERIZATION

CHAPTER 2

EXPERIMENTAL METHODS AND CHARACTERIZATION

This chapter contains detail of various experimental techniques used in the present work. A brief introduction of the solvothermal method which is used to prepare the zinc tungstate nanomaterial and hybrid nanocomposite material is provided. Techniques like X-ray diffraction (XRD), Thermogravimetric analysis (TGA), X-ray photo-electron spectroscopy (XPS), scanning electron microscopy (SEM), high-resolution transmission electron microscopy (HRTEM) and Brunauer-Emmett-Teller (BET) surface area analysis are used for material characterization. For electrochemical studies, cyclic voltammetry (CV), galvanostatic charge-discharge (GCD) and electrochemical impedance spectroscopy (EIS) were used. Preparations of electrode materials are also briefly discussed in this chapter.

Table 2.1 The chemicals used in the present work, along with chemical formula and production company

Chemical Name	Chemical formula	Company
Sodium tungstate dihydrate	$Na_2WO_4 \cdot 2H_2O$	Merck
Zinc acetate dihydrate	$Zn(CH_3COO)_2 \cdot 2H_2O$	Sigma Aldrich
Ethylene glycol	$C_2H_6O_2$	Loba
Tin(IV) chloride pentahydrate	$SnCl_4.5H_2O$	Sigma Aldrich
2-propanol	$(CH_3)_2CHOH$	Sigma Aldrich
Sodium hydroxide	NaOH	Sigma Aldrich
Germanium (IV) oxide	GeO2	Sigma Aldrich
Single walled carbon nanotube	SWCNT	Sigma Aldrich

2.1 PREPARATION METHODS

In obtaining good quality $ZnWO_4$ and its composite, conditions of the experiment and preparation method play an important role. The morphology, structural, chemical and physical properties of the $ZnWO_4$ and its composite depends on the preparation methods. By the proper selection of preparation method and parameters control, one can obtain the nanoparticles with desired properties. In this entire work, we have selected solvothermal method and microwave radiation method to prepare the $ZnWO_4$ and its composite due to their ease of synthesis of desired morphologies.

2.1.1 Solvothermal method

The term "hydrothermal" usually refers to any heterogeneous reactions in the presence of aqueous solvents or mineralizers under high pressure-high temperature conditions to dissolve and re-crystallize materials that are relatively insoluble under ordinary conditions. In the hydrothermal method the components are subjected to the action of water, at temperatures considerably above the critical temperature of water ($370^{o}C$) in closed bomb, and therefore under the corresponding high pressures developed by such solutions. If the solvent used is other than the water, the method is known as "solvothermal" synthesis[143].

Normally, hydrothermal and solvothermal reactions are conducted in a specially sealed container or high-pressure autoclave under subcritical or supercritical conditions of solvent.

Figure 2.1 Teflon jar and stainless steel jacket for solvothermal reaction

Solvothermal method has several advantages over other methods of nanomaterial synthesis such as low reaction temperature and ease of synthesis of desired morphologies, just by changing the parameters like, pH, temperature, pressure, precursor, etc. Highly pure phase can be synthesized using this method. Contamination level is lower compared to other methods.

The image of solvothermal reactor used in our work was presented in the Figure 2.1. We used 120 ml solvothermal reactor for our entire study. We maintained the temperature for experiment at 180 °C.

2.1.2 Microwave method

The microwave-assisted method is widely used in synthesizing Binary Transition Metal Oxides (BTMOs) as a fast synthetic technique. The heating and driving chemical reactions by irradiating microwave have become an obligatory method in modern organic as well as inorganic synthesis, which can dramatically reduce reaction times from days and hours to minutes and seconds. In particular, in the synthesis of BTMOs, microwave-assisted method has the advantage of controlled heating. This is beneficial for the formation of nanostructured materials, whose growth is highly sensitive to the reaction conditions. Moreover, microwave-

assisted method can suppress side reactions and provide rapid kinetics of crystallization. Microwave-assisted routes have been applied for the one-pot synthesis of a large variety of bimetallic oxide nanoparticles and nanostructures, due to rapid volumetric heating, higher reaction rate, reducing reaction time and increasing yield of products, compared with conventional heating methods. However, the morphology and the phase of BTMOs are difficult to control in microwave-assisted synthesis[144].

In this work, commercially available Samsung microwave oven of frequency 2.45 GHz (domestic purpose) with power range of 100 W -750 W was used. The photograph of microwave oven used in the present work is presented in Figure 2.2.

Figure 2.2 Commercial Samsung microwave oven used in the experiment

2.2 CHARACTERIZATION TECHNIQUES

Various techniques are used to study the structural, compositional, morphological, and functional properties. The instrument details and parameters that are used to characterize the samples are briefly discussed below.

2.2.1 Structural, Morphological and Chemical characterization techniques

2.2.1.1 X-ray diffraction (XRD) spectroscopy:

X-ray diffraction technique is used to observe the structural property of the prepared materials. Subsequently, this technique is used to measurement of crystallite size, chemical analysis and internal stress and strain investigation. The diffraction of X-ray is followed by the Bragg's Law,

$$2d\ sin\theta = n\lambda \qquad\qquad (2.1)$$

Where, d is the inter-planar distance, θ is the reflected angle, n is the order of reflection and λ is the X-ray wavelength. The crystal structure of the all samples were analyzed using Rigaku miniflex600 XRD instrument by Cu Kα radiation in the 2θ range 10–80° at scan rate of 2° min[-1]. The X-ray generator is set to 40 kV voltages and 10 mA current. Using Xpert High score plus software the XRD patterns of the all samples were analyzed with reference to ICCD cards.

2.2.1.2 Thermo-gravimetric analysis (TGA):

The thermo-gravimetric analysis is very important and widely used thermal analysis technique to understand the property of material as function of applied temperature. In TGA, the mass of the sample is measured as a function of temperature or time in a controlled atmosphere. The change in the mass on increasing temperature can be attributed to the physical or chemical changes in the material. TGA helps us to find out the thermal stability, melting point, transition temperature of the material.

The weight percentage of the carbon content was measured using thermo-gravimetric analysis (TGA) using a Hitachi Exstar TGA/DTA 6300 for $ZnWO_4$@r-GO nanocomposite explained in the chapter 3. And also, Hitachi-STA7200 is used for ZWSN-10/GO nanocomposite which is explained in the chapter 4. Further, PerkinElmer TGA4000 was used for ZWGEC nanocomposite explained in Chapter 5. TGA of all samples are performed from room temperature to 700 °C in the presence of ambient air.

2.2.1.3 Raman spectroscopy:

Raman spectroscopy is used to notice the various crystalline parameter and frequency mode of the samples. In the present work, Raman spectra are recorded with Peek-Seeker Pro (PRO-785E) Raman system with excitation wavelength of 785 nm laser with a laser spot of 100 micron for ZWSN-10/GO nanocomposite. The Raman spectra of ZWGEC nanocomposite are recorded with LabRAM HR (Horiba) system.

2.2.1.4 X-ray photo-electron spectroscopy (XPS):

X-ray photo-electron spectroscopy is very useful and important characterization technique, which provides the evidence of the composition, bonding state and elements of the sample. Different chemical elements within the near surface are recognized on the basis of their binding energy (BE). In the present work, Kratos Axis Ultra with mono-chromatic Al Kα as X-ray source was used to characterize the $ZnWO_4$@r-GO nanocomposite. Shirley background available along with instrument was used to subtract the background. Thermo Scientific   K-Alpha, X-ray plus photoelectron spectroscopy (XPS) with micro-focused monochromatic Al-Kα as X-ray source was used to determine the ZWSN-10/GO nanocomposite.

2.2.1.5 Brunauer, Emmett and Teller (BET) surface area analysis:

The specific surface area, pore diameter, and pore volume of the samples were estimated using Brunauer-Emmett-Teller (BET) method from the nitrogen adsorption-desorption isotherms. This works on the basis of physical adsorption of a gas on the solid surface. The amount of gas adsorbed on the surface as a monolayer can be used to determine the specific surface area of the solid. It is also dependent on the temperature, pressure and the interaction of the gas with the surface. In the present work, Quanta Chrome Novae-2200 Instrument is used for the BET measurement of the samples.

2.2.1.6 Field Emission scanning electron microscopy (FESEM) and Energy-dispersive X-ray spectroscopy (EDAX):

SEM is a versatile instrument, which can be used for the elemental analysis and chemical state analysis along with simple morphological observation. The electron beam in SEM scans in a raster pattern and the signals detected are combined with the position of the beam to produce the image.

The morphology of the samples is identified using Field Emission scanning electron microscopy (FESEM). The JEOL Model JSM - 6390LV and ZIESS FESEM are used to analyze the ZWGEC nanocomposite with 20 kV accelerating voltage. EDAX is a technique used to examine the elemental composition of the material. EDAX measurements are based on the interaction of electron beam with the specimen, thus producing characteristic X-rays. EDAX measurements provide qualitative information of atomic and weight percentages of all the elements present in the sample. Energy-dispersive X-ray spectroscopy (EDAX) is used for elemental analysis of the samples using OXFORD XMX N.

2.2.1.7 High-resolution transmission electron microscope (HRTEM):

TEM is very important instrument and can be used to study the plane arrangement and core structure of the sample. In TEM, the electron beam passes through the specimen to form a microscopic image. The high resolution lattice fringes of the samples were identified using high-resolution transmission electron microscope (HRTEM) using a JEOL JEM-2100 machine with an operating voltage of 200 kV. SAED pattern and interplanar spacing are also identified using a HRTEM.

2.3 ELECTROCHEMICAL CHARACTERIZATION:

To study the electrochemical property of the samples via cyclic voltammetry (CV) and electrochemical impedance spectroscopy (EIS), Biologic SP-150 electrochemical workstation was used. The charge/discharge of the samples were characterised using a NEWARE BTS4000 battery analyser. A photograph of SP-150 electrochemical workstation and NEWARE BTS4000 battery analyser is presented in the Figure 2.3.
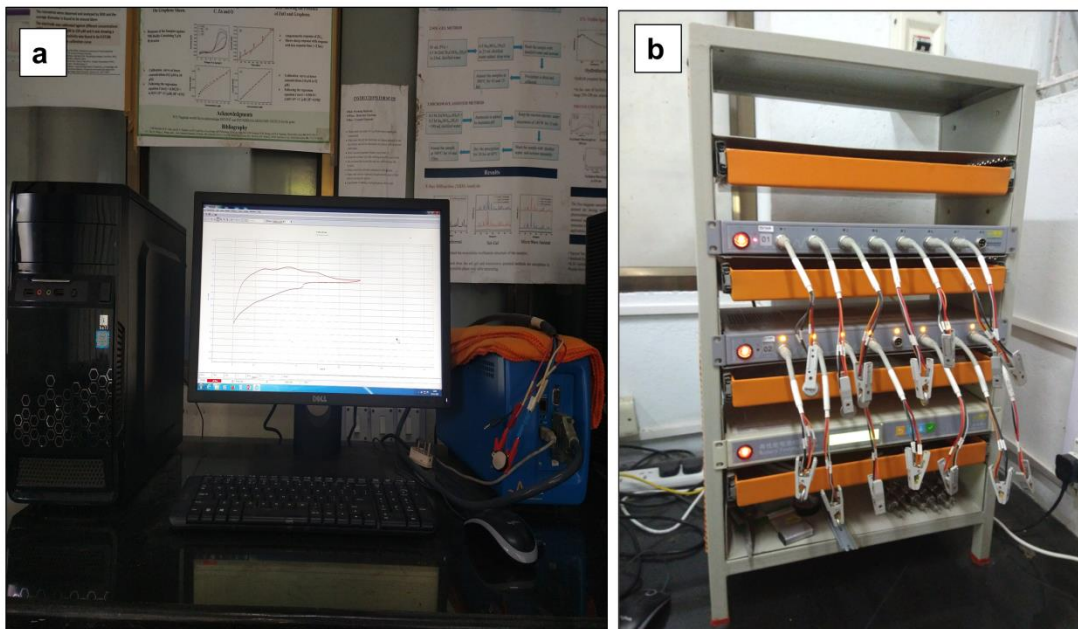
Figure 2.3 (a) Image of Biologic SP-150 workstation (b) NEWARE BTS4000 battery analyser

2.3.1 Cyclic Voltammetry (CV):

To study the electrochemical properties of the samples, CV was performed. The current between counter electrode and working electrode and the potential between reference electrode and working electrode are measured. The rate of change of voltage with time during each phase is known as scan rate. The curve of current versus potential is known as cyclic voltammogram. Cyclic voltammetry provides information about the kinetics of the reaction and the redox potential of the electro active species in the system. The important parameters of a CV are peak currents i.e., anodic peak current (I_{pa}) and cathodic peak current (I_{pc}) and peak potentials i.e. anodic peak potential (E_{pa}) and cathodic peak potential (E_{pc}).

In the present work, for $ZnWO_4$@r-GO nanocomposite and ZWSN-10/GO nanocomposite, the CV was performed at a scan rate of 0.1 mV s^{-1} in the voltage range 0.02 to 3 V versus Li/Li$^+$ which is explained in the chapter 3 and 4. For ZWGEC nanocomposite, CV was performed at 1 mV s^{-1} in the voltage range of 0.01–3V versus Li/Li$^+$, which is explained in the chapter 5.

34

2.3.2 Electrochemical Impedance Spectroscopy (EIS):

The Electrochemical Impedance Spectroscopy (EIS) is broadly used as standard characterization technique for many applications like, corrosion phenomena, batteries and fuel-cells. EIS can provide not only the detailed kinetic information, but also the changes in battery properties under different usage or storage conditions. EIS is a very sensitive technique, and offers a wealth of information about battery systems such as:

> ➢ analysis of state of charge
> ➢ reaction mechanisms
> ➢ change of active surface area during operation
> ➢ separator evaluation
> ➢ passivating film behaviour
> ➢ separation and comparison of electrode kinetics on each electrode
> ➢ identification of possible electrode corrosion processes
> ➢ investigation of the kinetics at each electrode

To study the kinetics and electrochemical behaviour of the as prepared nanocomposites, EIS was performed in the frequency range of 1 mHz to 50 kHz.

2.3.3 Galvanostatic Charge-discharge (GCD):

Galvanostatic charge-discharge is an electrochemical technique used to study the mechanism and kinetics of an electrochemical reaction, along with the estimation of electrochemical capacitance of a material under the controlled current conditions. In GCD, a constant current is applied to the system to charge device, and when the device reaches the cut-off potential, it will be discharged with negative current. The potential versus time curves obtained with this technique can be used to estimate the capacity of the energy storage device. Multiple charge-discharge cycles can be studied to understand the stability and coulombic efficiency of the device. In our studies, GCD was performed with different current density and potential window.

2.3.4 Electrode preparation and construction of anode material for LIB

Preparation of electrodes
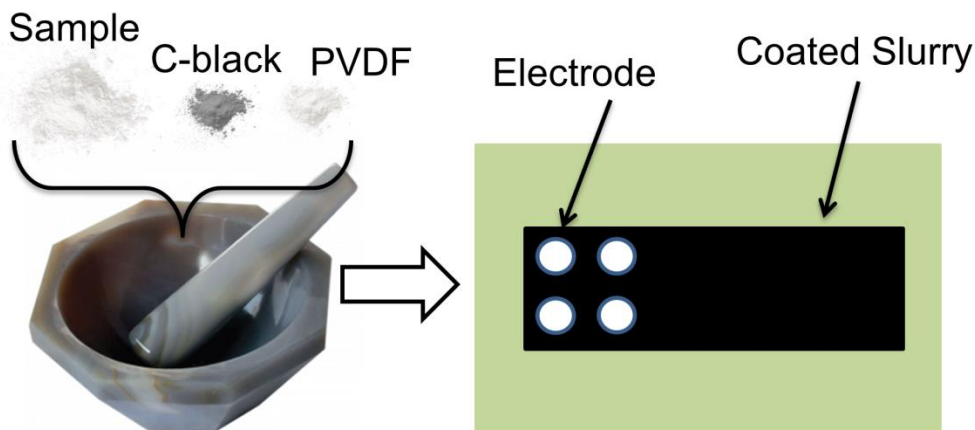
Figure 2.4 Schematic representations of slurry preparation and electrode coating

The electrochemical analysis of the prepared samples was carried out using CR2032 type coin cells assembled in glove box filled with argon gas. The synthesized samples were used as working electrode, lithium foil as counter electrode, 1 M $LiPF_6$ electrolyte in 1:1 volume ratio of ethylene carbonate (EC) and dimethyl carbonate (DMC), and CELGARD 2324 PP Separator to assemble the coin cell. To prepare the working electrode, copper foil was coated by slurry containing prepared samples, and polyvinylidene fluoride (PVDF) and carbon black with different molar ratio with a little quantity of N-methyl-2-pyrrolidone (NMP). The schematic representation of slurry preparation is showed in Figure 2.4. The coated copper foil is dried at 120 °C overnight in a vacuum oven. Copper foil and lithium chip are cut into 16 mm diameter circular shape disc and separator is cut into the 18mm diameter disc. The cell fabricated using the cut disc and few amount of electrolyte. The schematic representation of coin cell fabrication is showed in Figure 2.5.

Coin Cell Fabrication

Anode: Coated Cu foil
Counter electrode: Li metal
Separator: CELGARD 2324 PP
Electrolyte : 1 M LiPF$_6$ in 1:1 volume ratio of dimethyl carbonate (DMC) and ethylene carbonate (EC)
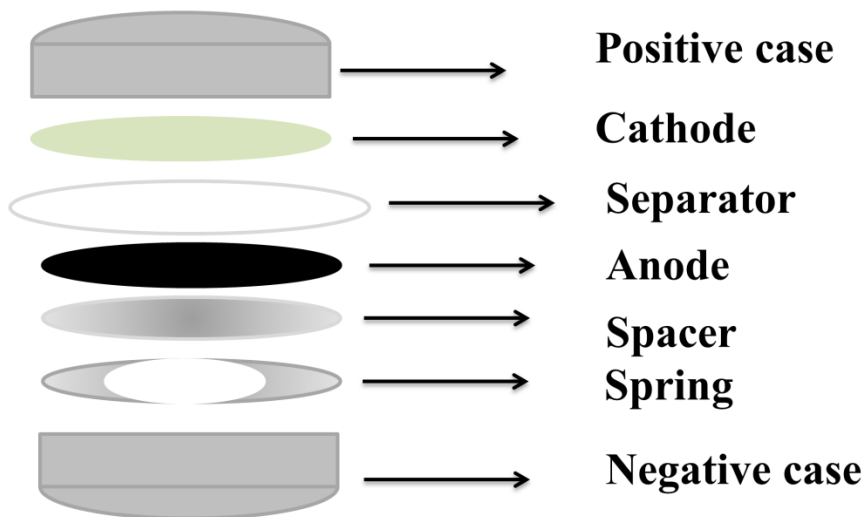
Figure 2.5 Schematic representation of the coin cell preparation

Instruments used in the lab setup for LIB fabrication and assembly in the present work are represented in the Figure 2.6. Figure 2.6 (a) shows the Sartorius BSA224S-CW electronic weighing balance used for present work. Figure 2.6 (b) is Vacuum oven used as heating zone for present work. Figure 2.6 (c) is the Automatic Electrode Film Coater used for the coating of the electrode material in the present work. For the fabrication of LIB, CR2032 coin cells are used and assembled in the argon filled MBruan glove box shown in the Figure 2.6 (d). Figure 2.6 (e) represents the prepared half-cell in this work.
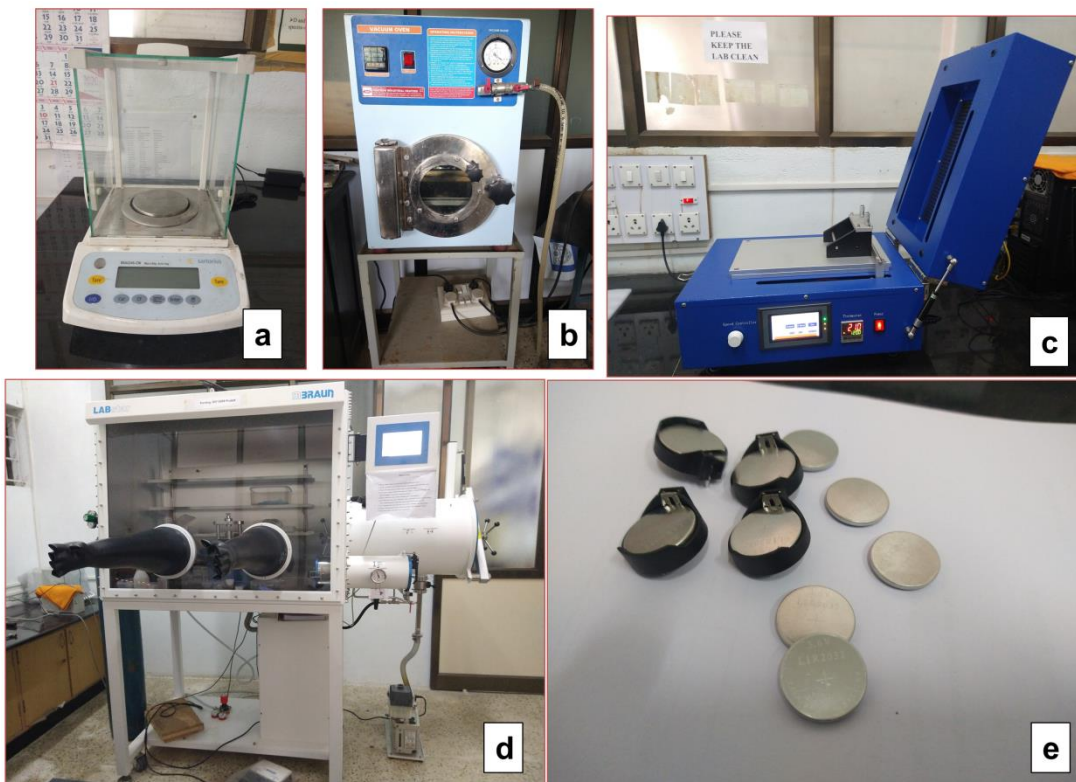
Figure 2.6 (a) Sartorius BSA224S-CW electronic weighing balance, (b) Vacuum oven, (c) Automatic Electrode Film Coater, (d) MBruan glove box and (e) Prepared CR2032 Coin cells.

2.4 PARAMETERS USED TO EVALUATE THE BATTERY PERFORMANCE

There are several important parameters to evaluate the performance of the LIB, few among them are listed below,

2.4.1 Capacity (C_s):

Capacity refers to specific capacity, indicating charge per mass (mAh g^{-1}). Specific capacity measures the amount of charge that can be reversibly stored per unit mass. Specific capacity is closely related to number of electrons released from electrochemical reactions and the atomic weight of the host[145].

$$Specific\ capacity\ (Cs) = \frac{(N \times F)}{(Atomic\ weight \times m)} \qquad (2.2)$$

Where, N = Valence of the Material,

 F = Faraday constant = 96485 Coulombs/Mole.

If this has to be expressed in terms of current, divide that by 3600

F = 26.801Ah/Mole.

m = active mass loaded in the electrode

2.4.2 Cycle life:

Cycle life of a battery refers to how many complete charges and discharges that a rechargeable battery can undergo, after which it cannot perform the required functions.

2.4.3 Capacity retention:

Measure of the capacity of a battery to retain stored energy during an extended open circuit rest period is known as capacity retention. Capacity retention of the cell is affected by the design of the cell.

2.4.4 Columbic efficiency (CE):

Columbic efficiency is also called as Faradic efficiency or current efficiency, which defines the charge efficiency by which electrons are conveyed in batteries. CE is the ratio of the total charge removed from the battery to the total charge put into the battery over a full cycle. Columbic efficiency (CE) is usually used to estimate the cycling life of LIB because CE reflects the loss of Li^+ during each cycle[146].

By definition, CE is the ratio of discharge capacity over charge capacity of a specific electrode in a cell.

$$CE = \frac{Discharge\ capacity}{Charge\ capacity} \qquad (2.3)$$

2.4.5 Electrochemical Impedance Spectroscopy (EIS):

To study the kinetics of the electrode material, Electrochemical Impedance Spectroscopy (EIS) was performed. The Nyquist plot (Z' Vs. –Z'') of the prepared half-cell was recorded. Generally, Nyquist plot consists of a semicircle in the medium higher frequency region and an oblique line in the lower frequency region. The reaction resistance of the SEI layer and charge transfer resistance is the reason for the semicircle. Solid- state diffusion of lithium ions in active material is associated with the line in low frequency region.

The schematic representation of Nyquist plot is represented in Figure 2.7 and process can be interpreted as follows.

Region I: The high frequency region in the Nyquist plot is due to the fastest mass transfer, which is Li^+ diffusion through separator and electrodes within the liquid electrolyte resulting solution resistance.

Region II: This section contains two semicircles. The reaction resistance of the SEI layer and charge transfer resistance is the reason for the semicircle. The second semi-circle depends additionally on the state of health (SOH) of the cell and continuously increases during cycling. This is attributed to structural defects in the electrode materials and the increase in the SEI layer thickness during cycling since its formation with the first charging of the cell

Region III: The moderate mass transfer process is the solid-state Li-diffusion in the active material of the electrodes at very low frequencies. When the concentration gradient fades in the solid material, this section transforms into a capacitive behaviour[147].
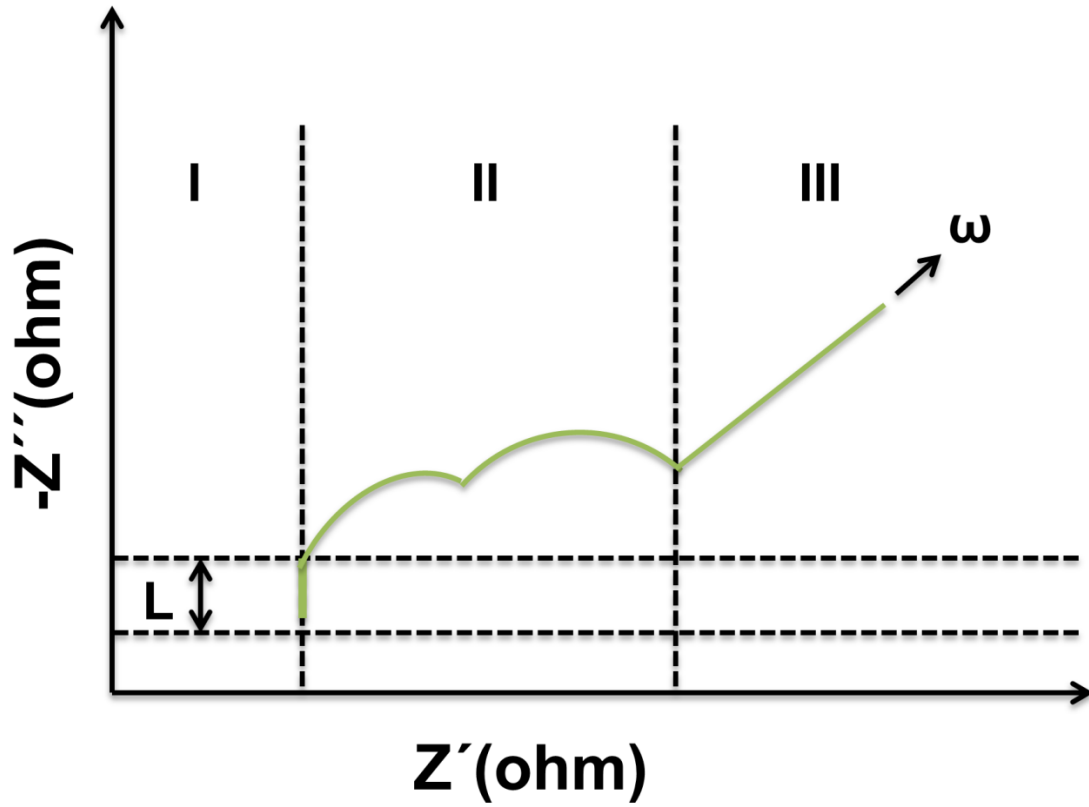
Figure 2.7 Schematic representation of Nyquist plots of the EIS of a LIB

CHAPTER 3

ZnWO$_4$@r-GO NANOCOMPOSITE

A NEGATIVE ELECTRODE FOR LITHIUM-ION BATTERY

CHAPTER 3

ZnWO₄@r-GO NANOCOMPOSITE A NEGATIVE ELECTRODE FOR LITHIUM ION BATTERY

This chapter includes the preparation, structural, morphological characterization and detailed electrochemical studies of the zinc tungstate ($ZnWO_4$) and $ZnWO_4$@r-GO nanocomposite using solvothermal method. Entire chapter concentrates on the effect of the r-GO in the $ZnWO_4$ composite and the synergetic effect of r-GO and $ZnWO_4$ to enhance the performance of the composite. The applicability of the $ZnWO_4$@r-GO nanocomposite as an anode material for LIB is demonstrated.

3.1 INTRODUCTION

The need for more energy is a never-ending quest. This can be tackled by introducing new sources of power or efficient usage of existing power. The current storage devices have their own limitations; however, it is possible to subdue it leading to better storage devices. For better energy storage devices, Li-ion batteries (LIBs) and supercapacitors are currently being extensively researched. LIBs with fast charging and discharging ability, long cycle life, and high energy density are one among the promising solutions for energy storage and suitable for portable electronics. Several materials are used as anode, cathode, electrolyte, and separator for lithium-ion battery. The well-established anode material for lithium-ion battery is graphite (372 mAh g^{-1} capacity) but its low capacity fails to meet most of the applications [148,149]. Several materials like transition metal oxides and their composites[149-153], sulfides [154-159], polymers [160-162], nitrides [163-167], carbonaceous material [168-172], chalcogenides [173,174], silicon-based materials [175-181], and metal alloys [182-184] are widely used anode materials. Among them, transition metal oxides as anode material of LIBs have several advantages like excellent capacity and cyclic stability, low cost, and easy availability [185]. As a member of metal oxide, $ZnWO_4$ is also suitable for ion intercalation. $ZnWO_4$ is widely used as photocatalyst [186,187], photoanode [188], sensors [189-192], electrocatalyst [193,194], and supercapacitor [142,138,137]. Very few works are reported on $ZnWO_4$ as the

electrode for LIBs. Shi Nianxiang et al. [139] hydrothermally synthesized $ZnWO_4$ hierarchical hexangular microstars and used as anode material for the LIBs. It revealed the first discharge and charge capacity of 777 mAh g^{-1} and 585 mAh g^{-1} respectively. However, the application of $ZnWO_4$ as an anode material for LIB is hindered by large volume change and high initial reversible capacity, which leads to poor cycling performance. To resolve these issues, carbonaceous materials like reduced graphene oxide (r-GO) and carbon nanotubes (CNT) are used as buffers because carbonaceous materials can improve the conductivity, contact and also reduce the mechanical stress produced by the volume change of the $ZnWO_4$. Due to good electrical conductivity, high surface area, and greater mechanical flexibility, graphene has attracted most attention for fabricating high-performance composite. Linsen Zhang et al. [136] prepared $ZnWO_4$/CNTs composite as anode material reported superior electrochemical performance than pure $ZnWO_4$. Wang Xiao et al. [132] reported the synthesis and application of $ZnWO_4$@r-GO hybrids as an anode material for LIBs. The discharge capacity of 566.6 mAh g^{-1} at 100 mA g^{-1} current density is reported $ZnWO_4$@r-GO, which is higher than bare $ZnWO_4$. Also, 477.3 mAh g^{-1} is obtained after 40 cycles at a current density of 100 mA g^{-1}. To improve the capacity and cyclic stability, herein we report the preparation of $ZnWO_4$@r-GO nanocomposite by single-step solvothermal method and its performance as anode material for LIBs. Further, the comparison of electrochemical properties with pristine $ZnWO_4$ demonstrates that r-GO enhances the electron conveyance leading to improved capacity of 1158 mAh g^{-1} at 100 mA g^{-1} and reduces the degradation of the $ZnWO_4$. The synergetic effect of r-GO and $ZnWO_4$ improves the capacity, columbic efficiency, and stability of the material.

3.2 SYNTHESIS, STRUCTURAL, CHEMICAL AND MORPHOLOGICAL CHARACTERIZATION OF ZnWO₄@r-GO NANOCOMPOSITE

3.2.1 Preparation of ZnWO₄:

The chemicals used in this work were of analytical grade and were used as obtained. $ZnWO_4$ nanoparticles were synthesized by mixing 0.35 g of sodium tungstate dihydrate (98%) and 0.523 g of zinc acetate dihydrate with 1:1 ratio of distilled water and ethylene glycol and stirred for about 15 minutes. Obtained white solution mixture was transferred into a teflon jar and

placed in the autoclave at 180 °C for 24 hours and allowed to cool to room temperature. Thus, obtained precipitates were collected and washed with distilled water, ethanol and acetone for several times. Then the samples are dried overnight in a vacuum oven at 65°C.

3.2.2 Preparation of ZnWO$_4$@r-GO nanocomposite:

GO was prepared using modified Hummer's method as reported in our previous reports [195,196]. The ZnWO$_4$@r-GO nanocomposite was synthesized by following the same method as that of zinc tungstate with the addition of 0.5 mg GO.

3.3 RESULTS AND DISCUSSION

3.3.1 X-ray diffraction (XRD) analysis

Figure 3.1 represents the XRD pattern of the as prepared pristine ZnWO$_4$ and ZnWO$_4$@r-GO nanocomposite. The diffraction patterns of the samples were indexed using Xpert high score plus software. The diffraction peaks of the pristine ZnWO$_4$ and ZnWO$_4$@r-GO nanocomposite match with the JCPDS Card No.00-015-0774 with space group of P2/c, lattice constants a= 0.472 nm, b= 0.570 nm and c= 0.495 nm, which indicates monoclinic Wolframite structure. A small hump at 12° and 21° in the ZnWO$_4$@r-GO nanocomposite is ascribed to the incorporation of the r-GO into the composite. From the figure 3.1, it is evident that monoclinic Wolframite structure of ZnWO$_4$ has not been affected by the addition of r-GO.
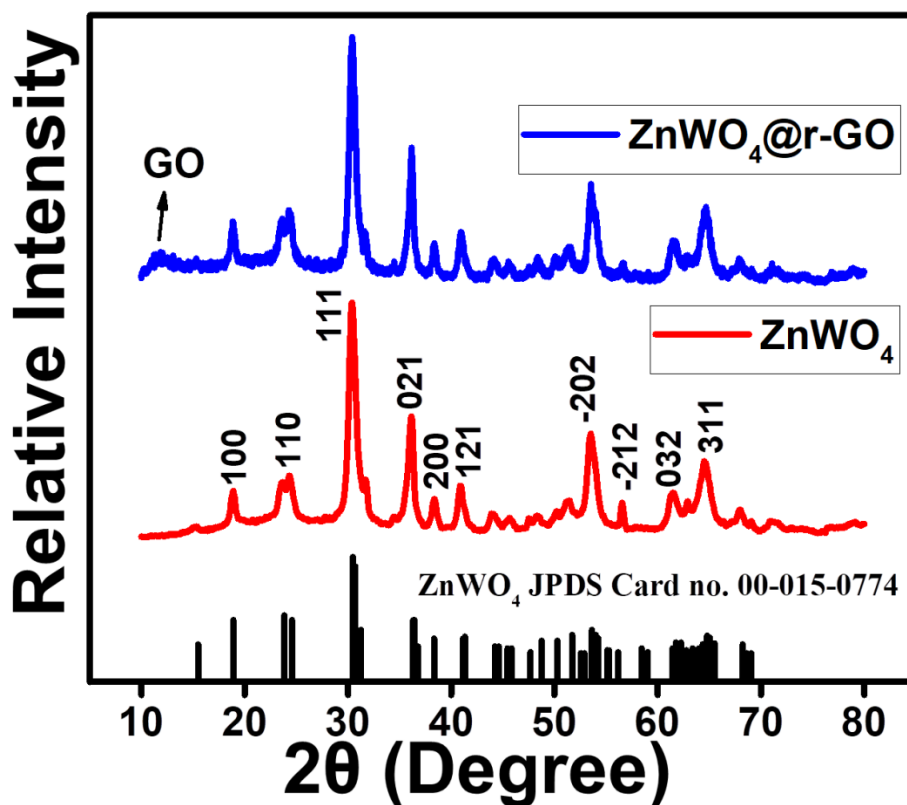
**Figure 3.1 XRD pattern of the pristine ZnWO₄ and ZnWO₄@r-GO nanocomposite at 2°
min⁻¹ scan rate and 10–80° 2θ range of pristine ZnWO₄ and ZnWO₄@r-GO
nanocomposite.**

3.3.2 Thermogravimetric analysis (TGA)

TGA was performed to determine the exact amount of carbon content in the $ZnWO_4$@r-GO
nanocomposite, in air ambient from room temperature to 700 °C, as represented in the Figure
3.2 The plot shows the first trivial weight loss of $ZnWO_4$@r-GO nanocomposite in the
temperature range up to 100 °C. This loss is due to moisture and surface bound water
molecules. The result indicates approximately 1 wt% loss in the $ZnWO_4$@r-GO
nanocomposite. Significantly, $ZnWO_4$@r-GO nanocomposite shows a highest weight loss (~5
wt%) in the temperature range from 100 to 550 °C, which is attributed to the combustion of
graphene and amorphous carbon[197]. From 550 to 700 °C, only $ZnWO_4$ was left. Based on
the weight loss in the TGA plot, the $ZnWO_4$ content in the $ZnWO_4$@r-GO nanocomposite is
about ~94 wt%.
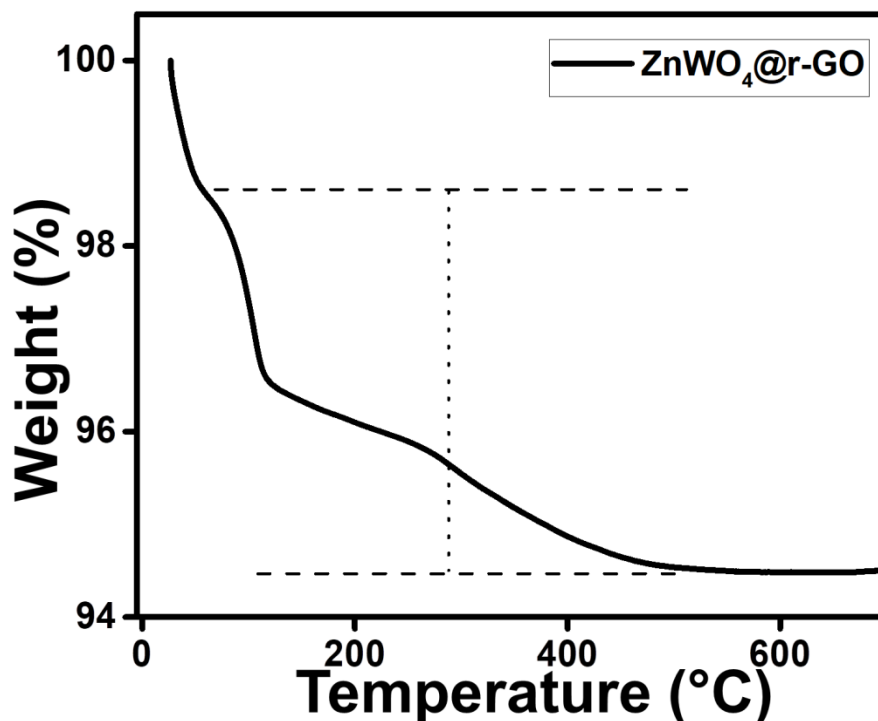
Figure 3.2 TGA curve of the ZnWO4@r-GO nanocomposite from room temperature to 700 °C in the air atmosphere.

3.3.3 X-ray photoelectron spectroscopy (XPS) analysis

The chemical state and elemental composition of the pristine $ZnWO_4$ and $ZnWO_4$@r-GO nanocomposite was confirmed from X-ray photoelectron spectroscopy (XPS). XPS spectra were calibrated by C 1s peak (284.6 eV). Figure 3.3 (a) represents the survey spectra of pristine $ZnWO_4$ and $ZnWO_4$@r-GO nanocomposite, which displays four peaks at 35.7, 246.7, 530.7 and 1020.7 eV, shows the existence of W, Zn, O and C elements[198,199]. Pristine $ZnWO_4$ shows surface absorbed carbon species only. Figure 3.3 (b) exhibits the binding energy peaks of $ZnWO_4$ at 1021.4 and 1044.5 eV, which are ascribed to Zn $2p_{3/2}$ and Zn $2p_{1/2}$ respectively indicating the existence of Zn^{2+} ions of the $ZnWO_4$[200].
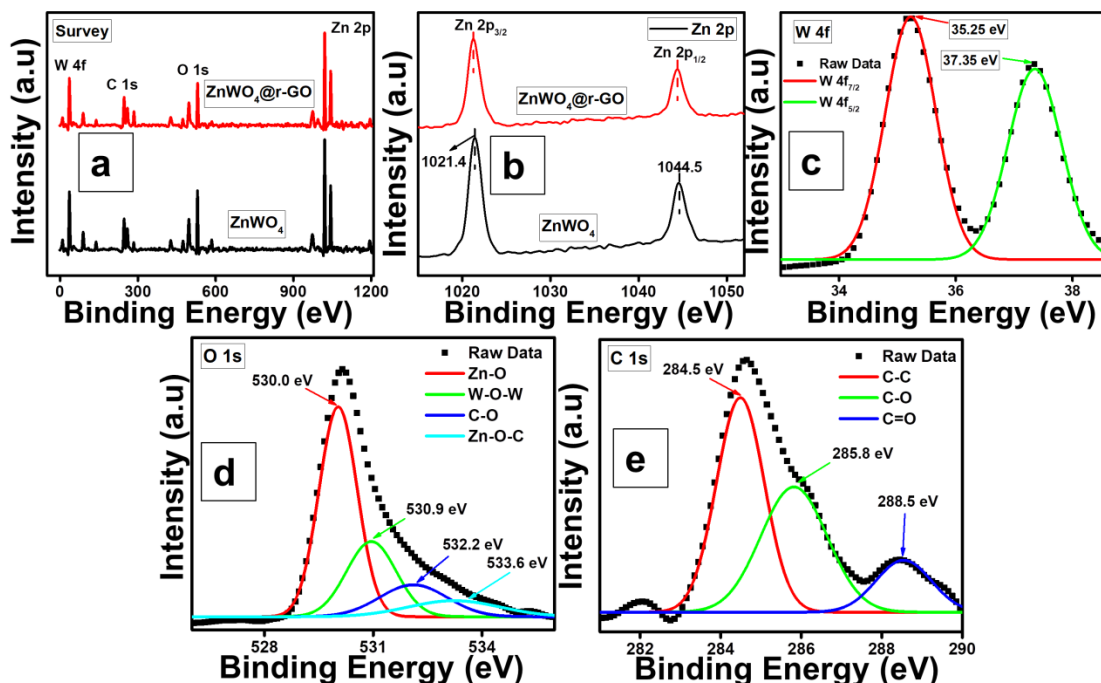
Figure 3.3 (a) XPS survey spectra and high-resolution spectra of (b) Zn 2p of pristine ZnWO₄ and ZnWO₄@r-GO nanocomposite, (c, d, f) deconvoluted high resolution spectra of W 4f, O 1s and C 1s of the ZnWO₄@r-GO nanocomposite.

Similarly, the binding energy of Zn $2p_{3/2}$ and Zn $2p_{1/2}$ of ZnWO₄@r-GO nanocomposite were 1021.3 and 1044.4 eV respectively, with a shift of 0.1 eV to low energy region. The deconvoluted peaks analogous to W 4f of ZnWO₄@r-GO nanocomposite are represented in the Figure 3.3 (c) having binding energy peak at 35.25 eV for W $4f_{7/2}$ and 37.35 eV for W $4f_{5/2}$. However, in comparison to ZnWO₄, the W 4f peaks of ZnWO₄@r-GO nanocomposite have shifted by 0.2 eV towards higher binding energy. Similarly, O 1s high resolution spectra of ZnWO₄@r-GO was represented in Figure 3.3 (d), which consist of deconvoluted four peaks at 530.0, 530.9, 532.2 and 533.6 eV corresponding to oxygen coordination in Zn-O, W-O-W of ZnWO₄, hydroxyl/epoxy groups of r-GO and Zn–O–C bonds between ZnWO₄ and r-GO surfaces respectively[201,198]. The deconvoluted high resolution C 1s spectra of ZnWO₄@r-GO nanocomposite were represented in the Figure 3.3 (e). The Figure 3.3 (e) depicts three peaks at 284.5, 285.8 and 288.5 eV, which can be ascribed to the C-C, C-O and C=O groups respectively. The intensity of the oxygenated peaks are reduced due to GO being adequately reduced to r-GO[202]. For the comparison, high resolution spectra of W 4f, O 1s and C 1s of

the pristine $ZnWO_4$ and $ZnWO_4$@r-GO nanocomposite was represented in the Figure 3.4 (a, b, c). The deconvoluted high resolution spectra of the W 4f and O 1s of the pristine $ZnWO_4$ represented in the Figure 3.4 (d, e, f).
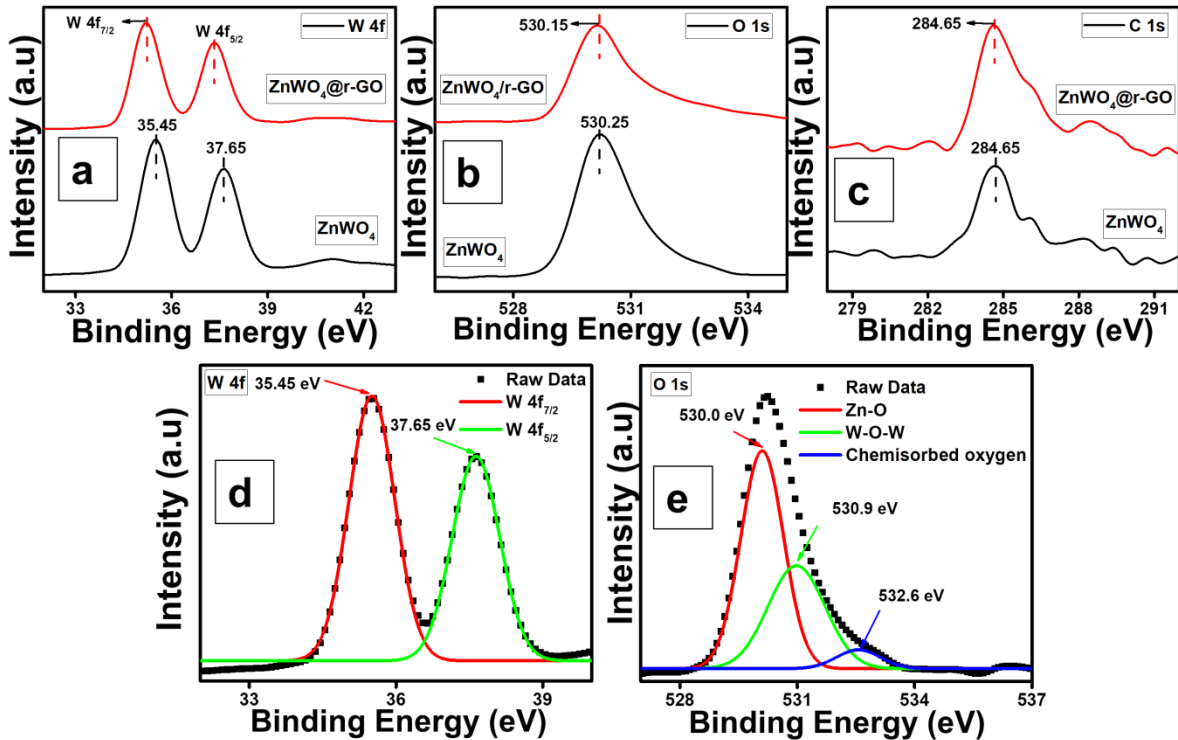
Figure 3.4 High resolution spectra of (a) W 4f, (b) O 1s and (c) C 1s of pristine $ZnWO_4$ and $ZnWO_4$@r-GO nanocomposite. Deconvoluted high resolution spectra of (d) W 4f and (e) O 1s of pristine $ZnWO_4$

3.3.4 Scanning Electron Microscopy (SEM)

The morphology of the pristine $ZnWO_4$ and $ZnWO_4$@r-GO nanocomposite was analyzed through SEM images. The pristine $ZnWO_4$ and $ZnWO_4$@r-GO nanocomposite have irregular nanorods of a few microns in length as shown in the Figure 3.5 (a, c). The EDS spectra of the $ZnWO_4$ and $ZnWO_4$@r-GO nanocomposite in Figure 3.5 (b, d) confirm the elemental composition of O, Zn and W in addition to carbon atomic percentage of 19, which is in agreement with XPS results.
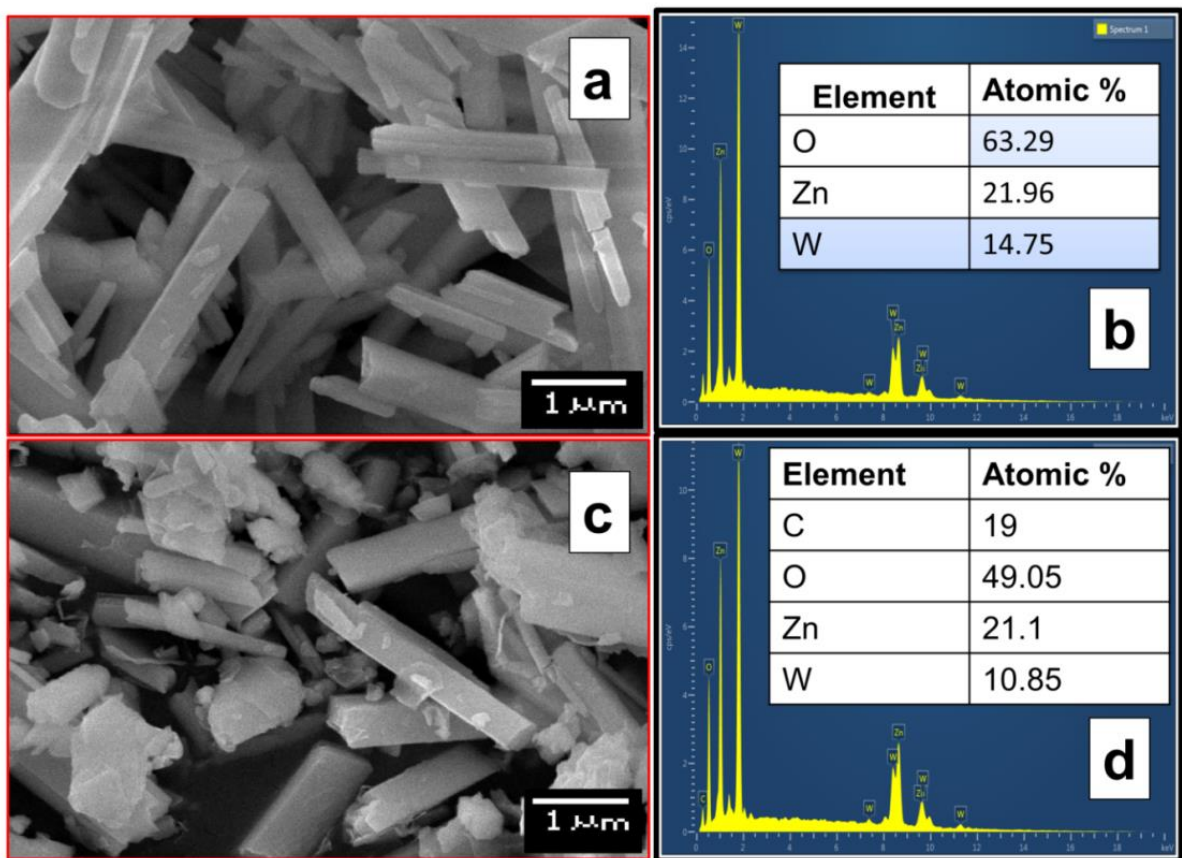
Figure 3.5 SEM images of the pristine (a) ZnWO₄ and (c) ZnWO₄@r-GO nanocomposite. The energy dispersive X-ray (EDS) spectrum of (b) ZnWO₄ and (d) ZnWO₄@r-GO nanocomposite

3.3.5 High-resolution transmission electron microscopy (HR-TEM)

Figure 3.6 (a) depicts the TEM image (b) HRTEM image and (c) SAED pattern of pristine $ZnWO_4$ nanorods. The average length and diameter of nanorods is approximately 20-50 nm and 6- 9 nm respectively as measured from TEM image of pristine $ZnWO_4$ and $ZnWO_4$@r-GO nanocomposite. Figure 3.6 (b) and (e) show the interplanar spacing of 0.47 and 0.52 nm for pristine $ZnWO_4$ having (100) and (010) plane respectively and 0.52 nm for $ZnWO_4$@r-GO nanocomposite having (010) plane. The monoclinic phase of the samples is confirmed by the HR-TEM. Figure 3.6 (d) denotes TEM image (e) HRTEM image and (f) SAED pattern of $ZnWO_4$@r-GO nanocomposite. TEM image (Figure 3.6 (d)) of $ZnWO_4$@r-GO nanocomposite reveals the growth of $ZnWO_4$ nanorod over the reduced graphene sheet. The ring SAED pattern

of pristine $ZnWO_4$ nanorods and $ZnWO_4$@r-GO nanocomposite confirms the polycrystalline structure. SEAD pattern of pristine $ZnWO_4$ nanorods and $ZnWO_4$@r-GO nanocomposite are indexed to (100) and (110) planes respectively, which matches with the XRD results.
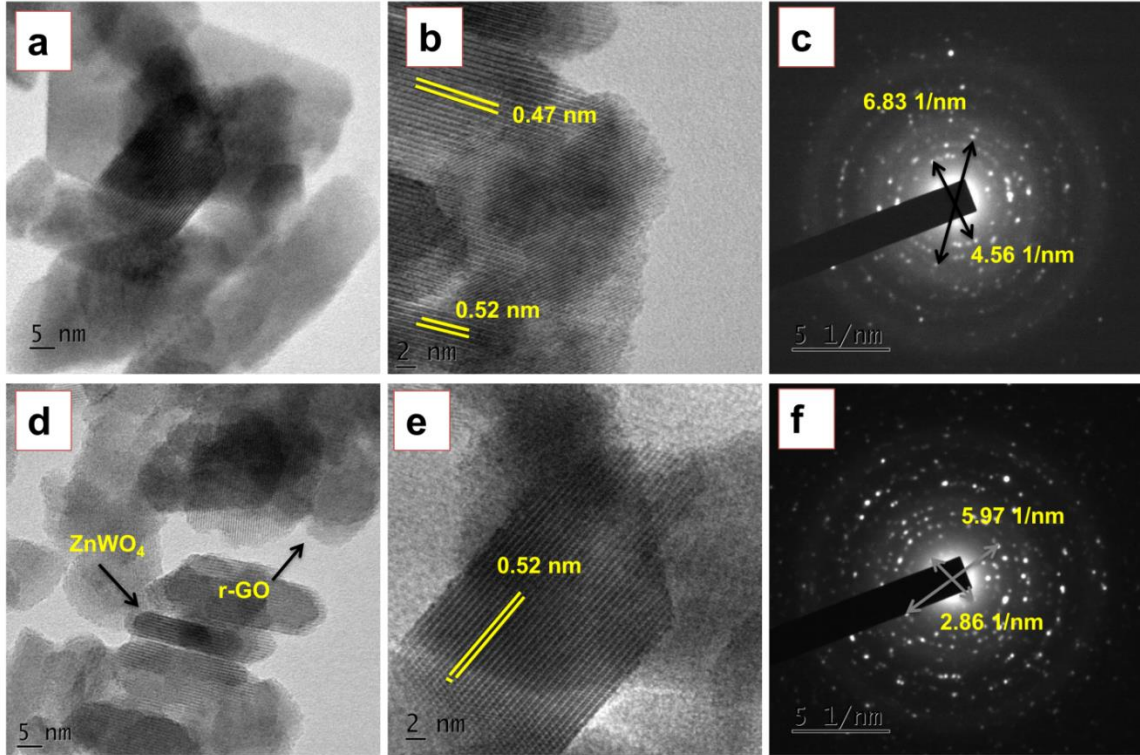
Figure 3.6 (a) TEM image, (b) HRTEM image and (c) SAED pattern of pristine $ZnWO_4$. (d) TEM image, (e) HRTEM image and (f) SAED pattern of $ZnWO_4$@r-GO nanocomposite.

3.3.6 BET surface area analysis

The N_2 absorption and desorption isotherms of the prepared pristine $ZnWO_4$ and $ZnWO_4$@r-GO nanocomposite were represented in the Figure 3.7. The sample shows IV isotherm type, which represents the mesoporous powder. The surface areas of pristine $ZnWO_4$ and $ZnWO_4$@r-GO nanocomposite as obtained from BET analysis were 38.771 m² g^{-1} and 50.802 m² g^{-1} respectively. $ZnWO_4$@r-GO nanocomposite shows higher surface area than pristine $ZnWO_4$. Figure 3.7 (c, d) shows the size distribution curves of the pristine $ZnWO_4$ and $ZnWO_4$@r-GO nanocomposite. The values of the surface area, pore volume and pore diameter

are tabulated in Table 3.1. The ZnWO$_4$@r-GO nanocomposite displays greater surface area, however, nearly the same pore diameter and volume[203].
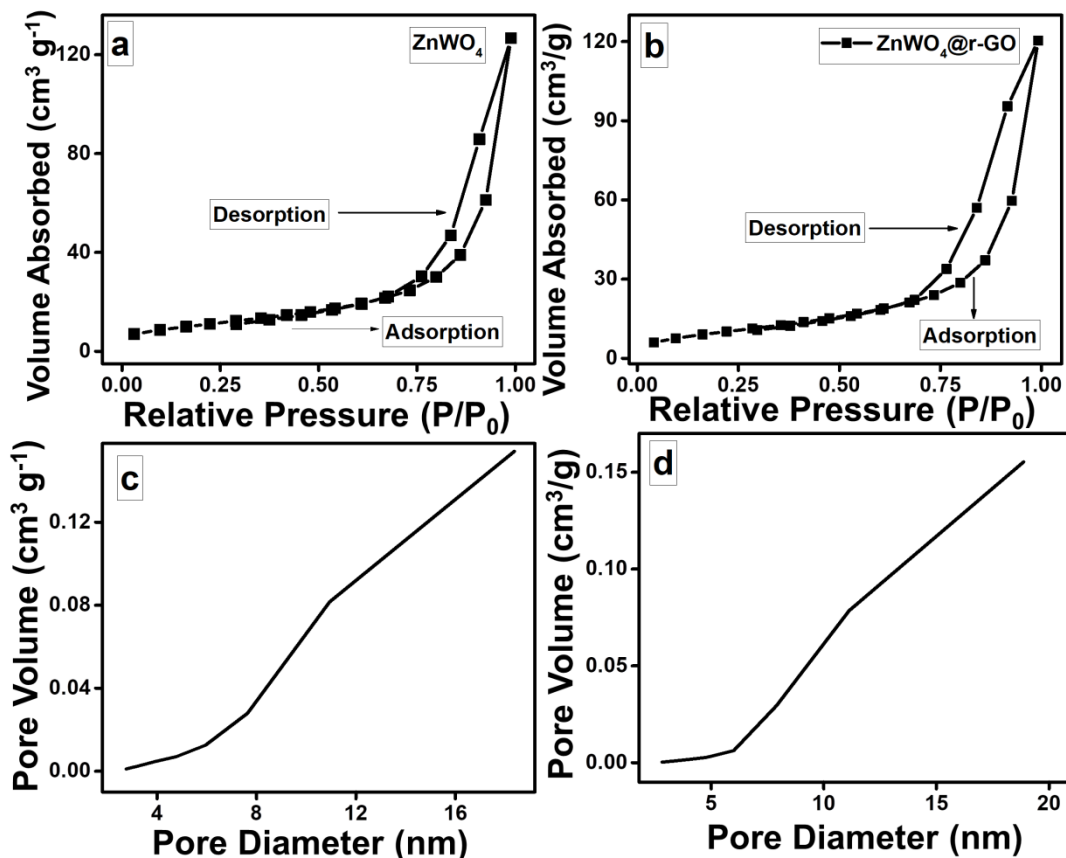
Figure 3.7 N$_2$ adsorption and desorption isotherms of pristine (a) ZnWO$_4$ and (b) ZnWO$_4$@r-GO nanocomposite. (c, d) corresponding pore size distribution curves

Table 3.1 Surface area from BET analysis

Sample	Surface Area (m^2 g^{-1})	Pore Volume (cc g^{-1})	Pore diameter (nm)
ZnWO$_4$	38.771	0.138	10.919
ZnWO$_4$@r-GO nanocomposite	50.802	0.155	11.125

52

3.3.7 Electrochemical measurements

The electrochemical reactions of the prepared pristine $ZnWO_4$ and $ZnWO_4$@r-GO nanocomposite were studied using CV technique. The CV was performed at a scan rate of 0.1 mV s^{-1} in the voltage range 0.02 to 3 V versus Li/Li$^+$ as shown in the Figure 3.8. The CV plot for both $ZnWO_4$ and $ZnWO_4$@r-GO nanocomposite, shows similar shape signifying that pristine $ZnWO_4$ and $ZnWO_4$@r-GO nanocomposite have similar electrochemical reaction. The cathodic peaks noticed at 0.58 and 0.76 V are considered to be due to $ZnWO_4$ reduction to Zn and W as mentioned in equation (1). SEI film formation on electrode surface and Li-Zn alloy formation as shown in equation 2 are the two possible factors that give rise to additional minor cathodic peaks. The peak from 0.65 to 2 V corresponds to the oxidation of Zn^0 to Zn^{2+} and oxidation of WO_3 to W^{6+} along with decomposition of the Li_2O matrix[136]. Zn and W oxidation as shown in equation 3 results in the first anodic peaks at 0.68 V and 1.12 V. The integrated area in CV of the $ZnWO_4$@r-GO nanocomposite is greater than that of pristine $ZnWO_4$; this is due to the incorporation of r-GO into $ZnWO_4$, which significantly enhances the electronic conductivity.
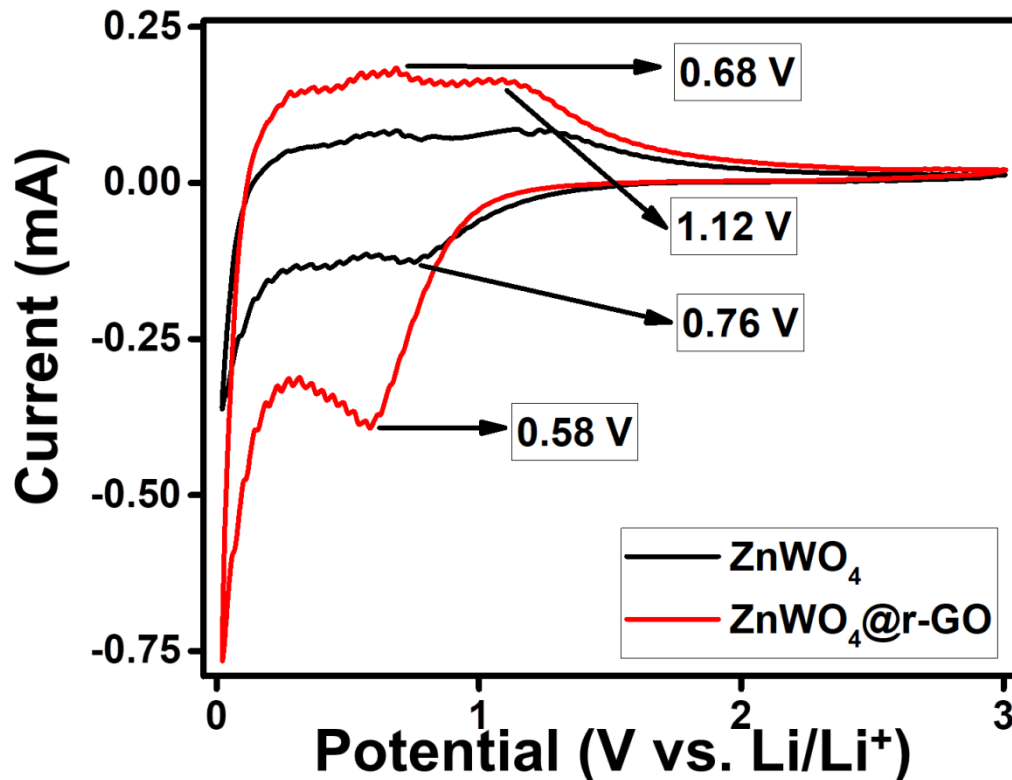
Figure 3.8 The cyclic voltammetric profiles of the pristine $ZnWO_4$ and $ZnWO_4$@r-GO nanocomposite in 0.1 mV s^{-1} scan rate and 0.02 to 3 V versus Li/Li$^+$ potential range.

The above discussion is based on the reactions of the pristine $ZnWO_4$ that can be summarized as follows [131,139,133]:

$$ZnWO_4 + 8Li^+ + 8e^- \rightarrow Zn + W + 4Li_2O \tag{3.1}$$

$$Zn + Li^+ + e^- \leftrightarrow LiZn \tag{3.2}$$

$$LiZn + W + 4Li_2O \leftrightarrow Zn + WO_3 + 7Li^+ + 7e^- + Li_2O \tag{3.3}$$
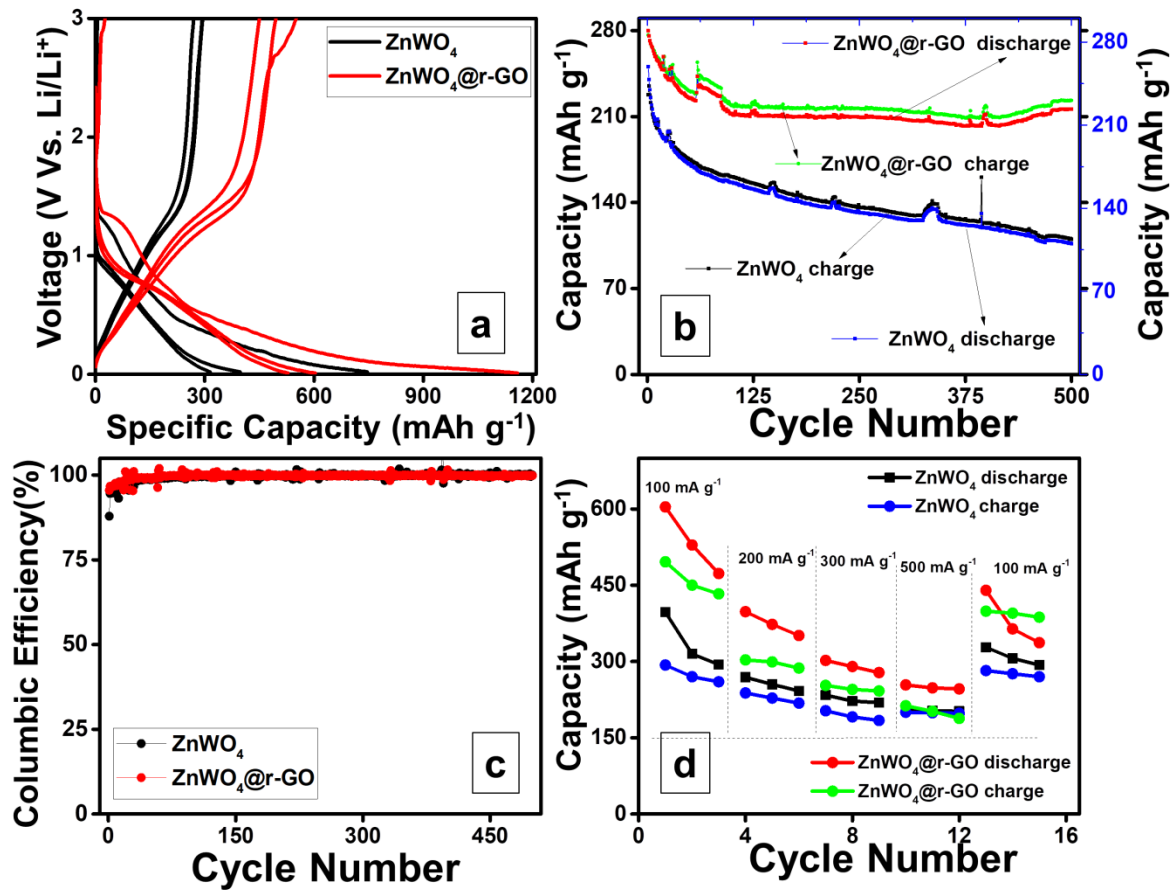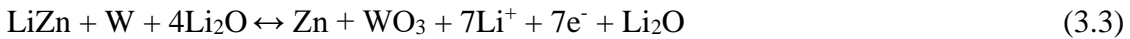
Figure 3.9 (a) Charge/discharge curves of the $ZnWO_4$ and $ZnWO_4$@r-GO nanocomposite at 100 mA g^{-1} current density. (b) Cycle number versus charge/discharge capacity plot of $ZnWO_4$ and $ZnWO_4$@r-GO nanocomposite for 500 cycles at 300 mA g^{-1}. (c) Cycle number versus columbic efficiency plot and (d) comparison of the rate capability of $ZnWO_4$ and $ZnWO_4$@r-GO nanocomposite.

54

The electrochemical enactment of the pristine $ZnWO_4$ and $ZnWO_4$@r-GO nanocomposite was studied by galvanostatic charge/discharge techniques at current density of 100 mA g^{-1} and potential window 0.02 - 3 V versus Li/Li$^+$ at a room temperature as shown in the Figure 3.9 (a). The similar charge discharge graph with different current density is shown in the Figure 3.10. The initial discharge capacity of the $ZnWO_4$@r-GO nanocomposite is found to be 1158 mAh g^{-1} and initial charge capacity is 552 mAh g^{-1}, which is higher than that of pristine material (746 and 295 mAh g^{-1}). The capacity is greater than calculated theoretical capacity (600-750 mAh g^{-1}), which may be due to the formation of the SEI layer and synergetic effect of $ZnWO_4$ and r-GO. The $ZnWO_4$@r-GO nanocomposite also exhibits good cyclic stability over 500 cycles at 300 mA g^{-1} as shown in the Figure 3.9 (b). From Figure 3.9 (b), the $ZnWO_4$@r-GO nanocomposite shows 277 mAh g^{-1} and 290 mAh g^{-1} charge/discharge capacity at 300 mA g^{-1} current density. After 500 cycles the charge /discharge capacity of $ZnWO_4$@r-GO nanocomposite is 224 and 225 mAh g^{-1} respectively. The columbic efficiency of the $ZnWO_4$@r-GO nanocomposite is 95% for the 1st cycle and it is 99.9% for 500th cycle as represented in Figure 3.9 (c). Further, $ZnWO_4$@r-GO nanocomposite shows 80.74% capacity retention even after 500 cycles, which is higher than that of pristine $ZnWO_4$ (48.35% charge retention). The capacity retention plot is represented in the Figure 3.11, which reveals better structural stability of the $ZnWO_4$@r-GO nanocomposite compared to pristine $ZnWO_4$.
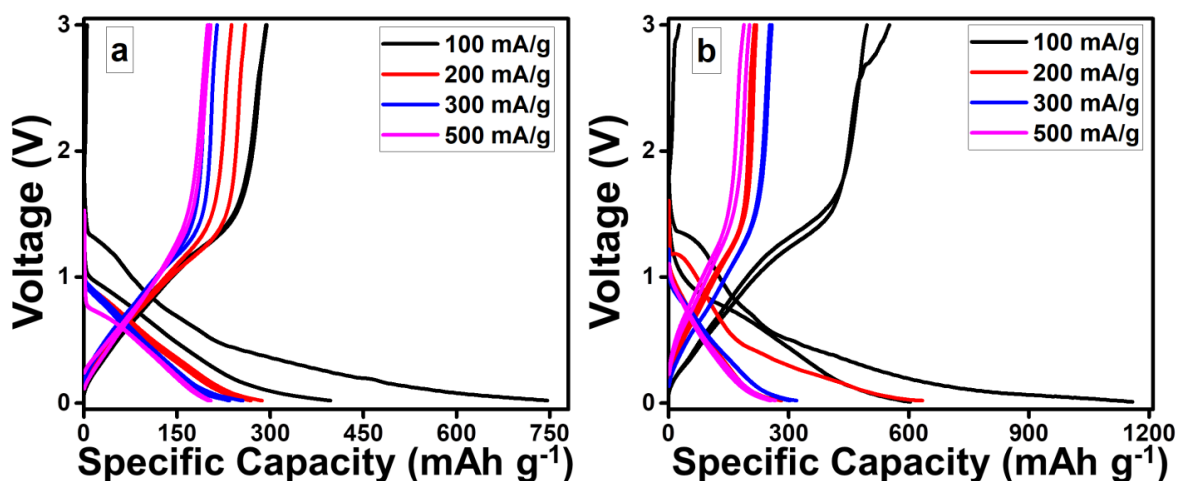
Figure 3.10 the first two cycle charge/discharge curves of (a) ZnWO₄ and (b) ZnWO₄@r-GO nanocomposite at 100, 200, 300 and 500 mA g⁻¹ current densities.

The Figure 3.9 (d) shows the rate capability of the pristine $ZnWO_4$ and $ZnWO_4$@r-GO nanocomposite. The charge/discharge capacity of the pristine $ZnWO_4$ and $ZnWO_4$@r-GO nanocomposite decreases with rise in current density. It is to be noted that higher capacity is obtained at lower current densities compared to higher current densities. This is explained through kinetics of the charges in the cell. Higher the current density, faster is the kinetics of the charges within the cell. Thus, the ions lack the time to accommodate within the lattice and reduce the capacity.
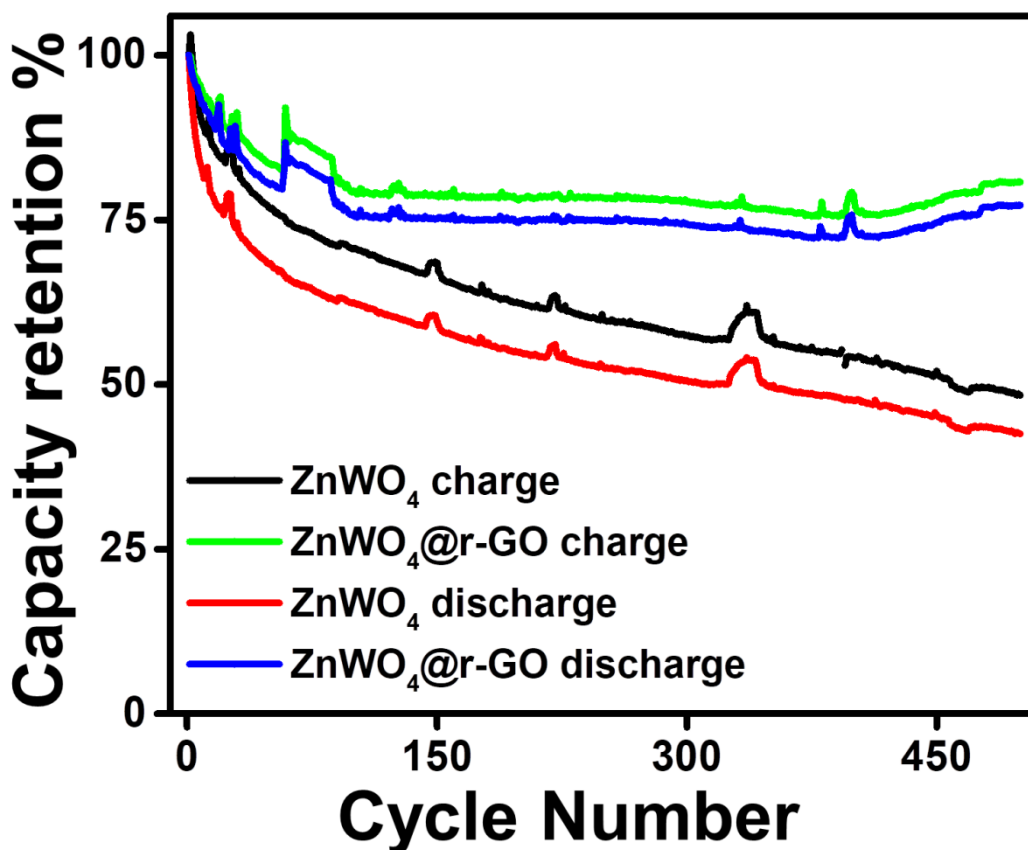
Figure 3.11 Capacity retention versus cycle number plot of $ZnWO_4$ and $ZnWO_4$@r-GO nanocomposite

To study the rate capability of the materials, charge/discharge test was performed from 100 to 500 mA g^{-1} current density. While increasing the current density from 100, 200, 300 and 500 mA g^{-1}, $ZnWO_4$@r-GO nanocomposite shows average discharge capacities of 604, 398, 302 and 254 mAh g^{-1} respectively. Likewise, the charge capacity of 496, 303, 253 and 213 mAh g^{-}

[1] respectively have been obtained, which is higher than that of pristine $ZnWO_4$ discharge/charge capacity. At higher current density, capacity reduces due to insufficient conducting path of graphene in $ZnWO_4$@r-GO nanocomposite. Notably, the $ZnWO_4$@r-GO nanocomposite reverted to 440 mAh g^{-1}, compared to 604 mAh g^{-1}. In $ZnWO_4$@r-GO nanocomposite, the reduced graphene oxide offers a large aspect ratio, which leads to the long transport path for Li^+ and limits the rate capacity. So, the $ZnWO_4$@r-GO nanocomposite has lower rate capacity than that of $ZnWO_4$ [204,205]. However, $ZnWO_4$@r-GO nanocomposite has a higher specific capacity and cyclic stability compared to pristine $ZnWO_4$.

From the TGA curve, the $ZnWO_4$@r-GO nanocomposite contains approximately 94 wt% of $ZnWO_4$ and 6 wt% of r-GO. Based on the theoretical capacity of $ZnWO_4$ (684 mAh g^{-1}) and the theoretical capacity of graphene (744 mAh g^{-1}), the theoretical capacity of the $ZnWO_4$@r-GO nanocomposite was calculated to be 686 mAh g^{-1}[206]. Compared to the present discharge capacity of $ZnWO_4$ (397 mAh g^{-1}), the extra incremental discharge capacity of $ZnWO_4$@r-GO nanocomposite was 207 mAh g^{-1}. Using theoretical capacity of grapheme (744 mAh g^{-1}), the enhanced capacity from Li^+ storage in graphene is presumably 45 mAh g^{-1}. From the above calculation, the contribution from the electronic conductivity of graphene in the composite may be 162 mAh g^{-1} [207]. The Lithium storage capacity of prepared and reported tungstate based anode material for LIBs are compared and listed in the Table 3.2. Based on data from Table 2, prepared $ZnWO_4$@r-GO nanocomposite exhibit superior lithium storage capacity than other previous reports. From BET data, $ZnWO_4$@r-GO nanocomposite exhibits larger surface area than $ZnWO_4$. The incorporation of r-GO into $ZnWO_4$ increases the surface area, which enhances the charge/discharge capacity of the $ZnWO_4$@r-GO nanocomposite. This indicates the capacity enhancement is arriving due to the lithium ion intercalation and extraction during cycling.

Table 3.2 Comparison of prepared ZnWO₄@r-GO nanocomposite with reported tungstate anode material for LIBs

Sl No	Electrode	Preparation Method	Discharge Capacity (mAh g^{-1})	Current Density / C-rate	Ref
1	$ZnWO_4$	Sol–Gel method	705.9	50 mA g^{-1}	[136]

2	ZnWO$_4$/RGO hybrid	Hydrothermal Method	566.6	100 mA g^{-1}	[132]
3	FeWO$_4$/C	Hydrothermal method	771.6	100 mA g^{-1}	[208]
4	ZnWO$_4$ Hierarchical Hexangular Microstars	Two Step Hydrothermal Method	777	200 mAg^{-1}	[139]
5	ZnWO$_4$ Nanorods	Facile hydrothermal process	1140	0.2 C	[131]
6	Nanocrystalline ZnWO$_4$	Wet chemical method	783.8	100 mA g^{-1}	[209]
7	ZnWO$_4$/graphene composite	Sol–Gel method	1016	50 mA g^{-1}	[207]
8	Core/shell ZnWO$_4$/carbon nanorods	Hydrothermal Method	512	0.1 C	[210]
9	NiWO$_4$	Electro spinning method	888	100 mA g^{-1}	[211]
10	ZnWO$_4$ Nanorods	Hydrothermal Method	746	100 mA g^{-1}	Present work
11	ZnWO$_4$@r-GO nanocomposite	Hydrothermal Method	1158	100 mA g^{-1}	Present work

The kinetics of the pristine ZnWO$_4$ and ZnWO$_4$@r-GO nanocomposite was studied using EIS, in the frequency range 1 mHz - 50 kHz as represented in the Figure 3.12. Equivalent circuit of the Nyquist plot is represented in the inset of Figure 3.12. Nyquist plot of ZnWO$_4$ and ZnWO$_4$@r-GO nanocomposite contains two semicircles that extend from region of high frequency to medium frequency. At low frequency region, an inclined line is observed which corresponds to two processes, charge transfer of lithium ion from electrolyte into electrode and lithium ion diffusion to the electrode, the latter being referred to as Warburg impedance[212]. The radius of the semicircle in the plot of ZnWO$_4$@r-GO nanocomposite is smaller than that of pristine ZnWO$_4$, which is due to the incorporation of r-GO. It indicates the faster kinetic process of ZnWO$_4$@r-GO nanocomposite compared to that of pristine ZnWO$_4$. The conductivity of ZnWO$_4$ is significantly improved by r-GO network. The fitted values for the Nyquist plots of pristine ZnWO$_4$ and ZnWO$_4$@r-GO nanocomposite are represented in the Table 3.3.
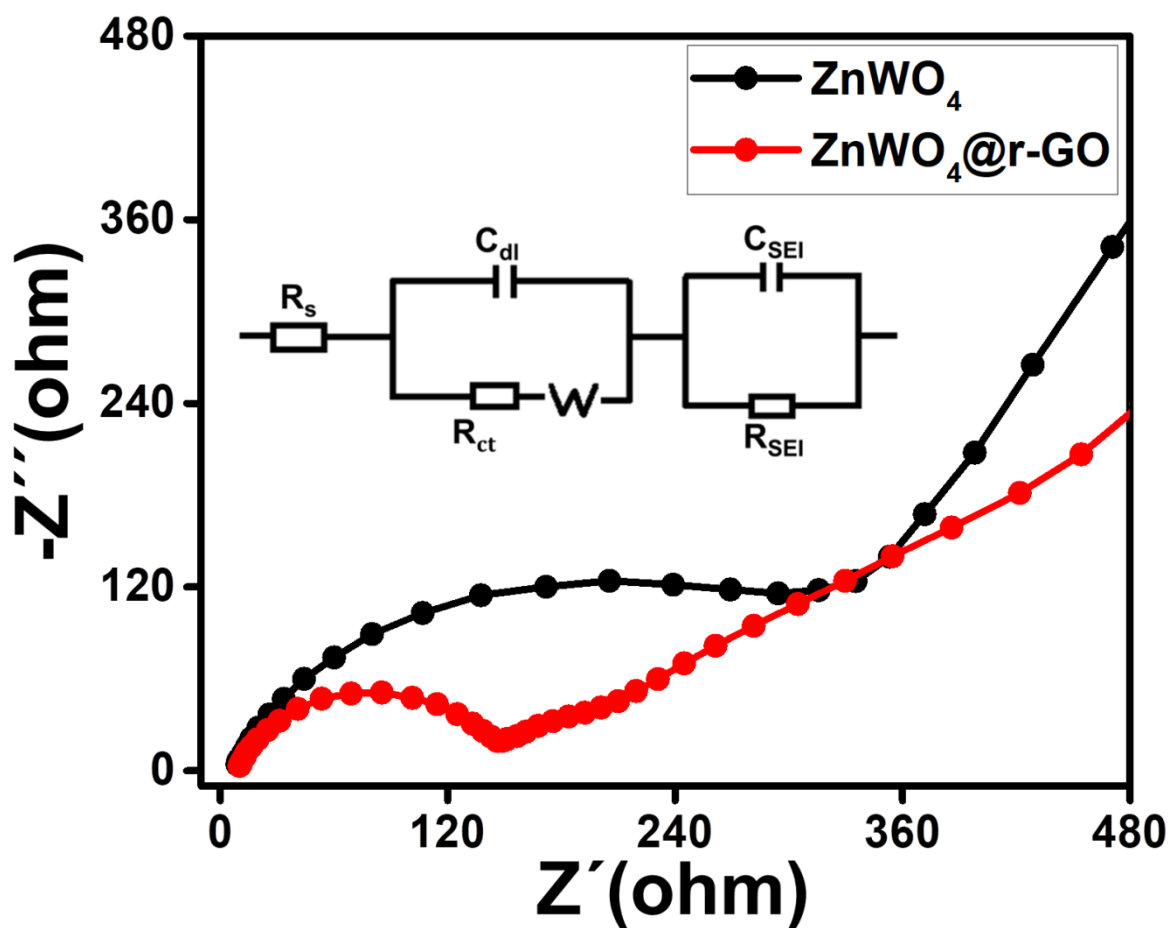
Figure 3.12 Nyquist plots of ZnWO₄ and ZnWO₄@r-GO nanocomposite. Equivalent fitted circuit given as inset.

Table 3.3 Nyquist plot fitted values of ZnWO₄ and ZnWO₄@r-GO nanocomposite

Sample	R_s (Ω)	C_{dl} (µF)	R_{ct} (Ω)	W(Ω s$^{-1/2}$)	C_{SEI} (µF)	R_{SEI} (Ω)
ZnWO₄	10.58	1.303	112.6	56.67	3.341	158.3
ZnWO₄@r-GO nanocomposite	8.559	7.431	16.14	1344	3.7	27.14

To further investigate the crystal structure of the prepared ZnWO₄ and ZnWO₄@r-GO nanocomposite, ex-situ XRD was performed after 500 cycles as represented in the Figure 3.13

(a). The difference in XRD pattern of $ZnWO_4$ and $ZnWO_4$@r-GO nanocomposite before and after charge/discharge cycle are observed, indicating electrochemical reactions of Li and $ZnWO_4$ as per equations 1, 2 and 3. From the Figure 3.13 (a), we can observe the absence of few XRD peaks, which illustrates the destruction of $ZnWO_4$. The peaks around 43.26°, 50.42° and 74.26° are due to Cu foil on which the material was coated, and the peak at around 32.68° is indexed to Li_2O[213] and also the peak at 35.96° and 39.32° are indexed to tungsten (JCPDS Card No. 03-065-6453). After 500 discharge cycles, emergence Li_2O peak indicates the reaction of Li with oxygen present in $ZnWO_4$.
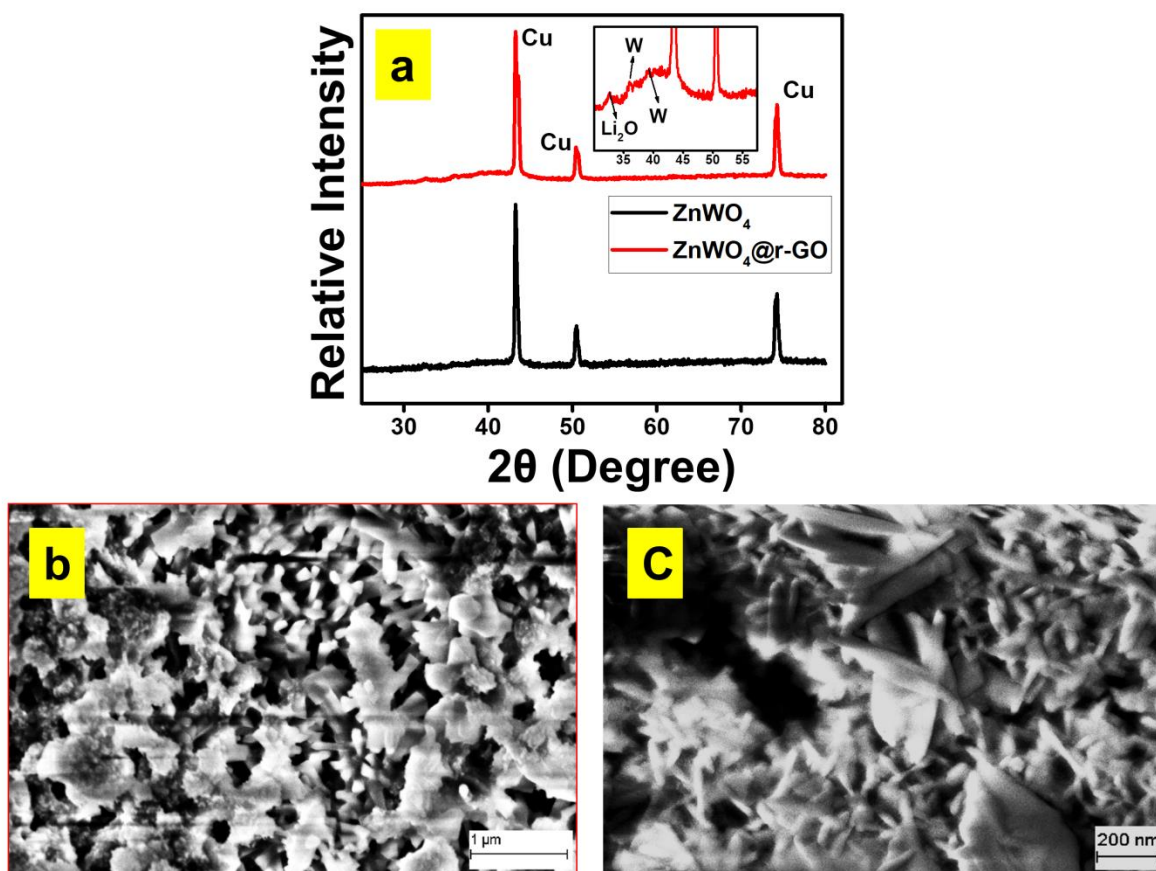
Figure 3.13 (a) Ex-situ XRD plot after 500 cycles (b, c) SEM images of the pristine $ZnWO_4$ and $ZnWO_4$@r-GO nanocomposite after 500 cycles.

The morphology of the pristine $ZnWO_4$ and $ZnWO_4$@r-GO nanocomposite after 500 cycles at 300 mA g^{-1}, FE-SEM is represented in the Figure 3.13 (b) and 3.13 (c) respectively. We can observe from the figure 3.13 (b) that, nanorods morphology of $ZnWO_4$ has been changed after

500 cycles. While drastic changes are not observable in the case of the ZnWO₄@r-GO nanocomposite, which confirms that they do not get destroyed easily and thus have higher cycle stability.

3.4 SUMMARY

- ➤ The pristine $ZnWO_4$ and $ZnWO_4$@r-GO nanocomposite has been synthesized by single step solvothermal method

- ➤ The pristine $ZnWO_4$ and $ZnWO_4$@r-GO nanocomposite exhibits monoclinic Wolframite structure which is match with the JCPDS Card No.00-015-0774

- ➤ TGA plot revels, $ZnWO_4$ content in the $ZnWO_4$@r-GO nanocomposite is about ~94 wt%

- ➤ XPS study confirms the existence of graphene oxide content and Zinc tungstate presence in the $ZnWO_4$@r-GO nanocomposite

- ➤ SEM reveals the irregular nanorods of a few microns in length for pristine $ZnWO_4$ and $ZnWO_4$@r-GO nanocomposite.

- ➤ TEM image confirms the growth of $ZnWO_4$ nanorod over the reduced graphene sheet. The ring SAED pattern of pristine $ZnWO_4$ nanorods and $ZnWO_4$@r-GO nanocomposite confirms the polycrystalline structure.

- ➤ BET results suggest that, sample shows IV isotherm type, which represents the mesoporous powder. The surface areas of pristine $ZnWO_4$ and $ZnWO_4$@r-GO nanocomposite as obtained from BET analysis were 38.771 m² g⁻¹ and 50.802 m² g⁻¹ respectively.

- ➤ The CV plot for both $ZnWO_4$ and $ZnWO_4$@r-GO nanocomposite, shows similar shape signifying that pristine $ZnWO_4$ and $ZnWO_4$@r-GO nanocomposite have similar electrochemical reaction.

- ➤ The $ZnWO_4$@r-GO nanocomposite has discharge capacity of 1158 mAh g⁻¹, a value that is 1.6 times higher than discharge capacity of pristine $ZnWO_4$ (776 mAh g⁻¹).

- ➤ The synergetic effects between r-GO into $ZnWO_4$ enhances the capacity, better capacity retentions, decent rate capability and good cyclic stability of the composite.

- ➤ r-GO contributes to the higher surface area and improved conductivity of the composite.

CHAPTER 4

ZnWO$_4$/SnO$_2$@r-GO NANOCOMPOSITE

AS AN ANODE MATERIAL FOR

HIGHCAPACITY LITHIUM-ION BATTERY

CHAPTER 4

ZnWO$_4$/SnO$_2$@r-GO NANOCOMPOSITE AS AN ANODE MATERIAL FOR HIGH CAPACITY LITHIUM ION BATTERY

This chapter includes the preparation of ZnWO$_4$/SnO$_2$ nanocomposite and ZnWO$_4$/SnO$_2$@r-GO nanocomposite via solvothermal method. This chapter includes the structural, elemental and morphological properties of the prepared samples are characterized using x-ray diffraction (XRD), scanning electron microscopy (SEM), energy-dispersive X-ray spectroscopy (EDAX), high-resolution transmission electron microscopy (HR-TEM), Brunauer-Emmett-Teller (BET) measurements, Raman spectroscopy and X-ray photoelectron spectroscopy (XPS) techniques. Further, prepared samples are tested as an anode for LIB. The ZnWO$_4$/SnO$_2$ (5%) nanocomposite delivers initial discharge capacity of 882 mAh g^{-1} at a current density of 100 mA g^{-1}, while, the specific capacity increases with the increase of SnO$_2$ upto 10% tested in present case. Further, ZnWO$_4$/SnO$_2$@r-GO nanocomposite exhibits a discharge capacity of 1486 mAh g^{-1} which is higher than that of ZnWO$_4$/SnO$_2$ nanocomposite. In addition, after 500 cycles ZnWO$_4$/SnO$_2$@r-GO nanocomposite exhibits 89.8% cycle life and 98% of discharge capacity retention. These results indicate that, ZnWO$_4$/SnO$_2$@r-GO nanocomposite is a promising anode material for LIB.

4.1 INTRODUCTION

Lithium ion battery (LIB) is one of the promising energy storage devices in the modern technology of electronics. Presently, graphite is used as leading commercialized anode material for lithium ion battery with theoretical capacity of 372 mAh g^{-1}[214,215]. The increasing demand of commercialization of LIBs required high energy density, high specific capacity, decent rate capability, low-cost and environmental-friendliness[154] anode material. Therefore, searching for new anode material with notable electrochemical performance and high theoretical capacity is in demand. To improvise the performance of LIBs, several research studies have been done with different anode materials like chalcogenides and their composites[173,216-221], transition metal oxides (TMOs) and their composites[222,223,153,224,225], carbon materials[226-232,151,233], ferrites[234-238], silicon and silicon based composites[239-241,175,242,163,243-245], polymers[160,246,247]

and perovskite oxide[248-252]. Among them, TMOs based anode materials including single, binary and hybrid metal oxides are widely used by researchers for the high performance of LIBs [253,254,138,255].

In comparison, zinc tungstate ($ZnWO_4$) and tin oxide (SnO_2) are promising anode material for lithium ion battery due to their high theoretical capacity (~700 and 782 mAh g^{-1}), low cost and easy availability [136,131,256,257]. Tin based materials show lower potential hysteresis than transition metal oxides. Also, oxides, alloys, sulfides and other compounds of tin based materials have gained attention as electrode material. Among them, tin oxide (SnO_2) was able to electrochemically react with Li and considered as a capable host for Li-ion storage [258]. However, $ZnWO_4$ and SnO_2 anode materials also have some disadvantages like, pulverization of electrodes, capacity fading during cycling, poor electrical conductivity and intense volume changes leading to poor rate capability. Therefore, to improve the properties of anode material, researchers have focused on hybrid metal oxide. Li-Li Xing et al.,[133] prepared $SnO_2/ZnWO_4$ Core–Shell Nanorods by two step method. The comparison of the electrochemical performance of bare $ZnWO_4$ nanorods and $SnO_2/ZnWO_4$ core shell nanorods, reveals that, $SnO_2/ZnWO_4$ core shell nanorods have higher reversible capacity than bare $ZnWO_4$, however, the cycling performance of $ZnWO_4$ is much better than $SnO_2/ZnWO_4$ core shell nanorods for 50 cycles. Low cycling performance of the $ZnWO_4/SnO_2$ material as an anode material for LIB is still stuck for the industrialization process. To overcome these issues, graphene, graphene oxide (GO) and reduced graphene oxide (r-GO), carbon nanotube (CNT) and carbonaceous materials are used as buffers [259,260]. Buffers can decline the mechanical stress formed by the volume change of the material and improve the contact and conductivity of the materials. Owing to the high surface area, good mechanical flexibility and good electrical conductivity, r-GO has been most considered for fabricating the composites.

In chapter 3, we have compared the electrochemical properties of $ZnWO_4$ nanorods and $ZnWO_4$@r-GO nanocomposite. Herein, we report the facile solvothermal synthesis of $ZnWO_4/SnO_2$@r-GO nanocomposite as an anode material for LIBs. The detailed electrochemical properties of the prepared $ZnWO_4/SnO_2$ and $ZnWO_4/SnO_2$@r-GO nanocomposite were studied and compared. Further, to boost the efficiency and electrochemical performance of $ZnWO_4/SnO_2$, GO was added. The synergetic effects of each

metal oxide along with GO improves the capacity than $ZnWO_4/SnO_2$ nanocomposite. To the best of our knowledge there are no reports on $ZnWO_4/SnO_2$@r-GO nanocomposite as an anode material for LIBs.

4.2 SYNTHESIS AND PHYSIOCHEMICAL ANALYSIS

4.2.1 Preparation of $ZnWO_4$

$ZnWO_4$ was prepared by following the method explained in the chapter 3. To prepare $ZnWO_4$, 0.35g of $Na_2WO_4.2H_2O$ (98%) and 0.523 g of $(CH_3COO)_2Zn.2H_2O$ were added separately to 50 ml (1:1 v/v) of $C_2H_6O_2$ and distilled water and stirred for 15 min. The two solutions were mixed together and again stirred for 15 min. Obtained white solution was transferred into a teflon jar for hydrothermal reaction at 180°C for 24 h, followed by cooling to room temperature. Resultant solution was collected and washed several times with distilled water, ethanol and acetone to remove the impurities. Collected samples were dried overnight at 65°C in a vacuum oven.

4.2.2 Preparation of SnO_2

SnO_2 nanoparticles were prepared using the hydrothermal method. $SnCl_4.5H_2O$ was introduced into a solution containing 2-propanol and distilled water in the ratio 4:1. The solutions were adjusted to pH 13 by the addition of NaOH, and then transferred to a stainless autoclave, and heated at 150°C for 24 h and cooled to room temperature. Obtained solution was washed with distilled water, ethanol and acetone several times. Finally, the sample was collected and dried overnight at 60°C in a vacuum oven.

4.2.3 Preparation of $ZnWO_4/SnO_2$ nanocomposite:

To prepare $ZnWO_4/SnO_2$ nanocomposite, preparation procedure of $ZnWO_4$ was carried out by adding 8.975 mg and 17.95 mg of prepared SnO_2 nanoparticles respectively. Correspondingly the samples were termed as ZWSN-5 and ZWSN-10.

4.2.4 Preparation of ZnWO₄/SnO₂@r-GO nanocomposite

Using modified Hummers method, GO was prepared as reported by our previous study [196,195,262]. To prepare the $ZnWO_4/SnO_2$@r-GO nanocomposite, preparation procedure of $ZnWO_4/SnO_2$ nanocomposite was performed with the inclusion of 0.5 mg GO. The sample is named as ZWSN-10/GO nanocomposite.

4.3 Results and Discussion

4.3.1 Structural, morphological and chemical analysis
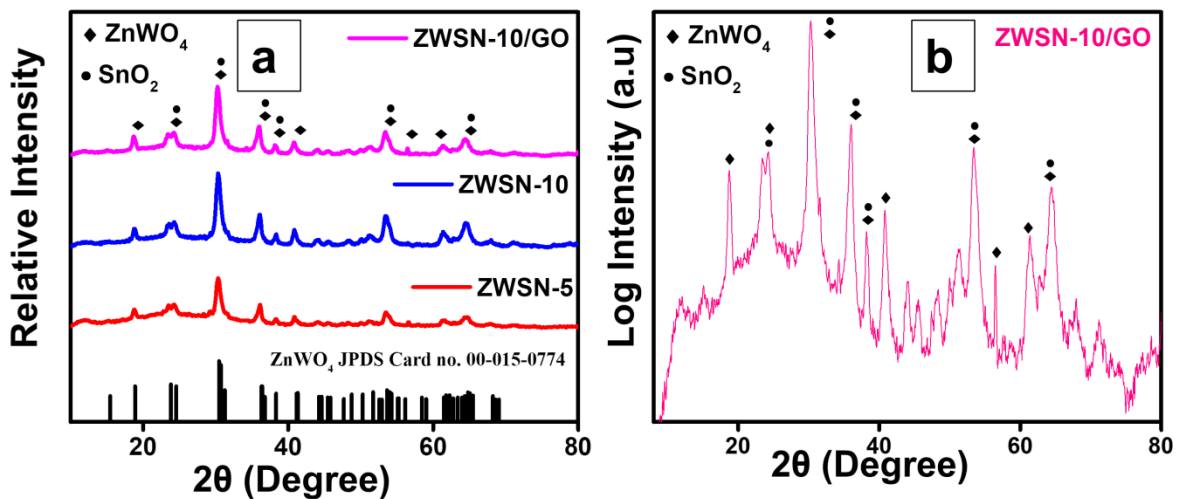
Figure 4.1 (a) XRD pattern of the ZWSN-5, ZWSN-10 and ZWSN-10/GO nanocomposites and (b) log intensity XRD pattern of the ZWSN-10/GO nanocomposites.

Figure 4.1(a) depicts the X-ray diffraction pattern of the as prepared ZWSN-5, ZWSN-10 and ZWSN-10/GO nanocomposites. The diffraction pattern of the $ZnWO_4$ has monoclinic Wolframite structure and matches with the JCPDS Card No.00-015-0774 as reported elsewhere[263]. We can observe several new peaks in the composite at 34.35°, 42.61°, 67.81° and 71.34°, which can be indexed to (002), (112), (041) and (223) planes of SnO_2 and matches with the JCPDS Card No. 00-029-1484. This result confirms the formation of $ZnWO_4/SnO_2$. The hump at 12.04° and a broad peak at around 20° to 28° confirm the presence of r-GO in $ZnWO_4/SnO_2$. These results indicate the formation of ZWSN-10/GO nanocomposites. Further, to verify the presence of graphene oxide in the ZWSN-10/GO nanocomposites, Raman

spectroscopy was performed and shown in the Figure 4.2 (c). As shown in the Figure 4.2 (c), D and G bands appear at 1349 and 1599 cm^{-1} respectively, which suggests the existence of graphene oxide in the ZnWO$_4$/SnO$_2$@r-GO composite. And also, the characteristic peaks of ZnWO$_4$ (905 and 547 cm^{-1}) and characteristic peaks of SnO$_2$ (478 and 641 cm^{-1}) are observed in all Raman spectra represented in the Figure 4.2 (a, b)[264,192,265,266].
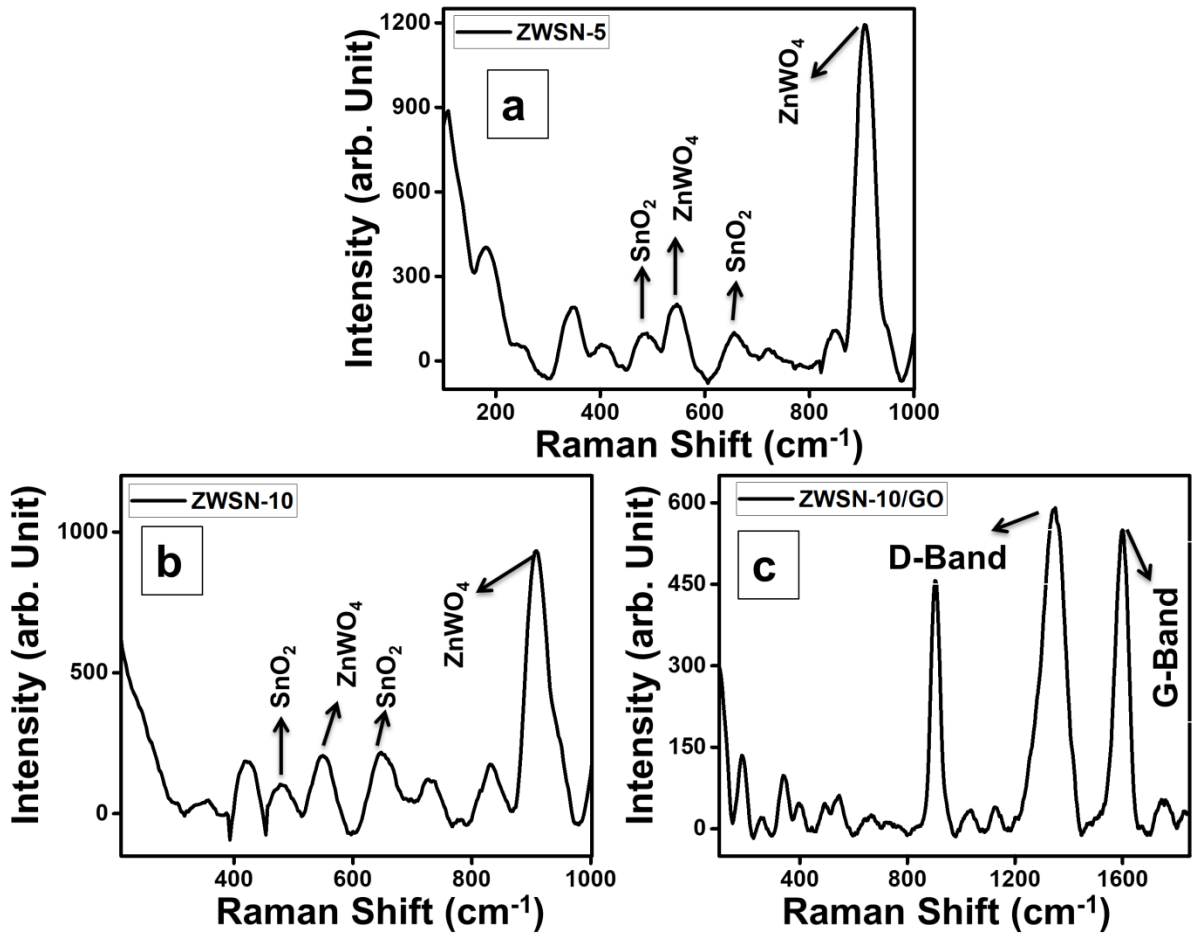
Figure 4.2 (a, b, c) Raman spectra of ZWSN-5, ZWSN-10 and ZWSN-10/GO nanocomposites

Further, to verify the amount of carbon content in ZWSN-10/GO nanocomposite, TGA was carried out in air atmosphere upto 700 °C which represented in Figure 4.3. From the TGA curve, the initial weight loss upto 60 °C may be due to the surface bound molecules and moisture in the ZWSN-10/GO nanocomposite. Significantly, the weight loss from 60 to 500

°C is due to the incineration of amorphous carbon and graphene. The amount of carbon in the ZWSN-10/GO nanocomposite is about ~4 wt%.
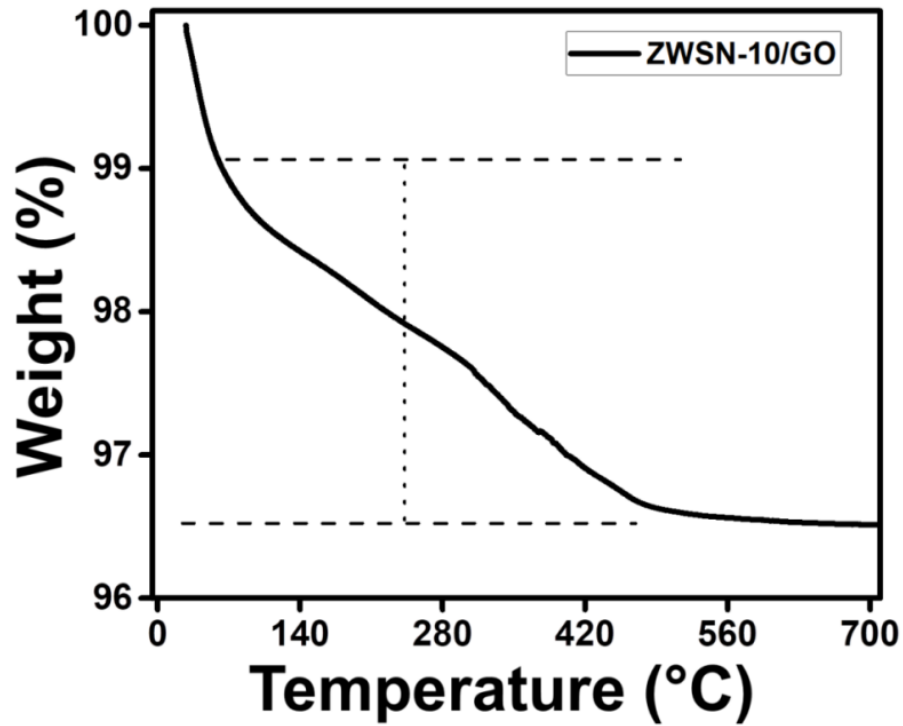
Figure 4.3 TGA curves of the ZWSN-10/GO nanocomposites from room temperature to 700 °C in the air atmosphere.

The elemental analysis and morphology of the prepared ZWSN-5, ZWSN-10 and ZWSN-10/GO nanocomposites were investigated using EDAX and FESEM. Figure 4.4 represents the FESEM images of the (a) ZWSN-5, (b) ZWSN-10 and (c) ZWSN-10/GO nanocomposites. FESEM images of all three samples shows non-uniform agglomerated nanorods.
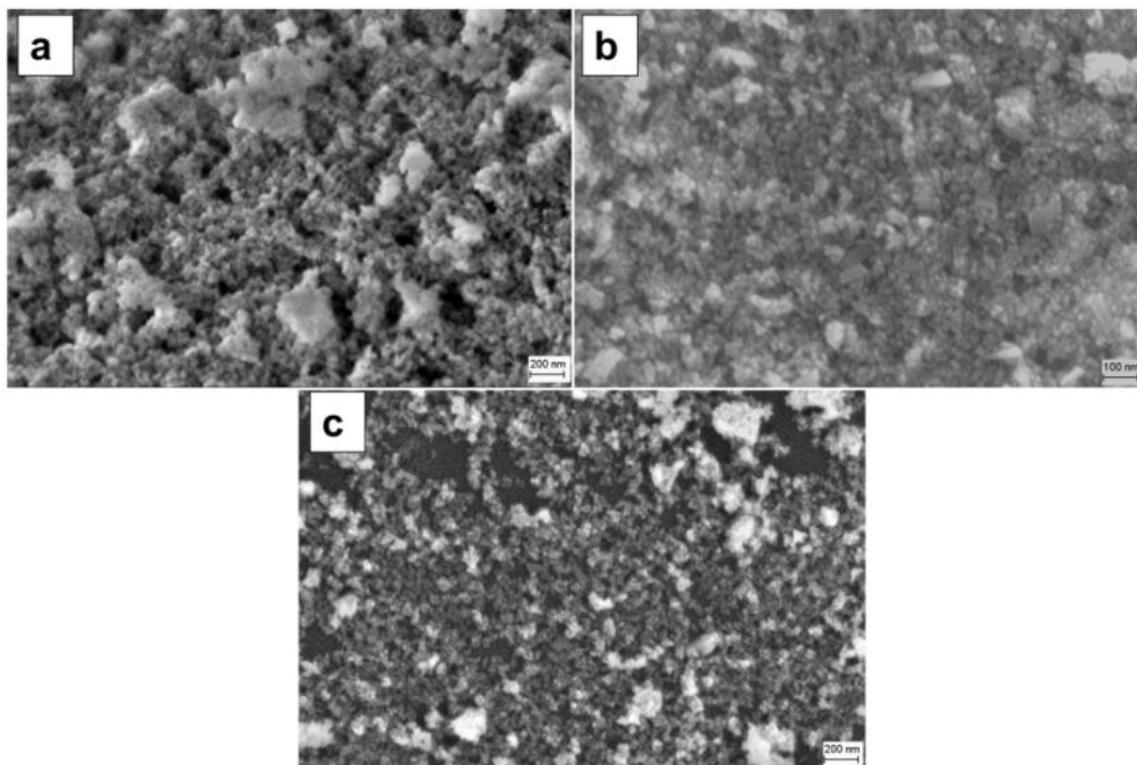
Figure 4.4 FESEM images of (a) ZWSN-5 (b), ZWSN-10 and (c) ZWSN-10/GO nanocomposites.

The FESEM image of the SnO_2 is presented in the Figure 4.5. The EDAX spectra of ZWSN-5, ZWSN-10 and ZWSN-10/GO nanocomposites represents the peaks corresponding to zinc, tungsten, oxygen, tin and carbon, which is shown in the Figure 4.4. From Figure 4.5, we can observe a carbon peak with significant intensity which could be attributed to the occurrence of carbon from graphene. From the EDAX spectra of ZWSN-5, ZWSN-10 and ZWSN-10/GO nanocomposites we can observe that, there are no significant impurities. The obtained atomic percentage of elements from the EDAX mapping is represented in the Figure 4.5.
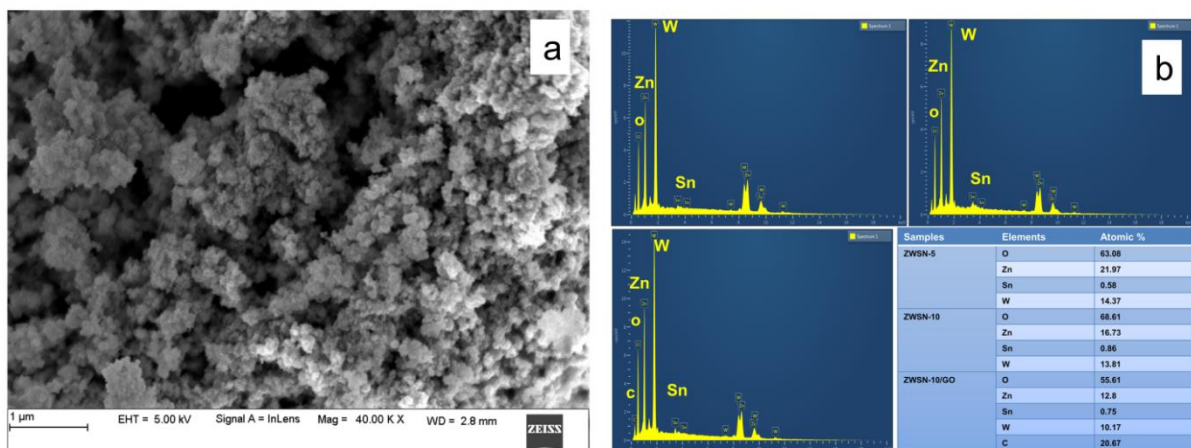
Figure 4.5 The morphology of the SnO$_2$ using ZEISS SIGMA VP Field Emission Scanning Electron Microscopes (FE-SEM) from Carl Zeiss Microscopy image. EDAX images of the ZWSN-5, ZWSN-10 and ZWSN-10/GO nanocomposites. Elements and their atomic percentage representation

TEM analysis of ZWSN-5, ZWSN-10 and ZWSN-10/GO nanocomposites is represented in the Figure 4.6 (a, d, g) and confirms the nanorod-like structure and also specifies there is no much change in the morphology. Further, TEM image of the ZWSN-10/GO nanocomposites in Figure 4.6 (g) confirms the growth of the ZWSN-10 composites over the graphene sheet. Also Figure 4.6 (b, e, h) represents the HRTEM images of ZWSN-5, ZWSN-10 and ZWSN-10/GO nanocomposites. Figure 4.6 (h) reveals the fringes with a lattice spacing value of 0.25 and 0.47 nm, corresponding to the (021) and (100) planes of SnO$_2$ and ZnWO$_4$ respectively, which matches well with the XRD analysis results. The ring type SAED pattern of ZWSN-5, ZWSN-10 and ZWSN-10/GO nanocomposites is depicted in the Figure 4.6 (c, f, i). The ring SAED pattern confirms the polycrystalline nature of the ZWSN-5, ZWSN-10 and ZWSN-10/GO nanocomposites, which agrees with the XRD results.
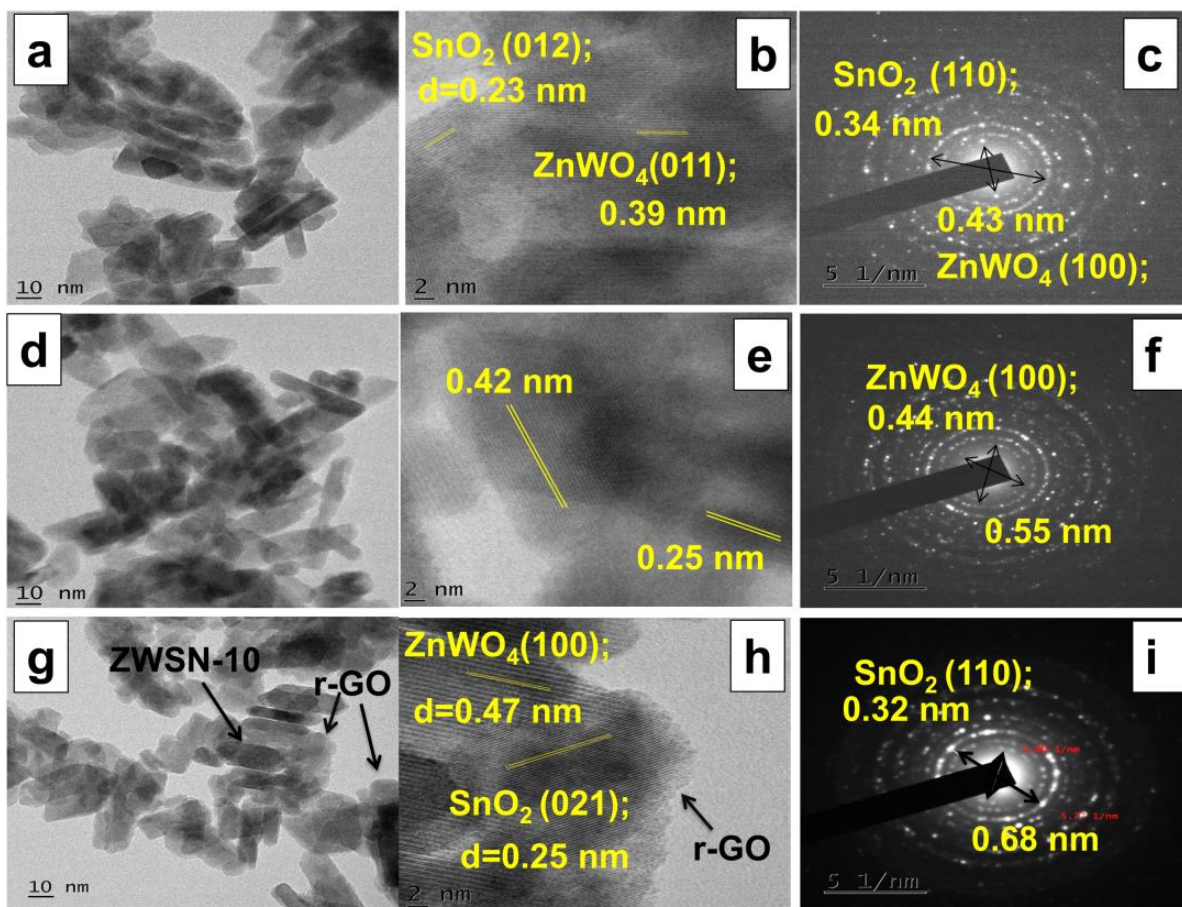
Figure 4.6 TEM, HRTEM and SAED patterns of (a, b, c) ZWSN-5, (d, e, f) ZWSN-10 and (g. h, i) ZWSN-10/GO nanocomposites.

Further, to investigate the chemical state of the elements in the ZWSN-10/GO nanocomposites, XPS technique was performed. The wide range XPS survey spectra depicted in the Figure 4.7 (a) illustrates the presence of Zn, O, Sn, C and W and is consistent with EDAX results. Using C 1s peak (284.6 eV), XPS spectra was calibrated. Figure 4.7 (b) represents the high-resolution spectra (HR spectra) of Zn 2p, which were fitted with 1021.4 eV (Zn $2p_{3/2}$) and 1044.5 eV (Zn $2p_{1/2}$) indicating the presence of Zn^{2+} ions in $ZnWO_4$[201]. The high-resolution spectrum of W 4f consists of two spin–orbit doublets with the binding energy peaks at 35.32 eV for W $4f_{7/2}$ and 37.42 eV for W $4f_{5/2}$ as represented in Figure 4.7 (c). To study the reduction degree of oxygen containing functional groups in graphene oxide, C 1s spectrum is a useful approach. In deconvoluted C 1s spectrum (Figure 4.7 (d)), the two peaks assigned to C-C (284.5 eV) and C=O (288.1 eV) groups represent r-GO plane. The C-C band has higher intensity than that of oxygen containing functional groups, which interprets the chemical reduction of GO[267].

71

Furthermore, the high resolution XPS spectra of Sn 3d represented in the Figure 4.7 (f), shows two peaks at 486.64 eV and 497.64 eV corresponding to Sn $3d_{5/2}$ and Sn $3d_{3/2}$ states. The binding energy of the Sn $3d_{5/2}$ peak at 486.64 eV indicates the presence of SnO_2[268]. Similarly, Figure 4.7 (e) illustrates the high resolution spectra of O 1s of ZWSN-10/GO nanocomposites. This exhibits three deconvoluted peaks at 529.6, 531.4 and 532.6 eV corresponding to either oxygen coordination in Zn-O, hydroxyl/epoxy groups of r-GO and Zn–O–C bonds of $ZnWO_4$ or O-Sn bond and Sn-O-C bonds of SnO_2 [269,261]. Based on the analysis, we can conclude that, $ZnWO_4$, SnO_2 and r-GO exists in the ZWSN-10/GO nanocomposite surface.
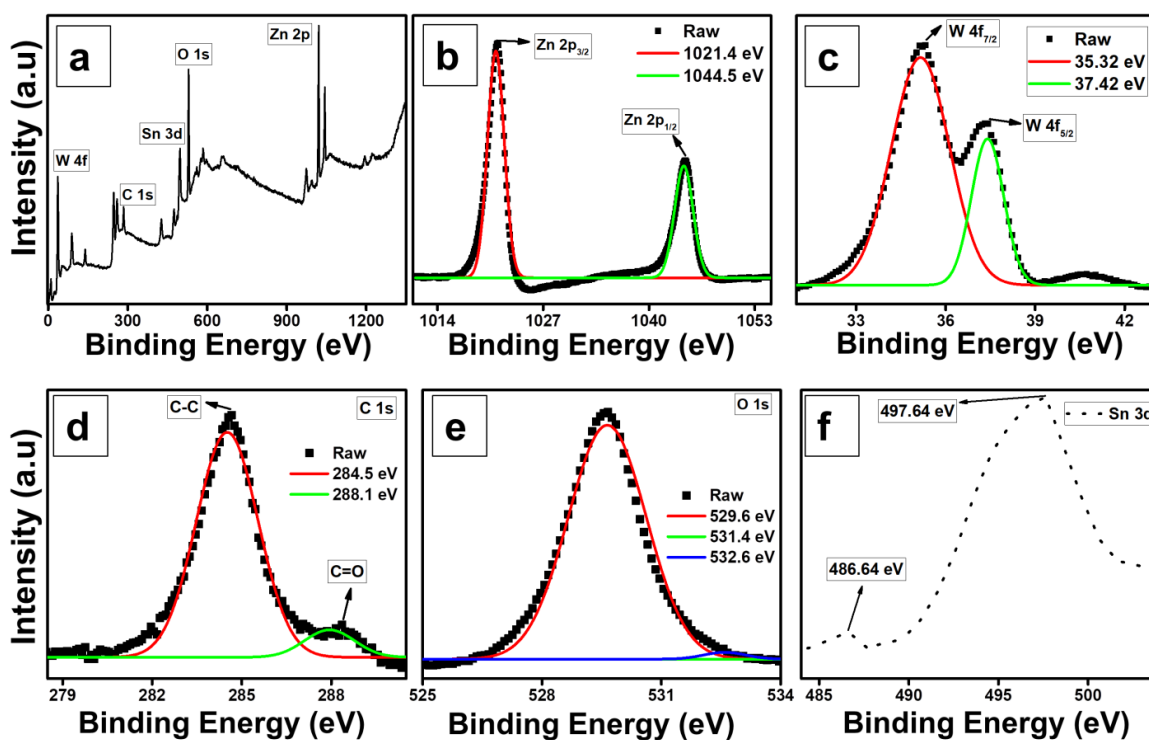
Figure 4.7 (a) XPS survey Spectra of ZWSN-10/GO nanocomposites and (b-f) HR spectra of Zn 2p, W 4f, C 1s, O 1s, and Sn 3d.

The N_2 adsorption/desorption isotherms of synthesized ZWSN-5, ZWSN-10 and ZWSN-10/GO nanocomposites are depicted in the Figure 4.8. This also shows the BET surface areas as 41.171, 46.032 and 49.341 m^2 g^{-1} respectively. The prepared sample represents IV isotherm type, and is mesoporous powder. The ZWSN-10/GO has larger surface area than that of ZWSN-5 and ZWSN-10. The r-GO and increased amount of SnO_2 increase the surface area of

the ZWSN-10/GO nanocomposite. The average pore diameters of ZWSN-5, ZWSN-10 and ZWSN-10/GO nanocomposites are 11.142, 10.939 and 10.9152 nm respectively. This mesoporous size is useful to improve the electrochemical reaction, hasten the reaction rate and diffusion of electrons and ions to some extent. The pore size distribution was represented in the Figure 4.8 (Inset).
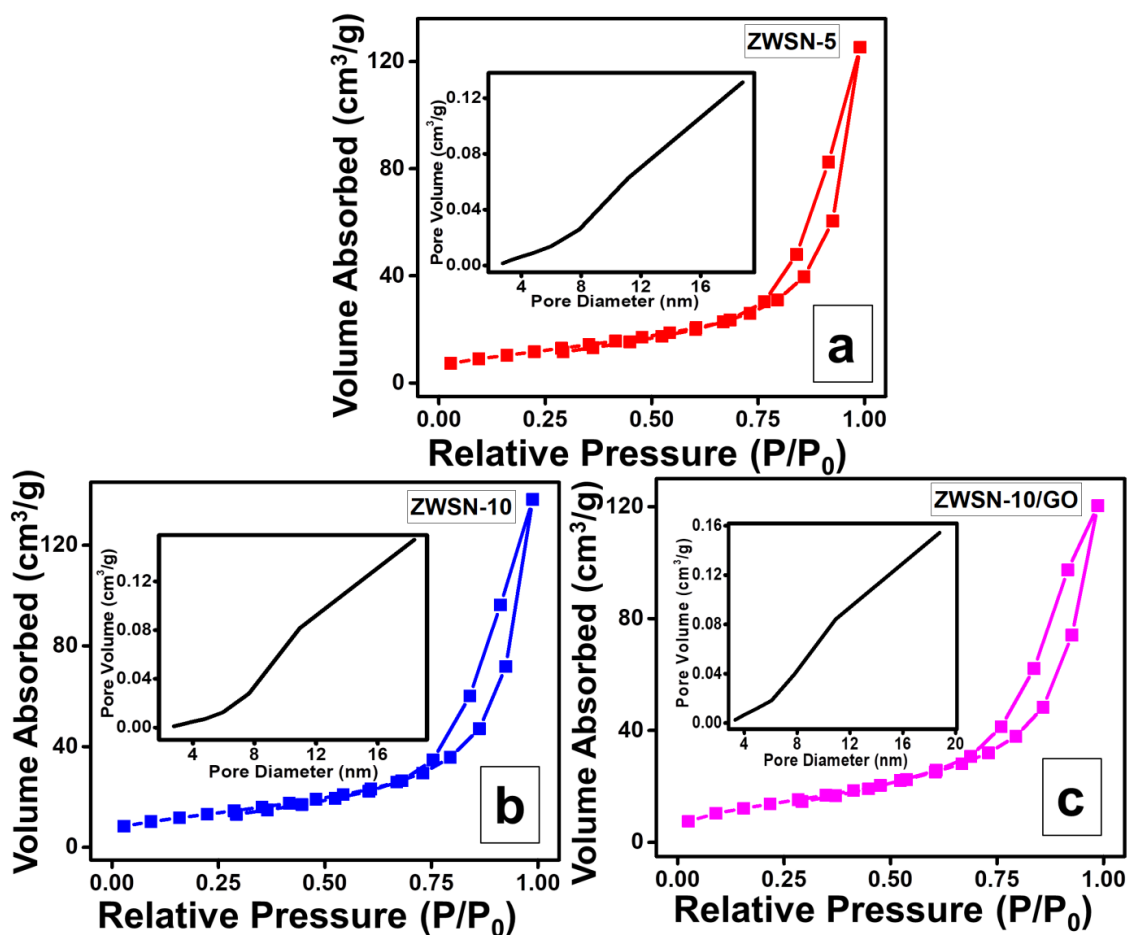
Figure 4.8 N$_2$ absorption-desorption isotherms of (a) ZWSN-5, (b) ZWSN-10 and (c) ZWSN-10/GO nanocomposite (corresponding pore size distribution was represented as inset)

4.3.2 Electrochemical measurements

To investigate the electrochemical property of the prepared nanocomposites, CV was performed. Figure 4.9 (a) represents the CV curves of the prepared ZWSN-5, ZWSN-10 and ZWSN-10/GO nanocomposites at a scan rate of 0.1 mV s^{-1} in the voltage range 0.02 to 3 V versus Li/Li$^+$. From the figure, the first reduction peaks occurred at ≈0.6 V and ≈1.2 V are

equivalent to the reduction of Zn^{2+} and W^{6+} respectively. The other minor peaks observed at reduction peaks are possibly due to the formation of solid electrolyte interface (SEI) film on the electrode surface and also the formation of Zn-Li alloy. The peaks in CV curves of all prepared ZWSN-5, ZWSN-10 and ZWSN-10/GO nanocomposite electrodes are identical indicating that similar reaction occurs in all anode materials. The oxidation peak observed around 0.6 V is interrelated with the de-alloying reaction of Zn-Li. The peak from 0.9 to 2 V resembles to the oxidation of Zn^0 to Zn^{2+} and WO_3 to W^{6+} along with decay of the Li_2O matrix. From the Figure 4.9 (a), it is evident that, the integrated area of the ZWSN-10/GO nanocomposite is to some extent greater than that of ZWSN-5 and ZWSN-10, which specifies large capacity, eventuated during the lithium ion extraction and intercalation in the cycling. This is because of the inclusion of r-GO and SnO_2 into $ZnWO_4$, which improves the electronic conductivity. The reactions of the $ZnWO_4$ can be summarized as follows, based on the above discussion [139]:

$$ZnWO_4 + 8Li^+ + 8e^- \rightarrow Zn + W + 4Li_2O \tag{4.1}$$

$$Zn + Li^+ + e^- \leftrightarrow LiZn \tag{4.2}$$

$$LiZn + W + 3\,Li_2O \leftrightarrow Zn + WO_3 + 6Li^+ + 6e^- \tag{4.3}$$
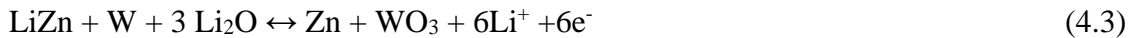
During the lithiation/delithiation process we can observe several peaks as shown in the Figure 4.9 (a). The peaks around 1.2 V is derived from Li_2O formation in the reaction between SnO_2 particles and Li^+[133]. The peak around 0.6 V related to the formation of Li_xSn. The lithiation / de-lithiation reactions of SnO_2 are given in the equation (4.4) and (4.5)[253,270,271].

$$SnO_2 + 4Li^+ + 4e^- \rightarrow SnO + 2Li_2O \tag{4.4}$$

$$Sn + xLi^+ + xe^- \leftrightarrow Li_xSn\ (0 \leq x \leq 4.4) \tag{4.5}$$
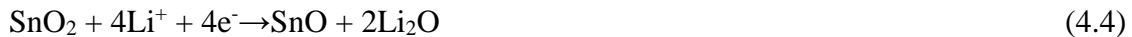
SnO_2 can produce extra Li_2O, which leads to large irreversible lithium storage capacity for SnO_2. In our nanocomposite, W metal cluster and GO can make this extra Li_2O reversibly convert to Li^+ and activate the irreversible capacity. The synergetic effect between nanostructured $ZnWO_4$, SnO_2 and GO leads to the high reversible capacity of the nanocomposites. The total reaction can be as follows[133],

LiZn + xLi$_y$Sn +W + (3 + 2x) Li$_2$O ↔ Zn + xSn + WO$_{3 + 2x}$ + (7 + 8.4x)Li$^+$ + (7 + 8.4x)e$^-$

(6)
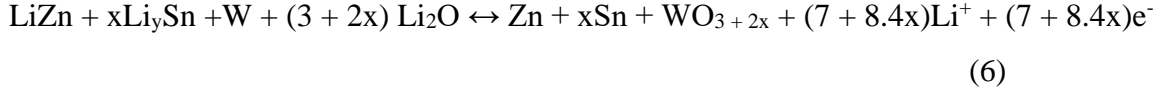
Equation (6) is a simplified expression. Importantly, W metal clusters cannot react with all of Li$_2$O.

The electrochemical performance of the as prepared ZWSN-5, ZWSN-10 and ZWSN-10/GO nanocomposite was studied by fabricating 2032 coin cells with prepared nanocomposites as anode materials and Li metal as counter electrode. The charge/discharge curves was performed at a current density of 100 mA g^{-1} and potential window 0.02 – 3 V versus Li/Li$^+$ at room temperature as shown in the Figure 4.9 (b). The capacity of the first discharge curve of ZWSN-5, ZWSN-10 and ZWSN-10/GO nanocomposite was noticed as 882, 1316 and 1486 mAh g^{-1} respectively. It is clear that the capacity obtained is above the theoretical capacity of ZnWO$_4$ (684 mAh g^{-1}) and can be ascribed to the incorporation of SnO$_2$ and formation of SEI layer. The large surface area could cause to decompose more electrolytes, which form the solid electrolyte interface film. The charge capacity of the as prepared ZWSN-5, ZWSN-10 and ZWSN-10/GO nanocomposite was 367, 425 and 548 mAh g^{-1} respectively, at a current density of 100 mA g^{-1} at room temperature. We observe that charge/discharge capacity of the ZWSN-10/GO nanocomposite is higher than that of ZWSN-5 and ZWSN-10, due to the incorporation of SnO$_2$ and r-GO into ZnWO$_4$. The BET analysis supports the above observation, in which the surface area/pore volume increases, which in turn increases the lithiation and electrochemical activity of the ZnWO$_4$/SnO$_2$ effectively.
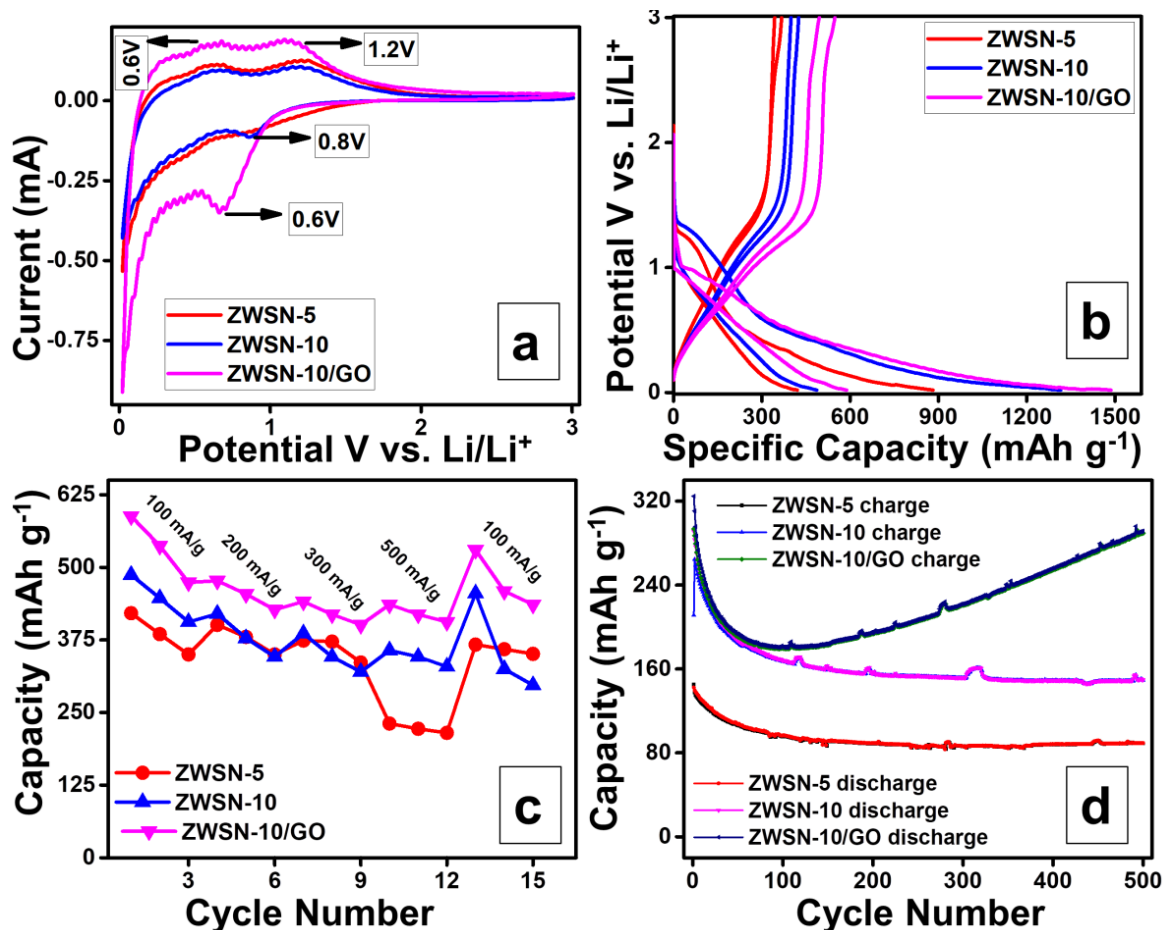
Figure 4.9 (a) CV representation (b) First two Charge/discharge curve (c) Rate capability plot and (d) Cyclability of the ZWSN-5, ZWSN-10 and ZWSN-10/GO nanocomposite.

In addition, to find out the advantage of the ZWSN-10/GO nanocomposite in lithium storage, the rate capability of ZWSN-5, ZWSN-10 and ZWSN-10/GO nanocomposite was further studied as shown in the Figure 4.9 (c). From the Figure 4.9 (c) it is clear that, the discharge capacity of the as prepared electrodes decreases with the increasing current density. It is notable that, the capacity of ZWSN-5, ZWSN-10 and ZWSN-10/GO nanocomposite was 418, 420 and 477 mAh g^{-1} respectively at 200 mA g^{-1} current density. This indicates that, extraction and insertion process of Li^{+} ions is reversible even at higher current density. Further, at higher current density (500 mAg^{-1}), the capacity of ZWSN-5, ZWSN-10 and ZWSN-10/GO nanocomposite electrodes are 231, 357 and 436 mAh g^{-1} and at lower current density (100 mA g^{-1}), the capacity are 367, 455 and 530 mAh g^{-1} respectively. This proves that samples regain almost its initial capacities indicating their good reversibility.
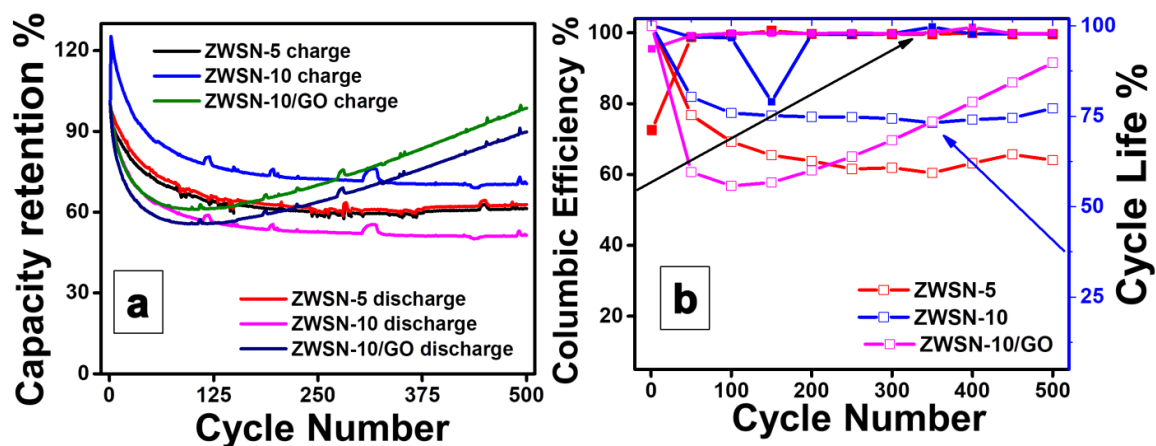
Figure 4.10 (a) Capacity retention versus cycle number plot (b) Cyclability of the ZWSN-5, ZWSN-10 and ZWSN-10/GO nanocomposite

To study the cyclic stability of the as prepared ZWSN-5, ZWSN-10 and ZWSN-10/GO nanocomposite electrodes, galvanostatic charge/discharge (GCD) was performed at a current density of 300 mA g^{-1} which is represented in the Figure 4.9 (d). Due to high surface area, there is an unwanted reaction of electrode and electrolyte which is the disadvantage of the nano-sized electrodes. Formation of the SEI layer causes the poor capacity retention during the initial cycles. The ZWSN-10/GO nanocomposite shows charge/discharge capacity of 294 and 325 mAh g^{-1} for first cycle at a current density of 300 mA g^{-1}. And also, ZWSN-10/GO nanocomposite shows 289 and 291 mAh g^{-1} charge/discharge capacity with 89% and 98% of capacity retention after 500 cycles. During the initial cycles ZWSN-10/GO nanocomposite shows poor capacity retention due to the reversible SEI film formation. After 200 cycles, the capacity starts to increase and reaches approximately near to initial value with a columbic efficiency of 99%. There is an upward trend after dramatic capacity drop during initial charge/discharge cycles. This situation is caused by matter factors, such as SEI, nanosized particle, electrode morphology and confined structure of active materials; this can be called as activation of materials. Depending on the materials, activation time varies [272]. The ZWSN-10/GO nanocomposite has 55.7% cycle life upto 100th cycle and the cycle life increased to 89.8% for 500th cycle. The ZWSN-10/GO nanocomposite exhibits good cycle life even after 500 cycles than ZWSN-5 (62.8 %) and ZWSN-10 (77.1 %) as represented in the Figure 4.10. High columbic efficiency of ZWSN-10/GO nanocomposite is also obtained and these results

77

strongly recommend the application of ZWSN-10/GO nanocomposite as anode material for LIBs. Table 4.1 shows the comparison of performance of the prepared electrodes and reported hybrid metal oxide composite based anode materials.

Table 4.1 Comparison of reported hybrid metal oxide with the prepared composite

Sl No	Electrode	Discharge Capacity (mAh/g)	Charge Capacity (mAh/g)	Current Density / C-rate	Ref
1	$SnO_2/ZnWO_4$ Core–Shell Nanorods	1318		C/20	[133]
2	α-Fe_2O_3@SnO_2 core-shell nanoparticles	895	791	50 mA/g	[273]
3	Porous Fe_2O_3/SnO_2 nanocubes	1481.6		100 mA/g	[274]
4	SnO_2–In_2O_3/GNS nanocomposite	1682	962	60 mA/g	[275]
5	ZWSN-10/GO nanocomposites	1486	548	100 mA/g	Present work

To further investigate the kinetics and electrochemical behavior of the as prepared nanocomposites, EIS was performed in the frequency range of 1 mHz to 50 kHz as shown in the Figure 4.11. The EIS spectra of the ZWSN-5, ZWSN-10 and ZWSN-10/GO nanocomposite were obtained after three cycles of CV characterization. Nyquist plot consists of a semicircle in the medium higher frequency region and an oblique line in the lower frequency region. The reaction resistance of the SEI layer and charge transfer resistance is the reason for the semicircle. Solid- state diffusion of lithium ions in active material is associated with the line in low frequency region. The radius of the semicircles is declining for the ZWSN-10/GO nanocomposite, which represents the quicker kinetic process of the ZWSN-10/GO nanocomposite than ZWSN-5 and ZWSN-10 electrode. The inclusion of SnO_2 and r-GO significantly advances the conductivity of $ZnWO_4$ which also improves the electrochemical activity of the composites.
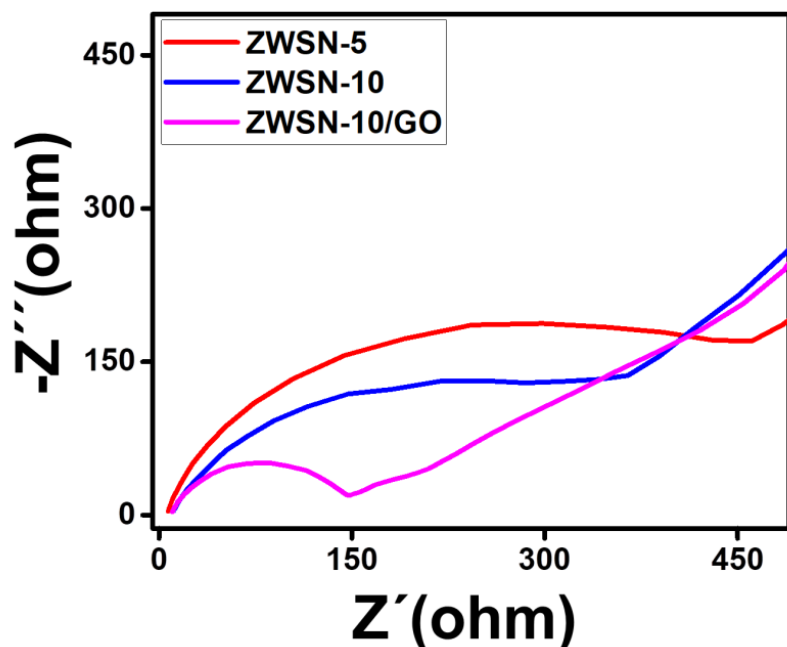
Figure 4.11 Nyquist plot of ZWSN-5, ZWSN-10 and ZWSN-10/GO nanocomposite

Further to study the crystal structure of ZWSN-5, ZWSN-10 and ZWSN-10/GO nanocomposite after 500 cycles, ex-situ XRD was performed and represented in the Figure 4.12 (a-b). We can observe that there are some peaks missing in the XRD plot, which elucidates the destruction of $ZnWO_4/SnO_2$ nanocomposite. The changes in XRD peaks of the ZWSN-5, ZWSN-10 and ZWSN-10/GO nanocomposite before and after 500 cycles specifies the electrochemical reactions of the SnO_2, $ZnWO_4$ and Li have taken place according to the equation (6). There are some new peaks at 43.22°, 50.36° and 74.06° due to the copper foil[276] and also there are several new peaks at 24.88° and 35.76° that resemble to tungsten, which match with the JCPDS Card No. 03-065-6453 and tungsten oxide (JCPDS Card No. 00-041-1230), 18.26° and 29.98° corresponding to SnO (JCPDS Card No. 01-085-0712), 39.13° corresponding to Zinc (JCPDS Card No. 00-001-1238) and 33.42° indexed to LiO_2[133].

To study the effect of cycling on the morphology of ZWSN-10/GO nanocomposite, after 500 cycles, ex-situ FE-SEM was performed as shown in the Figure 4.12 (b). We can observe from the Figure 4.12 (b) that dendrites are formed during the charge/discharge cycles, however, there is no drastic change in the morphology of the ZWSN-10/GO nanocomposite, which implies the greater stability of the material.
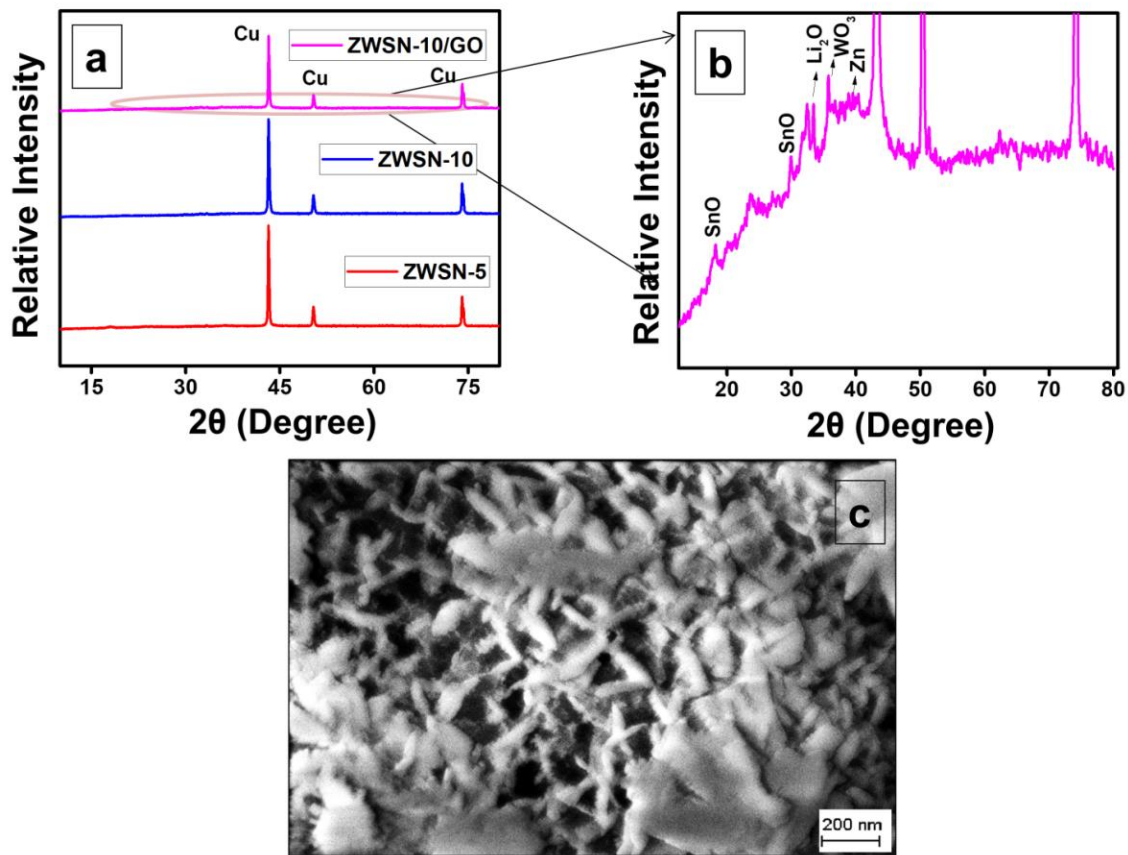
Figure 4.12 (a) Ex-situ XRD pattern of the ZWSN-5, ZWSN-10 and ZWSN-10/GO nanocomposite. (b) Zoomed XRD image of ZWSN-10/GO nanocomposite. (c) FE-SEM image of the ZWSN-10/GO nanocomposite after 500 cycles.

4.4 SUMMARY

- The $ZnWO_4/SnO_2$ and $ZnWO_4/SnO_2$@r-GO nanocomposite were prepared by facile solvothermal method and characterized using XRD, SEM, HRTEM, EDAX, BET and XPS for structural, elemental and morphology.

- Raman analysis confirms the presence of characteristic peaks of $ZnWO_4$, SnO_2 and r-GO in the $ZnWO_4/SnO_2$@r-GO nanocomposite

- TGA results infer the amount of carbon in the ZWSN-10/GO nanocomposite is about ~4 wt%.

- TEM images confirms the nanorod-like structure and confirms the growth of the ZWSN-10 composites over the graphene sheet

- The prepared samples were used as anode material and characterized electrochemically using CV, charge/discharge and EIS.

- An enhancement in the capacity by incorporation of graphene is witnessed in ZWSN-10/GO nanocomposite, revealing 1486 mAh g^{-1} discharge capacity, which is 1.8 and 1.1 times greater than ZWSN-5 and ZWSN-10 respectively.

- The synergetic effect of SnO_2 and $ZnWO_4$ increases the discharge capacity of the composite, the addition of GO into the composite enhances the surface area, pore volume and electrochemical activity, resulting in high charge/discharge capacity, decent cycling stability and good rate capability of the $ZnWO_4/SnO_2$@r-GO nanocomposite.

CHAPTER 5

ZnWO$_4$/GeO$_2$@CNT NANOCOMPOSITE

FOR LITHIUM-ION BATTERY

APPLICATION

CHAPTER 5

ZnWO$_4$/GeO$_2$@CNT NANOCOMPOSITE FOR LITHIUM ION BATTERY APPLICATION

In this chapter, the synthesis of ZnWO$_4$/GeO$_2$@CNT nanocomposite and ZnWO$_4$/GeO$_2$ nanocomposites and their use as anode material for lithium ion battery are discussed. The structural and morphological studies are conducted using X-ray diffraction (XRD), scanning electron microscopy (SEM) and energy-dispersive X-ray spectroscopy (EDAX) and high-resolution transmission electron microscope (HRTEM). The electrochemical performance as anode material for lithium ion battery is characterized through cyclic voltammetry, galvanostatic charge/discharge and electrochemical impedance spectroscopy methods.

5.1 INTRODUCTION

Lithium-ion battery (LIB) plays a major role in the advanced portable electronics due to high energy density and stable cycling performance. There is a great market for high performance LIBs in the field of intelligent grid, electrical vehicles and hybrid electric vehicles. It is well known that, electrode materials are important factor to determine the performance of the LIBs. Over the decade, the lower theoretical capacity (372 mAh g^{-1}) graphene is used as anode for LIB, which is not suitable for the high energy density LIB[62]. So far, metal oxides[277,185,278], carbon materials[279,259,280], chalcogenides[281-283], perovskite oxide[284,285], ferrites[234,236,286], silicon based compounds[240,164,176,287,242,288,166] and polymers[160-162,246,247,289] are extensively reported as anode materials for LIB. To attain high specific capacity, rate capability and superior cycling a novel anode material has to be found out. Nowadays researchers are focused on hybrid metal oxides as anode material to overcome the above problems.

Among them, zinc tungstates (ZnWO$_4$) are attractive anode material for LIBs because of their good theoretical capacity (684 mAh g^{-1}), high conductivity and high specific area. The ZnWO$_4$ has been of great interest because W and Zn are electrochemically active for LIBs. From the lithium storage perspective, ZnWO$_4$ works both conversion reaction and alloying/dealloying reaction, which improves the capacity[139]. According to the previous report, Hyun-Woo

Shim and co-authors[131] showed that, $ZnWO_4$ nanorods have a reversible capacity of 420 mAh g^{-1} at a current rate of C/5 after 150 cycles. Shi Nian xiang and co-authors[139] prepared a $ZnWO_4$ hierarchical hexangular microstars as a anode material and revealed the first discharge and charge capacity of 777 mAh g^{-1} and 585 mAh g^{-1} respectively. Though, the large volume change and poor cycling performance of the $ZnWO_4$ is hindered as an anode material for LIB. Some literatures reported that, synergetic effect between two different materials enhances the capacity of tungstate material. Dr. Li-Li Xing and co-authors[133] synthesized $SnO_2/ZnWO_4$ Core–Shell Nanorods and reported 1000 mAh g^{-1} reversible capacity at C/20 rate.

Recently, Germanium oxide (GeO_x) has attracted increasing attention due to its high theoretical capacity (1600 mA h g^{-1}), high Li-ion diffusivity which is 400 times faster than in Si, fast charge carrier mobility and high electrical conductivity (100 times higher than Si) [290], which can deliver fast charge/discharge rate and improved cycle performance [291,292]. Germanium dioxide (GeO_2) is less expensive than elemental Ge. Because of the encouraging property of GeO_x several research works are reported. Wei Wei and co-authors[293] prepared porous hexagonal GeO_2 nanorods with good electrochemical results. They reported 1781/917 mA h g^{-1} initial discharge/charge capacity and also 747 mA h g^{-1} after 50 cycles. Wang and co-workers [294] synthesized a novel hierarchical GeO_x nanoporous structure. The GeO_x powder delivers ~1250 mA h g^{-1} reversible capacity after 600 cycles at 0.5C. However, GeO_x has some drawbacks such as large volume extension during charge/discharge and uninterrupted formation of solid-electrolyte interface (SEI) film causing capacity fading. Multiple tactics have been proposed to overcome the above problems including, the use of carbonaceous materials because they will improve the conductivity and contact of the GeO_2 material and amorphous carbon which increases the electrochemical performance of the GeO_2.

Carbon nanotubes (CNTs) have excellent electrochemical, mechanical and electrical properties due to their seamless connection in their hexagon structure and light weight. Wide application of CNTs in LIB is due to their high tensile strength, electrochemical property, high rigidity and low density [295,296]. Wu and co-workers[297] found that, CNT structure is a key factor that determines cycle life and specific capacity of LIB. The composite with CNT produces good results for the LIB. So far, limited reports are focused on hybrid type composite materials for

GeO$_2$ anodes. Bo Liu and co-workers[298] reported the synthesis of the novel GeO$_2$−SnCoC Composite as anode material. They have combined the long cycle life Sn−Co−C and high capacity GeO$_2$ to get an improved performance of LIB. The GeO$_2$−SnCoC Composite delivers 1501 and 1200 mAh g^{-1}, discharge/charge capacity with 80% columbic efficiency. Seung Ho choi and co-workers,[299] prepared Li$_2$O–B$_2$O$_3$–GeO$_2$ glass as anode for LIBs by spray pyrolysis method and reported Li$_2$O–B$_2$O$_3$–GeO$_2$ glass delivers 1629.8 and 531.7 mAh g^{-1} discharge/charge capacity for the first cycle.

In Chapter 3 and chapter 4, we discussed the electrochemical property of the ZnWO$_4$@r-GO and ZnWO$_4$/SnO$_2$@r-GO nanocomposite [300,57]. In this work, we propose a new anode material of metal oxide composite for LIB. This composite material is a mixture of ZnWO$_4$, GeO$_2$ and SWCNT and is prepared by facile single step solvothermal method. The ZnWO$_4$/GeO$_2$@CNT nanocomposite has the potential of combining the properties of ZnWO$_4$ (high capacity), GeO$_2$ (high capacity) and SWCNT (long cycle life). The detailed comparison of ZnWO$_4$/GeO$_2$ and ZnWO$_4$/GeO$_2$@CNT nanocomposite has been reported. The electrochemical property of the ZnWO$_4$/GeO$_2$ was studied and SWCNT was added to boost its performance. There is no report on the ZnWO$_4$/GeO$_2$@CNT nanocomposite to the best of our knowledge.

5.2 SYNTHESIS AND CHARACTERIZATION OF ZnWO$_4$/GeO$_2$@CNT NANOCOMPOSITE

5.2.1 Preparation of ZnWO$_4$

The ZnWO$_4$ was prepared as reported elsewhere[261]. The Na$_2$WO$_4$.2H$_2$O (0.35 g) and Zn(CH$_3$COO)$_2$.2H$_2$O (0.523 g) were taken separately with 1:1 (*v/v*) ratio of C$_2$H$_6$O$_2$ and double distilled water. The solutions are kept stirring for 15 min. Then, the zinc acetate dihydrate solution is poured drop-wise to the sodium tungstate dihydrate solution and stirred for another 15 min. Obtained precipitate is transferred into a Teflon jar containing stainless steel autoclave for reaction at 180 °C for 24 hours and then cooled to room temperature. The resultant solution is washed several times to eliminate the impurities. The collected samples are kept in vacuum oven at 80°C overnight for drying.

5.2.2 Preparation of ZnWO$_4$/GeO$_2$ nanocomposites

Preparation method of ZnWO$_4$ is repeated with the addition of Germanium (IV) oxide (≥99.99% trace metal basis) (Sigma Aldrich) with a molar ratio of 1:0.05 and 1: 0.1 and is represented as ZWGE5 and ZWGE10.

5.2.3 Preparation of ZnWO$_4$/GeO$_2$@CNT nanocomposite

To prepare the ZnWO$_4$/GeO$_2$@CNT nanocomposite, synthesis procedure of ZnWO$_4$/GeO$_2$ nanocomposites is repeated with the addition of 2 mg purchased SWCNT (Sigma Aldrich). The sample is denoted as ZWGEC.

5.3 RESULTS AND DISCUSSION

5.3.1 Structural and morphological characterization

The structure of the prepared ZWGE5, ZWGE10 and ZWGEC nanocomposite were determined by powder XRD and represented in the Figure 5.1 (a). The diffraction patterns of the ZWGE5, ZWGE10 and ZWGEC nanocomposite were indexed using Xpert high score plus software. The ZnWO$_4$ has Monoclinic Wolframite structure and matches with the PDF-2 Card no. 01-073-0554 as described chapter 3. It is clear from the Figure 5.1 (b), there are several new peaks at 25.8°, 38.46°and 61.46°, which can be indexed to (110), (201) and (302) planes of GeO$_2$ (PDF-2 Card no: 01-073-1306,) in the composite. The additional peaks confirm the formation of the GeO$_2$/ZnWO$_4$. We can also observe, peaks corresponding to CNTs (marked as ▼) in the ZWGEC nanocomposite. The intensity of the peaks decreased due to the growth of ZWGE10 in the CNTs, which confirms the formation of ZWGEC nanocomposite. Further, Raman spectroscopy was performed to verify the presence of CNT in the ZWGEC nanocomposite and represented in the Figure 5.1 (b). From the Figure 5.1 (b), the D and G band of CNT was observed at 1308 and 1590 cm^{-1} respectively. And also we can observe the characteristic peak of ZnWO$_4$ (903 cm^{-1})[187,192] and GeO$_2$ (233 and 270 cm^{-1})[301] which suggest the formation of the ZWGEC nanocomposite.
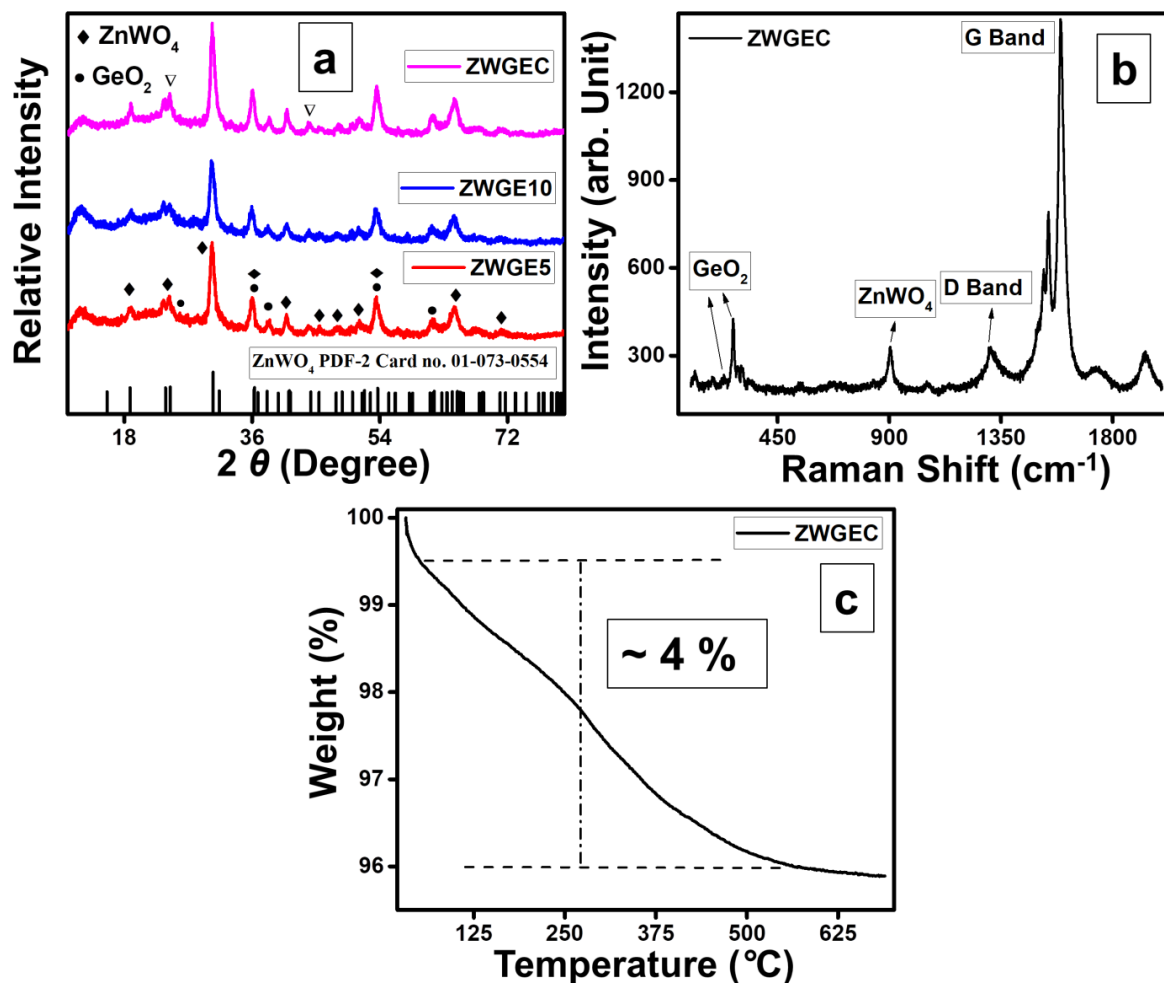
Figure 5.1 (a) XRD pattern of ZWGE5, ZWGE10 and ZWGEC nanocomposite (b) Raman spectra of ZWGEC nanocomposite and (c) TGA curve of ZWGEC nanocomposite.

Further, to investigate the carbon content in the ZWGEC nanocomposite, TGA was performed in air ambient upto 700 °C and represented in the Figure 5.1 (c). The initial minor weight loss is due to surface bound molecules and absorbed moisture in the ZWGEC nanocomposite. The drastic weight loss upto 550 °C is attributed to burning of the carbon content. The approximate amount of carbon content in the ZWGEC nanocomposite is about 4%.

To study the morphological features of the prepared ZWGE5, ZWGE10 and ZWGEC nanocomposite, FESEM was performed and represented in the Figure 5.2. We can notice non-uniform agglomerated nanorods with average length of 70-90 nm and width of 25-30 nm for

ZWGEC nanocomposite. All three samples appear as non-uniform agglomerated nanorods. To confirm the elemental composition of ZWGEC nanocomposite, EDAX was performed and represented in the Figure 2. The EDAX spectra peaks corresponding to the zinc, oxygen, tungsten, germanium and carbon with atomic percentage of the same was observed and represented in the Figure 5.2. We can observe the carbon peak with substantial intensity, which is ascribed to the presence of the carbon from the CNTs.

Sample	Elements	Atomic %
ZWGEC nanocomposite	Zn	8.90
	W	5.62
	O	56.90
	Ge	0.13
	C	28.45
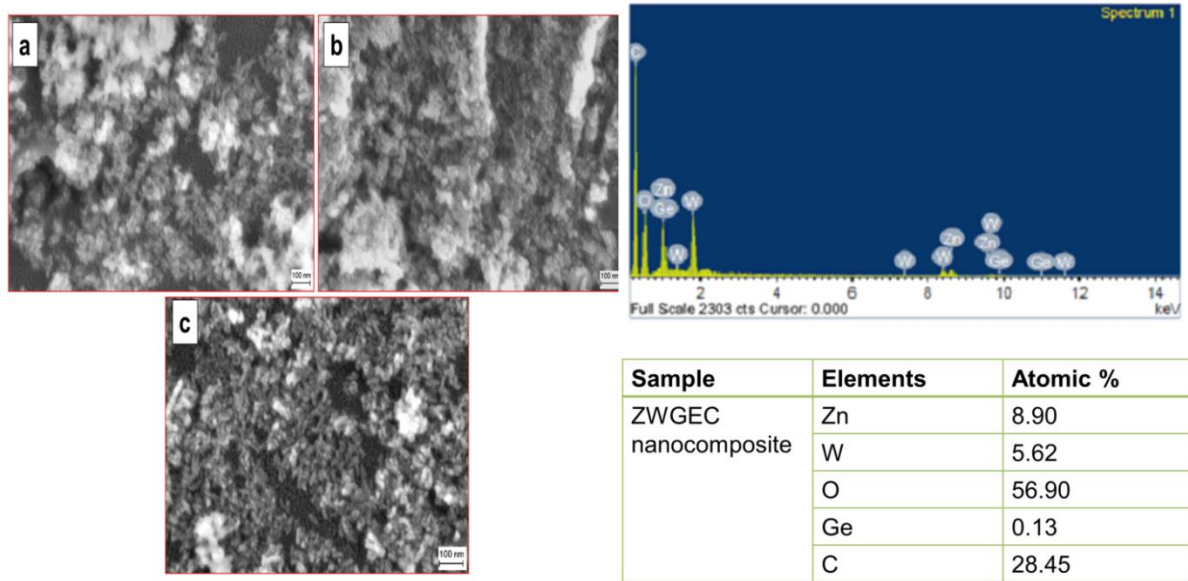
Figure 5.2 FESEM image of the (a) ZWGE5, (b) ZWGE10 and (c) ZWGEC nanocomposite. EDAX, elements and their atomic percentage representation of ZWGEC nanocomposite
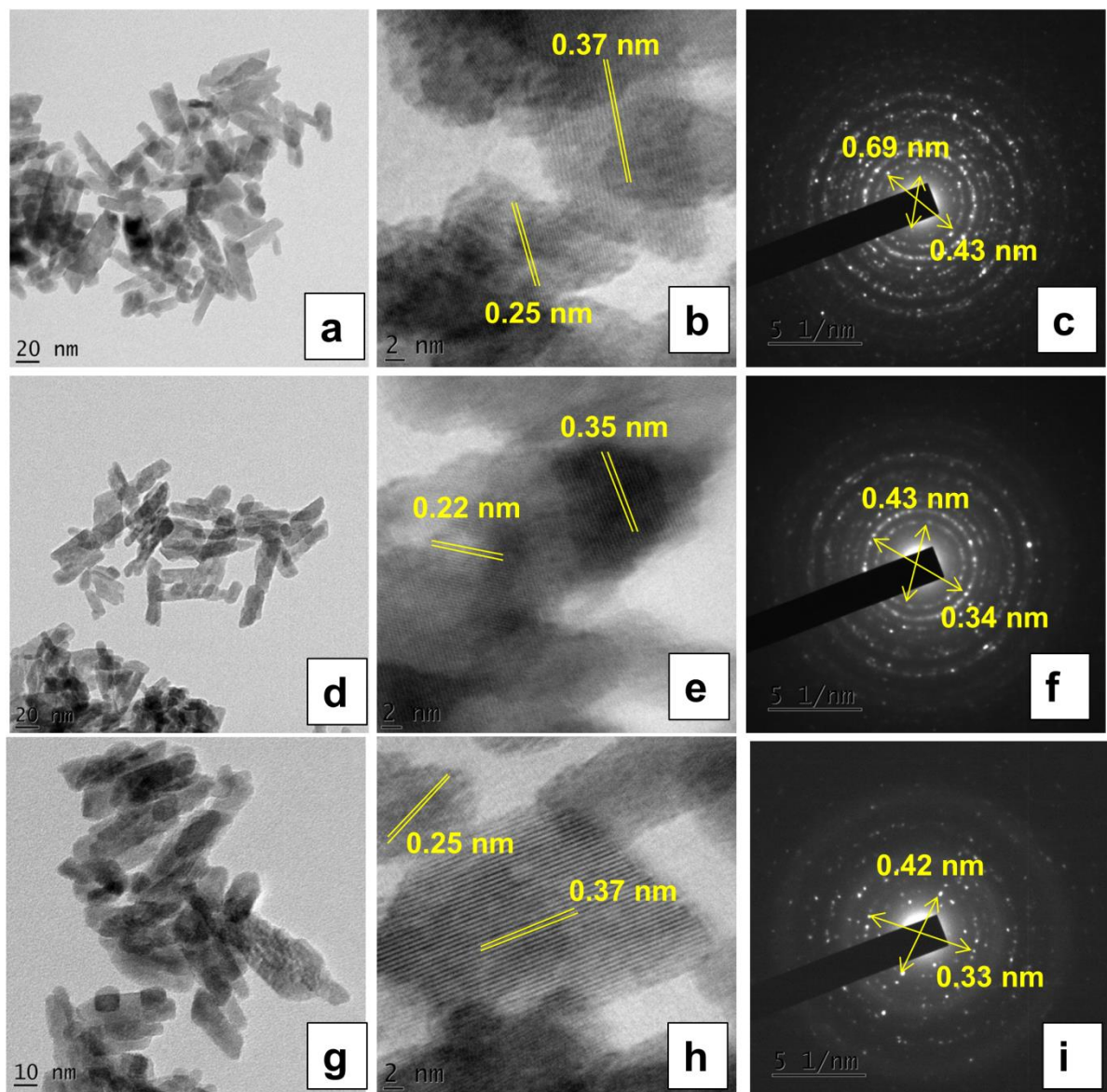
Figure 5.3 (a, d, g) TEM images, (b, e, h) HRTEM image and (c, f, i) SAED pattern of the ZWGE5, ZWGE10 and ZWGEC nanocomposite

Further, TEM analysis was performed to determine the morphologies of ZWGE5, ZWGE10 and ZWGEC nanocomposite and TEM images are represented in the Figure 5.3 (a, d, g). In Figure 5.3 (a, d, g), nanorods of ZWGE5, ZWGE10 and ZWGEC nanocomposite with a length of 30 – 70 nm and width of 10 – 20 nm observed. The identical morphology indicates that carbon nanotube does not affect the morphology of the ZWGEC. Raman and XRD studies show the presence of CNT in the composite and from the TEM we deduce that, ZWGE10

nanocomposites are grown around the CNT [302,303]. Also, Figure 5.3 (b, e, h) represents the HRTEM image of ZWGE5, ZWGE10 and ZWGEC nanocomposite with interplanar spacing of 0.25 nm and 0.37 nm corresponding to (112) planes of GeO_2 and (011) planes of $ZnWO_4$, 0.22 nm and 0.35 nm, and 0.25 nm and 0.37 nm corresponding to (112) planes of GeO_2 and (011) planes of $ZnWO_4$ respectively. This result matches with the XRD investigation. Further SAED pattern of the ZWGE5, ZWGE10 and ZWGEC nanocomposite shows the polycrystalline nature and matches well with the XRD results.

5.3.2 Electrochemical studies
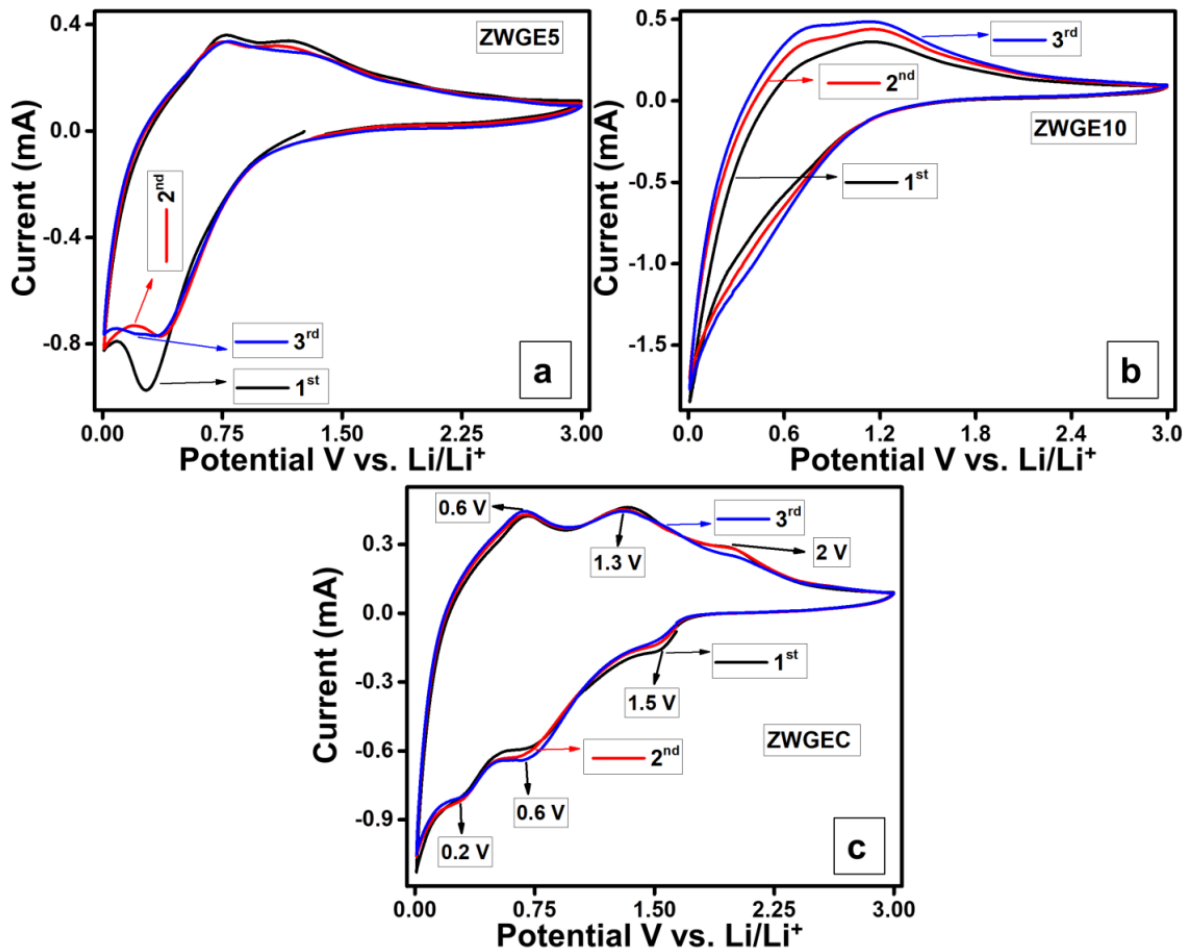
Figure 5.4 First three cycle CV of (a) ZWGE5, (b) ZWGE10 and (c) ZWGEC nanocomposite.

The electrochemical performance of the ZWGE5, ZWGE10 and ZWGEC nanocomposite was analyzed for the potential usage as anode material for LIBs. Figure 5.4 represents the first three

cycles of the ZWGE5, ZWGE10 and ZWGEC nanocomposite, CV performed at 1 mV s^{-1} in the voltage range of 0.01 – 3V versus Li/Li$^+$. We can observe almost identical peaks in CV curves for ZWGE5, ZWGE10 and ZWGEC nanocomposite electrodes, which suggest the similar reaction for all three anode materials. The reduction and oxidation peaks of ZnWO$_4$ were discussed in chapter 3. The reaction of ZnWO$_4$ is represented as below

$$ZnWO_4 + 8Li^+ + 8e^- \rightarrow Zn + W + 4Li_2O \qquad\qquad 5.1$$

$$Zn + Li^+ + e^- \leftrightarrows LiZn \qquad\qquad 5.2$$

$$LiZn + W + 4Li_2O \leftrightarrows Zn + WO_3 + 7Li^+ + 7e^- + Li_2O \qquad\qquad 5.3$$
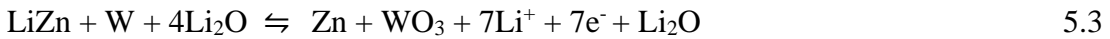
From the Figure 5.4 (c), the peaks at 1.5 V, 0.6 V and 0.2 V correspond to the reduction peaks. The 0.6 V peak is ascribed to the creation of Li$_2$O and reduction of GeO$_2$ to Ge. Below 0.52 V, the formation of the Li$_y$Ge alloy has occurred. The peaks were observed at about 0.6 V, 1.3 V and 2 V in the first oxidation sweep. The peak observed at 0.6 V is attributed to the lithium de-alloying of Li$_y$Ge. The broad peak upto 1.3 V corresponds to the creation of GeO$_2$[304]. The above results show that the ZWGE5, ZWGE10 and ZWGEC nanocomposite exhibit electrochemically reversible lithiation-delithiation. Due to the incorporation of CNT, the integrated area of the ZWGEC nanocomposite is greater to some extent than that of ZWGE5 and ZWGE10, which indicates large capacity during the lithium ion intercalation. Li insertion and extraction in GeO$_2$ are represented [305,304] in the equation (5.4) and (5.5)

$$GeO_x + (3.75+2x)Li^+ + (3.75+2x)e^- \Rightarrow Li_{3.75}\,Ge + xLi_2O \ \ (Charge) \qquad\qquad 5.4$$

$$Li_{3.75}Ge + xLi_2O \Rightarrow Ge + xLi_2O + 3.75Li^+ + 3.75e^- \quad (Discharge) \qquad\qquad 5.5$$
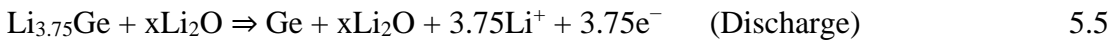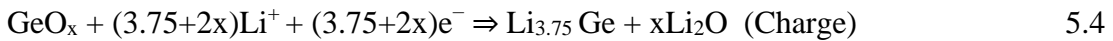
Further, to elucidate the electrochemical property of the ZWGE5, ZWGE10 and ZWGEC nanocomposite, galvanostatic charge/discharge was carried out at the current density of 100 mA g^{-1} and potential window 0.01 – 3 V versus Li/Li$^+$ at room temperature. The first two charge/discharge cycles of the ZWGE5, ZWGE10 and ZWGEC nanocomposite was represented in the Figure 5.5 (a). The obtained first discharge capacity of the ZWGE5, ZWGE10 and ZWGEC nanocomposite was 761, 825 and 930 mAh g^{-1} respectively. It is notable that, the found capacity is higher than the theoretical capacity and can be attributed the formation of the solid electrolyte interface (SEI) layer. Also, the initial charge capacity of the

ZWGE5, ZWGE10 and ZWGEC nanocomposite was 288, 364 and 533 mAh g^{-1} respectively. Note-worthily, ZWGEC nanocomposite exhibits higher charge/discharge capacity than that of ZWGE5 and ZWGE10 composite. The improved capacity may be due to the synergetic effects of the GeO$_2$ and ZnWO$_4$ with incorporation of CNTs. The incorporation of the CNTs into ZWGE10 composite enhances the electronic conductivity of the ZWGEC nanocomposite resulting in the highest specific capacity.

The rate capability is also one of the major indicators of the good performance of the batteries. The rate performance of the ZWGE5, ZWGE10 and ZWGEC nanocomposite is also measured at different current density as shown in the Figure 5.5 (b). At the current rate of 100, 200, 300 and 500 mA g^{-1}, the ZWGEC nanocomposite delivers 598, 411, 318 and 257 mAh g^{-1} discharge capacity and 533, 348, 291 and 231 mAh g^{-1} charge capacity respectively. It is noteworthy that, increase in the current density decreases the specific capacity of the electrodes. After undergoing different current density changes, the ZWGEC nanocomposite is reverted to 458 and 439 mAh g^{-1} discharge and charge capacity respectively at current density of 100 mA g^{-1}, which shows the good reversibility of the ZWGEC nanocomposite.

Further, to check the stability of the ZWGE5, ZWGE10 and ZWGEC nanocomposite, 400 galvanostatic charge/discharge cycles at a current density of 300 mA g^{-1} was carried out and represented in the Figure 5.5 (c). This illustrates poor cycle stability of ZWGEC nanocomposite upto 100 cycles. After 100 cycles ZWGEC nanocomposite shows good capacity retention with 100% columbic efficiency. After a drastic decrease in capacity during initial cycles, the capacity of the cell shows a dramatic increase due to the material properties such as SEI, electrode morphology and confines structure of active materials this can be called as activation of materials. Activation time varies depending on the materials [272]. The ZWGEC nanocomposite shows charge/discharge capacity of 383 and 395 mAh g^{-1} at 300 mA g^{-1} with 96% columbic efficiency.
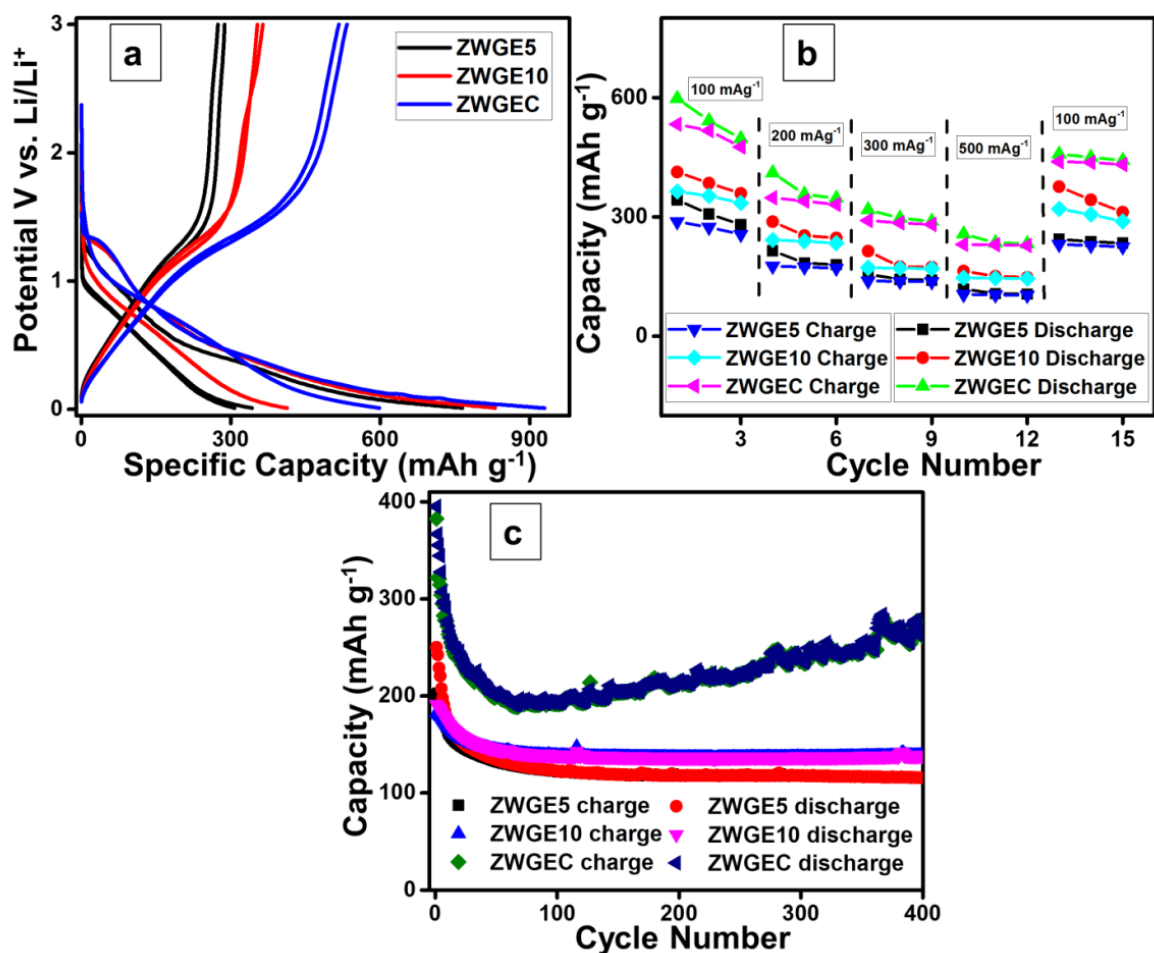
Figure 5.5 (a) Charge discharge curve, (b) Rate capability and (c) Cyclability of the ZWGE5, ZWGE10 and ZWGEC nanocomposite

After 400 cycles, ZWGEC nanocomposite exhibits charge/discharge capacity of 262 and 263 mAh g^{-1} with 100% columbic efficiency. The improved cycle life performance of ZWGEC nanocomposite may be due to the addition of CNT which, increasing the reversibility of the conversion reaction and provided an effective network for electron transfer. And also, it will act as a buffer matrix to reduce the volume expansion during the charge/discharge process [290]. The columbic efficiency and cycle life of the ZWGE5, ZWGE10 and ZWGEC nanocomposite is represented in the Figure 6.

The ZWGEC nanocomposite shows 68.5% capacity retention and 41% cycle life even after 400 cycles. From the Figure 5.6 (a, c), the ZWGE10 exhibits 75.8% capacity retention and 59% cycle life which is higher than ZWGEC nanocomposite. The ZWGEC nanocomposite

exhibits excellent columbic efficiency, high reversible capacity, good capacity retention and decent cycle stability, which suggest the use of ZWGEC nanocomposite as anode material for LIBs.
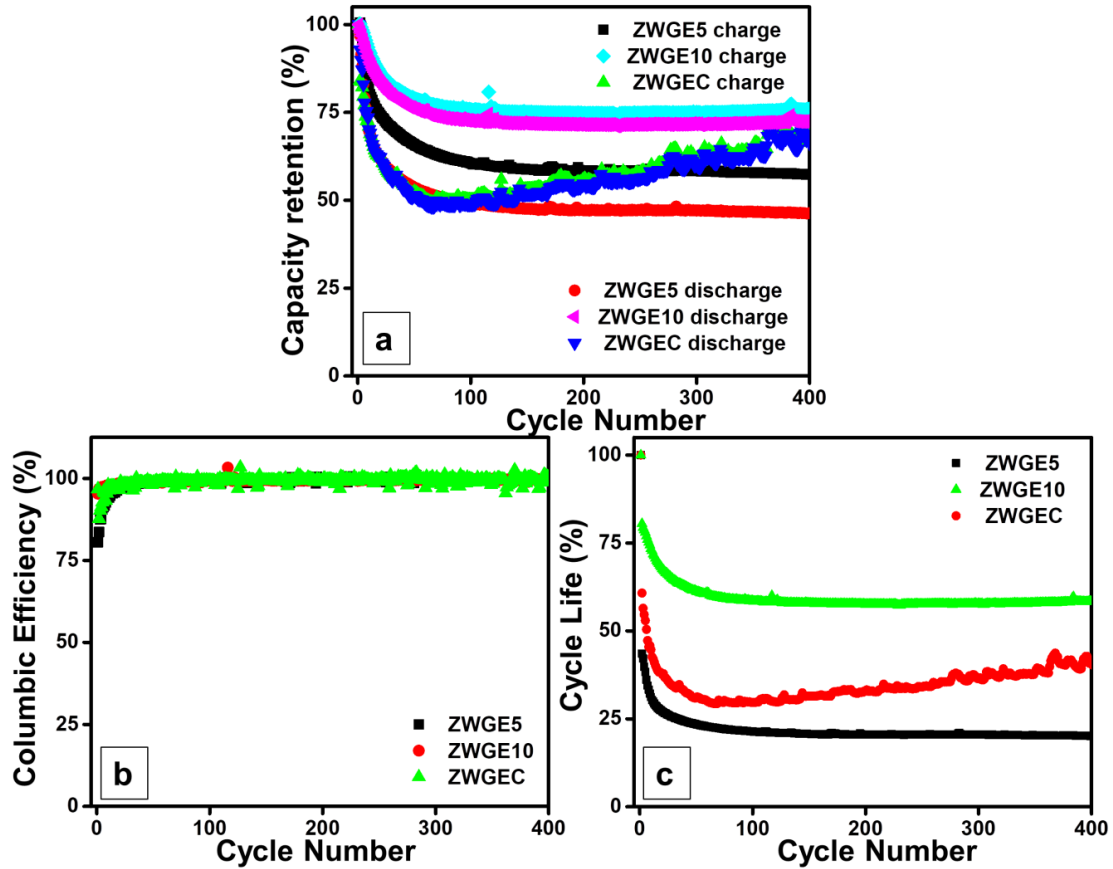
Figure 5.6 (a) Capacity retention versus cycle number (b) Columbic efficiency versus cycle number (c) cycle life versus cycle number plot of ZWGE5, ZWGE10 and ZWGEC nanocomposite

5.4 SUMMARY

➢ $ZnWO_4/GeO_2$ nanocomposite and $ZnWO_4/GeO_2$@CNT nanocomposite have been synthesized by facile solvothermal method

➢ Raman analysis confirms the presence of CNT in the $ZnWO_4/GeO_2$ nanocomposites.

➢ From TGA, approximate amount of carbon content in the ZWGEC nanocomposite is about 4%.

➢ TEM analysis reveals that, ZWGE5, ZWGE10 and ZWGEC nanocomposite form as a nanorods. And also suggests that, ZWGE10 nanocomposites are grown around the CNT.

➢ The prepared $ZnWO_4/GeO_2$ nanocomposites and $ZnWO_4/GeO_2$@CNT nanocomposite are used as anode material for lithium-ion battery (LIB).

➢ The $ZnWO_4/GeO_2$@CNT nanocomposite represents 533 mAh g^{-1} and 930 mAh g^{-1} charge/discharge capacity which is higher than that of $ZnWO_4/GeO_2$ nanocomposite.

➢ The synergetic effect of GeO_2 and $ZnWO_4$ increases the capacity of the $ZnWO_4/GeO_2$ nanocomposite. Further, addition of CNTs into $ZnWO_4/GeO_2$ nanocomposite boosts the electrochemical activity, rate capability and specific capacity of the $ZnWO_4/GeO_2$@CNT nanocomposite.

➢ $ZnWO_4/GeO_2$@CNT nanocomposite is a promising anode material for lithium ion battery.

CHAPTER 6

ZnWO$_4$/SiO$_2$ NANOCOMPOSITE

FOR ELECTROCHEMICAL ENERGY STORAGE

CHAPTER 6

ZnWO$_4$/SiO$_2$ NANOCOMPOSITE FOR ELECTROCHEMICAL ENERGY STORAGE

In this chapter contains the preparation and characterization of ZnWO$_4$/SiO$_2$ nanocomposite with varying the percentage of SiO$_2$ via microwave assisted method. The structural and morphological characterization of ZnWO$_4$/SiO$_2$ nanocomposite was done using x-ray diffraction measurements (XRD), field emission scanning electron microscopy (FESEM) and energy-dispersive X-ray spectroscopy (EDAX). Further, ZnWO$_4$/SiO$_2$ nanocomposite was used as anode material for LIB and electrochemical characterization done using cyclic voltammetry (CV), galvanostatic charge-discharge (GCD) and electrochemical impedance spectroscopy techniques.

6.1 INTRODUCTION

Lithium ion battery (LIB) is one of the promising energy storage devices to resolve the scarcity of the energy storage. Graphite and graphitized carbon materials are currently used as commercialized anode material with a theoretical capacity of 372 mAh g^{-1}[179]. Fabricating new negative electrode with high capacity, long cycle life and high energy density is necessary and urgently required. Nowadays, metal oxide compounds[261] and silicon-based compounds have gained more attention in the recent years due to low cost, availability, good capacity and cycle stability.

Recently, zinc tungstates are attractive anode material for LIBs because of their good theoretical capacity (684 mAh g^{-1}), high conductivity and high specific area. The composites of ZnWO$_4$ with other materials are also investigated. Nowadays, silicon oxide has also drawn more attention as anode for LIBs due to its high theoretical capacity (1961 mAh g^{-1}), low discharge potential and abundance. Furthermore, ZnWO$_4$ and SiO$_2$ also have some drawbacks like; an initial charge/discharge cycle shows low columbic efficiency, poor conductivity and poor rate capability. To overcome above problems, researchers focused on hybrid metal oxides. Li-Li Xing and coworkers[133] prepared SnO$_2$/ZnWO$_4$ nanorods via two step hydrothermal method. They reported that the discharge capacity of SnO$_2$/ZnWO$_4$ nanorod is 1318 mA h g^{-1}

which is higher than that of bare $ZnWO_4$ (1008 mA h g^{-1}) and SnO_2 (782 mAh g^{-1}). Herein, we synthesized $ZnWO_4/SiO_2$ nanocomposite via facile microwave irradiation method. The prepared $ZnWO_4/SiO_2$ nanocomposite is used as an anode material for LIB and compared with bare $ZnWO_4$.

6.2 SYNTHESIS AND CHARACTERIZATION

6.2.1 Experimental

Zinc chloride ($ZnCl_2$) dry (EMPLURA®, Merck Specialities Pvt. Ltd.), ammonium tungsten oxide (($NH_4)_2WO_4$, 99.99% (Metal basis)) (Alfa Aesar Co. Ltd.), silicon dioxide nanopowder (EMPLURA®, Merck Specialities Pvt. Ltd.), ethylene glycol ($C_2H_6O_2$, 99%) (Loba Chemie Pvt. Ltd.) and double distilled water were used as solvents. The above chemicals were all used for the preparation of the material without any further purification.

6.2.2 Preparation of $ZnWO_4$

To prepare zinc tungstate, zinc chloride and ammonium tungsten oxide were added separately in amounts of 325 mg and 301.2 mg respectively with 50 ml (1:1 v/v) of ethylene glycol and distilled water and the solutions were then stirred for 15 minutes. The two solutions were later mixed slowly with constant stirring and again stirred for another 30 minutes. The resultant solution was later irradiated with 300 W microwave radiations for 10 min. The solution was then allowed to cool naturally and then the precipitate was washed several times with distilled water, ethanol and acetone to remove by-products and left to dry in an oven at 65℃ for 24 hours. The dried precipitate is then transferred into a furnace, where the precipitate is annealed at 500℃ for 1 hour and the sample was named as ZW.

6.2.3 Preparation of $ZnWO_4/SiO_2$ nanocomposite

Preparation of the $ZnWO_4$ was represented in the supplementary. To prepare $ZnWO_4/SiO_2$ nanocomposite, preparation procedure of $ZnWO_4$ was repeated with the addition of silicon dioxide nanopowder with molar ratio of 1:0.01, 1:0.02, 1:0.03, 1:0.04 and 1:0.05 and the samples are named as ZWSO1, ZWSO2, ZWSO3, ZWSO4 and ZWSO5 respectively.

6.3 RESULTS AND DISCUSSION

6.3.1 Structural and morphological characterization
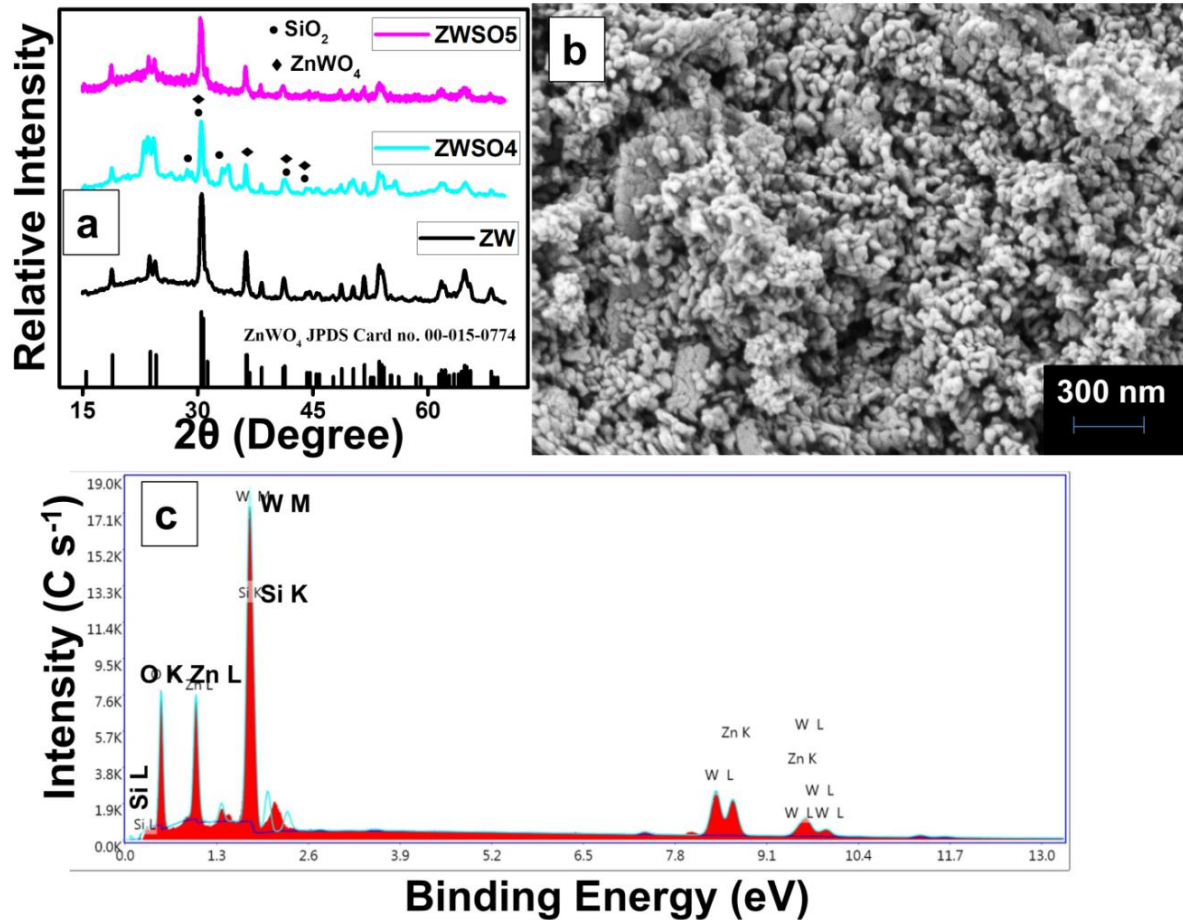
Fig. 6.1(a) XRD peaks of ZW, ZWSO4 and ZWSO5 nanocomposite (b) FESEM image and (c) EDAX map of ZWSO5.

Figure 6.1(a) represents the powder x-ray diffraction pattern of the ZW, ZWSO4 and ZWSO5 nanocomposite. In addition, diffraction pattern of ZWSO1, ZWSO2 and ZWSO3 is represented in the Figure 6.2. The diffraction pattern of the ZW has monoclinic Wolframite structure and matches with the JCPDS Card No.00-015-0774. As seen in the Figure 6.1(a) and Figure 6.2, the diffraction pattern of the ZWSO1, ZWSO2, ZWSO3, ZWSO4 and ZWSO5 nanocomposite also have the monoclinic Wolframite structure with additional peaks of SiO_2 at

2θ values of 28.62°, 30.44°, 33.2°, 41.2° and 44.1° which confirms the formation of $ZnWO_4/SiO_2$ composite without any effect on monoclinic Wolframite structure of the $ZnWO_4$..
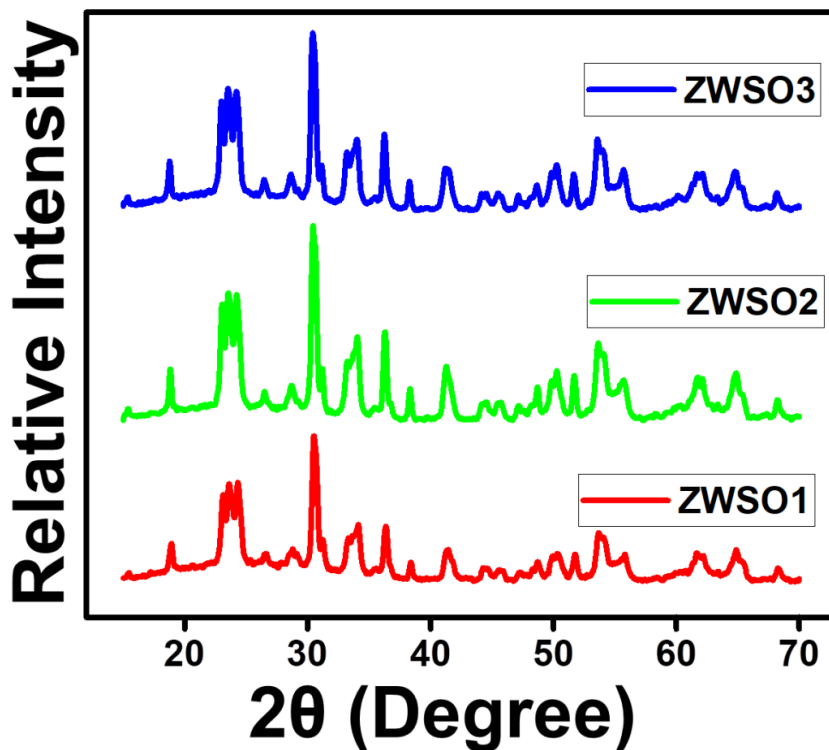
Figure 6.2 Powder X-ray diffraction patterns of the ZWSO1, ZWSO2 and ZWSO3 at a scan rate of 2°/min in the 2θ range 15–70°.

Figure 6.1(b) and 1(c) represents the FESEM image and EDAX map of the ZWSO5 nanocomposite. The FESEM image of the ZWSO5 nanocomposite shows the agglomerated nanorods of length 110 – 150 nm and width 25 – 38 nm. Further, there is no much difference in FESEM images of the ZW, ZWSO1, ZWSO2, ZWSO3 and ZWSO4 composites as represented in the Figure 6.3. The EDAX analysis of the ZWSO5 nanocomposite represents the presence of zinc (Zn), tungsten (W), oxygen (O) and silicon (Si) content in the atomic percentage of 11.62, 14.14, 69.39 and 4.86 respectively. The elements present in the ZW, ZWSO1, ZWSO2, ZWSO3 and ZWSO4 composites and atomic percentage of the same are represented in the Table 6.1.
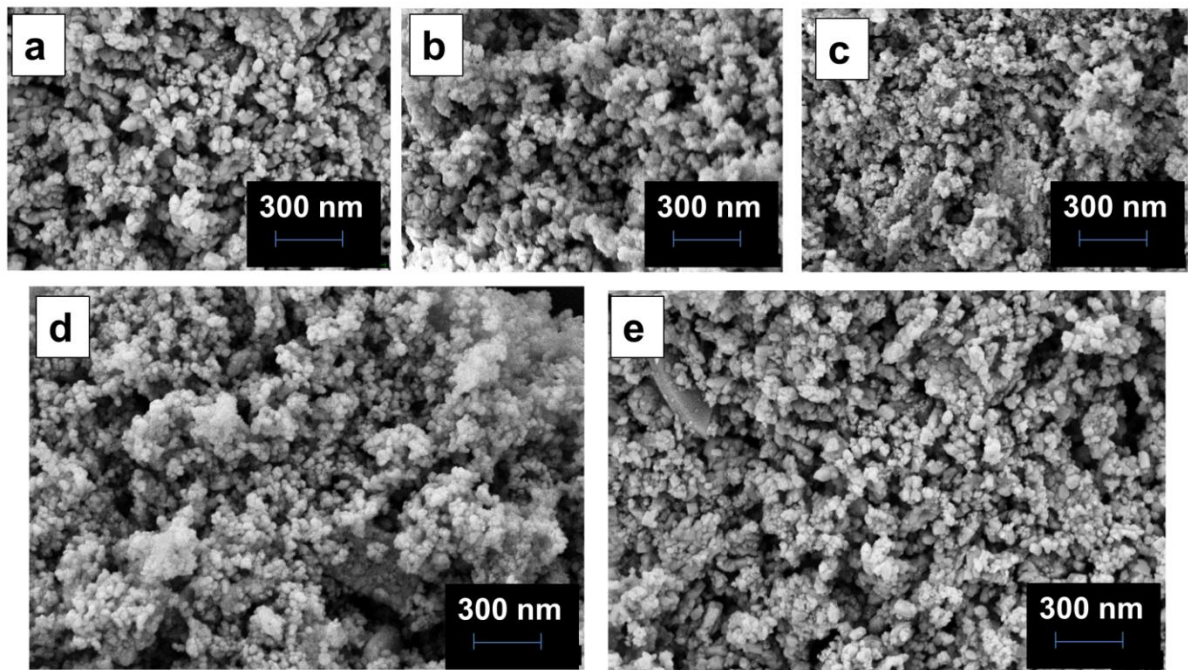
Figure 6.3 FESEM images of the ZW, ZWSO1, ZWSO2, ZWSO3 and ZWSO4 composites

Table 6.1 the atomic percentage of the elements observed in the EDAX analysis

Sample	Elements	Atomic %	Sample	Elements	Atomic %
ZW	Zn	11.79	ZWSO3	Zn	9.55
	W	12.56		W	15.41
	O	75.66		O	71.76
ZWSO1	Zn	10.05		Si	3.28
	W	12.56	ZWSO4	Zn	11.02
	O	75.66		W	17.10
	Si	1.74		O	67.47
ZWSO2	Zn	12.13		Si	4.41
	W	13.33	ZWSO5	Zn	11.62
				W	14.14

	O	71.97			O	69.39
	Si	2.56			Si	4.86

6.3.2 Electrochemical Analysis

To elucidate the assessment of electrochemical reaction during discharge and charge, CV measurements were performed and represented in the Figure 6.4(a). There are two prominent reduction peaks at 0.6 V and 1.1 V, which can be ascribed to the reduction of $ZnWO_4$ to W and Zn. The other minor peaks below 0.17 V were due to the creation of solid electrolyte interface (SEI) on the surface of the electrode and also due to formation of Li-Zn alloy [139]. The reduction peak at 0.24 V is ascribed to lithiation of SiO while the oxidation peak at 0.5 and 0.4 V are ascribed to delithiation of Si [306]. The oxidation peaks between 0.4 and 0.6 V are attributed to the de-alloying reaction of Zn-Li. The delithiation process indicated by a peak from 0.8 to 2 V corresponds to the oxidation of ZnO and WO_3 to Zn^{2+} and W^{6+} respectively[136]. Peak positions are determined by scan rate; cathodic peaks are shifted to lower values and anodic peaks are shifted to higher values with increasing scan rate. The ZWSO5 shows larger integrated area than ZW, ZWSO1, ZWSO2, ZWSO3 and ZWSO4 which is due to the incorporation SiO_2 into $ZnWO_4$ nanoparticles. Based on the above analysis, the discharge and charge reactions of $ZnWO_4$ and SiO electrodes can be shown as below [307,261]

$$ZnWO_4 + 8Li^+ + 8e^- \rightarrow Zn + W + 4Li_2O \qquad (6.1)$$

$$Zn + Li^+ + e^- \rightarrow LiZn \qquad (6.2)$$

$$LiZn + W + 3LiO_2 \rightarrow Zn + WO_3 + 6Li^+ + 6e^- \qquad (6.3)$$

$$SiO_x + yLi + ye \rightarrow Si + Li_yO_x \qquad (6.4)$$

$$yLi + SiO_x \rightarrow Li_ySiO_x \qquad (6.5)$$

$$Li + Si + xe \leftrightarrow Li_xSi \qquad (6.6)$$
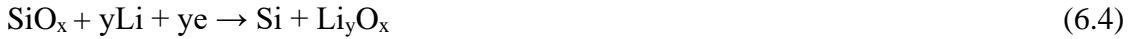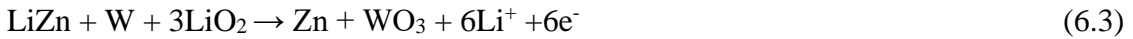
To study the electrochemical property of the prepared samples, Galvanostatic charge/discharge test was carried out. Figure 6.4(b) shows the first two charge/discharge cycles of the prepared ZW, ZWSO1, ZWSO2, ZWSO3, ZWSO4 and ZWSO5 nanocomposites at 10 mA g^{-1}. The ZWSO5 nanocomposite shows 570 mAh g^{-1}, initial discharge capacity and 314 mAh g^{-1} charge capacity with a columbic efficiency of 114%, which is better than that of ZW (145 and 130 mAh g^{-1}, columbic efficiency of 89.65%), ZWSO1(265 and 246 mAh g^{-1}, columbic efficiency of 92.8%) , ZWSO2 (278 and 253 mAh g^{-1}, columbic efficiency of 91%), ZWSO3 (363 and 285 mAh g^{-1}, columbic efficiency of 78.5%) and ZWSO4 (453 and 294 mAh g^{-1}, columbic efficiency of 64.9%) respectively. The initial charge/discharge capacities of the ZW, ZWSO1, ZWSO2, ZWSO3, ZWSO4 and ZWSO5 nanocomposite are tabulated in the Table 6.2. The synergetic effect between ZnWO$_4$ and SiO$_2$ increase the specific capacity of the ZWSO5 nanocomposite. The increasing percentage of SiO$_2$ in the composite increases the capacity.

Table 6.2 first cycle charge/discharge capacity of the prepared ZW, ZWSO1, ZWSO2, ZWSO3, ZWSO4 and ZWSO5 nanocomposite

Sl No	Samples	Discharge Capacity mAh/g	Charge Capacity mAh/g
1	ZW	145	130
2	ZW01	265	246
3	ZW02	278	253
4	ZW03	363	285
5	ZW04	453	294
6	ZW05	570	314
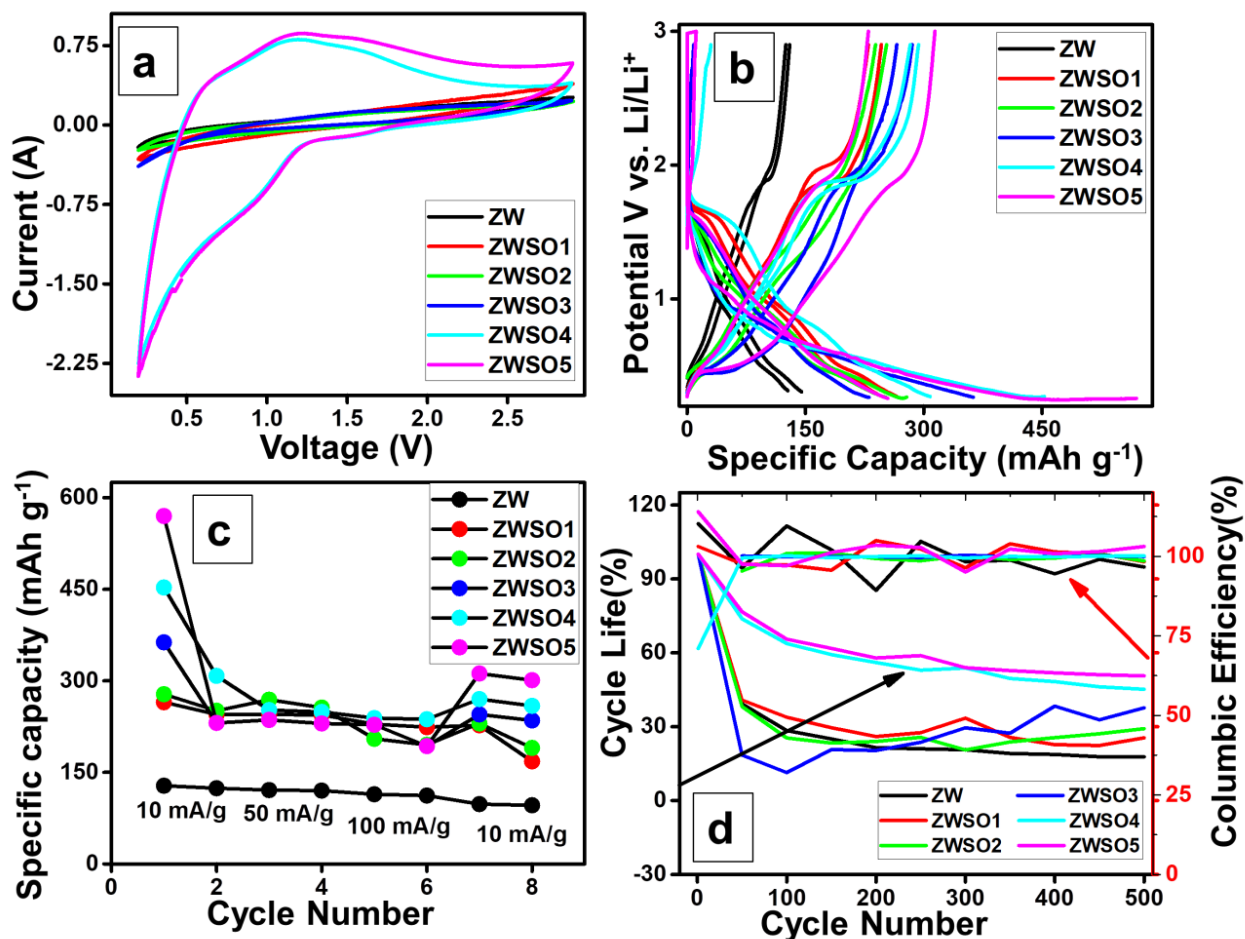
Figure 6.4 (a) cyclic voltammetry, (b) charge/discharge curve (c) rate capability and (d) cyclability of the ZW, ZWSO1, ZWSO2, ZWSO3, ZWSO4 and ZWSO5 nanocomposite

As expected, ZWSO5 nanocomposite shows a good rate performance as represented in the Figure 6.4(c). It delivers a discharge capacity of about 254, 239 and 200 mAh g^{-1} at a current density of 10, 50 and 100 mA g^{-1} respectively. Furthermore, after the high rate measurements, the specific capacity of the ZWSO5 nanocomposite is 227 mAh g^{-1} at 10 mA g^{-1} which shows good reversibility of the electrode. The prepared ZW, ZWSO1, ZWSO2, ZWSO3, ZWSO4 and ZWSO5 nanocomposite samples are able to pick up nearly their primary values, thereby indicating their reversibility.

To study the stability of the as prepared samples, the electrodes were cycled galvanostatically at a current density of 100 mA g^{-1} at room temperature and the results are represented in the

104

Figure 6.4(d). The ZWSO5 nanocomposite shows 51% cycle life even after 500 cycles which is comparably higher than the ZW (18%), ZWSO1 (25%), ZWSO2 (29%), ZWSO3 (38%) and ZWSO4 (45%). The first cycle columbic efficiency of the ZWSO5 nanocomposite is 114% and over 500 cycles the columbic efficiency is 103%. The SiO_2 has superior mechanical stability and good conductivity in nanoscale range[307]. SiO_2 has the advantage of storing large amount of lithium and low discharge potentials[308]. The stability and rate capability of the composite can increase with the addition of SiO_2 to $ZnWO_4$.

To find out the electrode kinetics of the material, EIS was performed and demonstrated in Figure 6.5(a). Nyquist curves comprise of two compact semicircles and a tilted line, the former in the higher-frequency region and later in the lower-frequency region [193,195]. Reaction resistance (R1) and capacity reactance (C1) of the freshly formed SEI layer constitutes the first semicircle, while transfer resistance (R2) and double layer capacity reactance (C2) account for the second semicircle. The tilted line represents impedance to ion diffusion described by Warburg impedance (Rw)[212]. Likewise, bulk resistance (R3) of the battery system is represented by an intercept on horizontal axis in higher frequency region. Further, fitting of Nyquist plots by an equivalent circuit is done as shown in Figure 6.5(b) to get an intuition of the mechanism involved. The fitting results are recorded in Table 6.3.
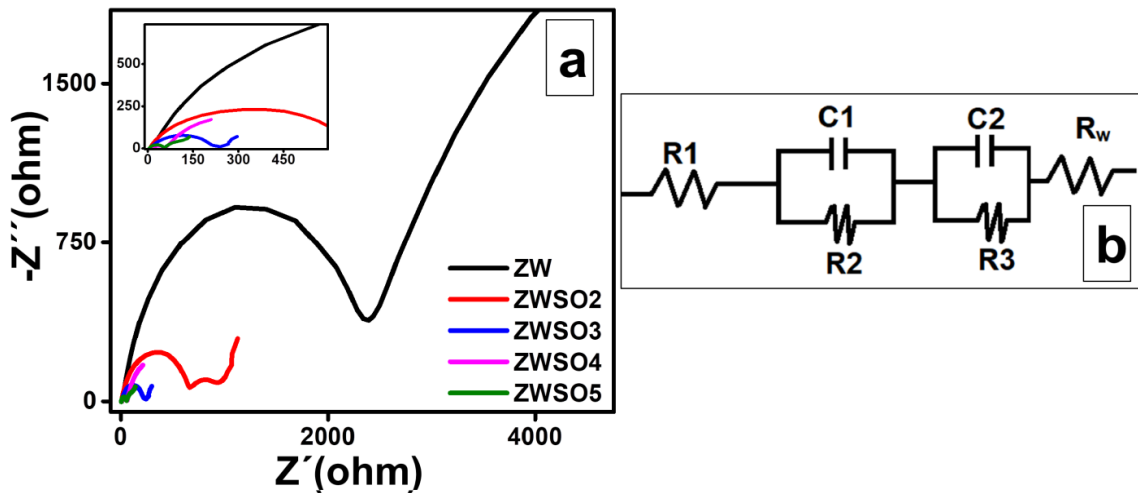
Figure 6.5 (a) Electrochemical impedance spectroscopy curves and (b) equivalent circuit of the ZW, ZWSO2, ZWSO3, ZWSO4 and ZWSO5 nanocomposite

The R_1 value of the ZWSO5 nanocomposite electrode is 4.307 Ω which is lower than the values of ZW, ZWSO2, ZWSO3 and ZWSO4 which are 19.53 Ω, 9.257 Ω, 6.252 Ω and 5.181 Ω respectively, representing that the incorporation of SiO_2 into $ZnWO_4$ decreases the reaction resistance of SEI layer. Furthermore, from the Table T3 R_2 value decreases with the synergetic effect of the incorporation of SiO_2 and $ZnWO_4$ nanoparticles. Likewise, we can observe the decrease in the R_w value with the increasing concentration of SiO_2 nanoparticles in the $ZnWO_4$ nanocomposite.

Table 6.3 Nyquist plot fitted values of ZW, ZWSO2, ZWSO3, ZWSO4 and ZWSO5 nanocomposite

Samples	R_1 (Ω)	C_1 (μF)	R_2 (Ω)	C_2 (μF)	R_3(Ω)	R_W (Ω s$^{-1/2}$)
ZW	19.53	0.5453	517	0.2839	1814	1187
ZWSO2	9.257	1.997	196.1	0.7893	621.8	72.04
ZWSO3	6.252	5.428	172.8	1.933	38.56	15.94
ZWSO4	5.181	3.236	132.2	7.499	17.59	13.2
ZWSO5	4.307	26.37	45.77	11.24	1.962	10.17

6.4 SUMMARY

➢ Monoclinic Wolframite $ZnWO_4$ and $ZnWO_4/SiO_2$ nanocomposite are successfully prepared via microwave method.

➢ The $ZnWO_4/SiO_2$ nanocomposite was prepared by increasing percentage of SiO_2.

➢ The SEM analysis confirms the agglomerated nanorods of length 110 – 150 nm and width 25 – 38 nm.

➢ The $ZnWO_4/SiO_2$ nanocomposite used as anode material for LIB and studied the electrochemical property comparing the composites.

➢ The increasing percentage of SiO_2 in the $ZnWO_4/SiO_2$ nanocomposite enhances the electrochemical property such as high specific capacity, high initial columbic efficiency and long stable life.

➢ Synergetic effect between $ZnWO_4$ and SiO_2 also boosts the electrochemical property of the $ZnWO_4/SiO_2$ nanocomposite.

➢ $ZnWO_4/SiO_2$ nanocomposite is good anode for LIB.

CHAPTER 7

CONCLUSION AND FUTURE DIRECTIONS

CHAPTER 7

Conclusion and Future Directions

7.1 Conclusion

In this thesis work, solvothermal method was used for the preparation of pristine ($ZnWO_4$) and hybrid metal oxides ($SnO_2/ZnWO_4$ nanocomposite, $GeO_2/ZnWO_4$ nanocomposite and $ZnWO_4/SiO_2$ nanocomposite) along with their carbon based composite ($ZnWO_4@r-GO$ nanocomposite, $ZnWO_4/SnO_2@r-GO$ nanocomposite and $GeO_2/ZnWO_4@CNT$ nanocomposite) and microwave assisted method was used to prepare pristine $ZnWO_4$ and $ZnWO_4/SiO_2$ nanocomposite. Synthesized pristine and hybrid metal oxides are used as an anode material for LIBs. The detailed structural, elemental, morphological and electrochemical studies have undergone and compared. The summary of the study is as follows,

- ➢ The structural, elemental and morphological properties of the prepared samples were characterized using XRD, FESEM, EDAX, HRTEM and XPS.
- ➢ FESEM and HRTEM reveal nanostructure for all samples.
- ➢ XPS results confirm the elemental composition of the prepared composite.
- ➢ The electrochemical properties of the prepared samples were analyzed using CV, GCD and EIS.
- ➢ Electrochemical results infer that, $ZnWO_4@r-GO$ nanocomposite delivers discharge capacity of 1158 mAh g^{-1} at 100 mA g^{-1}, with 80.74% capacity retention and $ZnWO_4/SnO_2@r-GO$ nanocomposite provides discharge capacity of 1486 mAh g^{-1} at 100 mA g^{-1}, with 98% capacity retention and 89.08 % cycle life. Also, $GeO_2/ZnWO_4@CNT$ nanocomposite delivers discharge capacity of 930 mAh g^{-1} at 100 mA g^{-1}, with a 75.8% capacity retention and 41% cycle life and $ZnWO_4/SiO_2$ nanocomposite shows discharge capacity of 570 mAh g^{-1} at 10 mA g^{-1} and 51 % cycle life.
- ➢ In $ZnWO_4/SnO_2@r-GO$ nanocomposite, the synergetic effect of SnO_2 and $ZnWO_4$ increases the discharge capacity of the composite. The addition of GO into the composite enhances the surface area, pore volume and electrochemical activity,

resulting in high charge/discharge capacity, decent cycling stability and good rate capability

➤ From the electrochemical analysis, $ZnWO_4/SnO_2@r$-GO nanocomposite shows higher initial capacity, long cycle stability and good rate capability compared with other prepared composites.

Table 7.1 Overall results of the prepared composites

Sample	Preparation method	Morpho logy	Initial discharge capacity (mAh g^{-1})	Initial charge capacity (mAh g^{-1})	Current density (mA g^{-1})	Capacity retention (%)
$ZnWO_4$	Solvothermal	nanorods	746	295	100	48.35
$ZnWO_4@r$-GO nanocomposite	Solvothermal	nanorods	1158	552	100	80.74
ZWSN-5 nanocomposite	Solvothermal	nanorods	882	367	100	62.82
ZWSN-10 nanocomposite	Solvothermal	nanorods	1316	425	100	51.78
$ZnWO_4/SnO_2@$ r-GO nanocomposite	Solvothermal	nanorods	1486	548	100	98
ZWGE5 nanocomposite	Solvothermal	nanorods	761	288	100	46.27
ZWGE10 nanocomposite	Solvothermal	nanorods	825	364	100	75.8
$ZnWO_4/$ $GeO_2@CNT$ nanocomposite	Solvothermal	nanorods	930	533	100	68.5
$ZnWO_4/SiO_2$ nanocomposite	Microwave method	nanorods	570	314	10	51

7.2 FUTURE DIRECTIONS

To extend the present work further, following directions may be considered:

➢ Hybrid metal oxides with different transition metal oxides may be prepared.

➢ The anodic performance of the LIB can be improved by the addition of different carbonaceous materials like carbon nanostructures, conducting polymers and activated carbons. Further to find out the electrochemical reactions, in-situ XRD and XPS could be carried out.

➢ Full cell may be fabricated using commercialized cathode and electrolyte materials to estimate the actual capacity and the overall performance of the battery.

APPENDIX

REFERENCES

1. Anderson TR, Hawkins E, Jones PD (2016) CO2, the greenhouse effect and global warming: from the pioneering work of Arrhenius and Callendar to today's Earth System Models. Endeavour 40 (3):178-187. doi:https://doi.org/10.1016/j.endeavour.2016.07.002

2. Ekwurzel B, Boneham J, Dalton MW, Heede R, Mera RJ, Allen MR, Frumhoff PC (2017) The rise in global atmospheric CO2, surface temperature, and sea level from emissions traced to major carbon producers. Climatic Change 144 (4):579-590. doi:10.1007/s10584-017-1978-0

3. Solomon S, Plattner G-K, Knutti R, Friedlingstein P (2009) Irreversible climate change due to carbon dioxide emissions. Proceedings of the National Academy of Sciences 106 (6):1704-1709. doi:10.1073/pnas.0812721106

4. Keeling CD (1997) Climate change and carbon dioxide: an introduction. Proc Natl Acad Sci U S A 94 (16):8273-8274. doi:10.1073/pnas.94.16.8273

5. Liu J, Wang J, Xu C, Jiang H, Li C, Zhang L, Lin J, Shen ZX (2018) Advanced Energy Storage Devices: Basic Principles, Analytical Methods, and Rational Materials Design. Advanced Science 5 (1):1700322. doi:https://doi.org/10.1002/advs.201700322

6. Dincer I, Acar C (2015) Review and evaluation of hydrogen production methods for better sustainability. International Journal of Hydrogen Energy 40 (34):11094-11111. doi:https://doi.org/10.1016/j.ijhydene.2014.12.035

7. Owusu PA, Asumadu-Sarkodie S (2016) A review of renewable energy sources, sustainability issues and climate change mitigation. Cogent Engineering 3 (1):1167990. doi:10.1080/23311916.2016.1167990

8. Dorning MA, Diffendorfer JE, Loss SR, Bagstad KJ (2019) Review of indicators for comparing environmental effects across energy sources. Environmental Research Letters 14 (10):103002. doi:10.1088/1748-9326/ab402d

9. Milledge JJ, Heaven S (2014) Methods of energy extraction from microalgal biomass: a review. Reviews in Environmental Science and Bio/Technology 13 (3):301-320. doi:10.1007/s11157-014-9339-1

10. Elliott D (2017) Energy Storage Systems. doi:10.1088/978-0-7503-1531-9

11. Introduction: Energy Storage Technologies. In: Handbook of Clean Energy Systems. pp 1-3. doi:https://doi.org/10.1002/9781118991978.hces169

12. Olabi AG, Onumaegbu C, Wilberforce T, Ramadan M, Abdelkareem MA, Al – Alami AH (2021) Critical review of energy storage systems. Energy 214:118987. doi:https://doi.org/10.1016/j.energy.2020.118987

13. Kampouris KP, Drosou V, Karytsas C, Karagiorgas M (2020) Energy storage systems review and case study in the residential sector. IOP Conference Series: Earth and Environmental Science 410:012033. doi:10.1088/1755-1315/410/1/012033

14. Bank AD (2018) Handbook on Battery Energy Storage System. Asian Development Bank,

15. Xin S. GH, Li Y., Guo YG (2019) Introduction to Electrochemical Energy Storage. Springer, Singapore

16. Scott K (2020) Chapter 1 Introduction to Electrolysis, Electrolysers and Hydrogen Production. In: Electrochemical Methods for Hydrogen Production. The Royal Society of Chemistry, pp 1-27. doi:10.1039/9781788016049-00001

17. Vladimir S. Bagotsky AMS, Yurij M. Volfkovich (2015) Electrochemical Power Sources: Batteries, Fuel Cells, and Supercapacitors. Wiley,

18. Buckley DN, O'Dwyer C, Quill N, Lynch RP (2019) Electrochemical Energy Storage. In: Energy Storage Options and Their Environmental Impact. The Royal Society of Chemistry, pp 115-149. doi:10.1039/9781788015530-00115

19. Abood N (2020) Chapter 1. Introduction of Electrochemical Chapter 1. Introduction of Electrochemical Concepts Concepts. In.

20. Wang P, Wang J, Fu L, Wu Y, van Ree T (2018) 2 - Metal oxides in fuel cells. In: Wu Y (ed) Metal Oxides in Energy Technologies. Elsevier, pp 17-47. doi:https://doi.org/10.1016/B978-0-12-811167-3.00002-X

21. Cook B (2002) Introduction to fuel cells and hydrogen technology. Engineering Science and Education Journal 11 (6):205-216. doi:10.1049/esej:20020601

22. Shah R (2007) Introduction to Fuel Cells. In. pp 1-9. doi:10.1007/978-0-387-68815-2_1

23. Saxena S, Verma A (2015) INTRODUCTION TO FUEL CELL TECHNOLOGY : A REVIEW. doi:10.17148/IARJSETT

24. Sharaf OZ, Orhan MF (2014) An overview of fuel cell technology: Fundamentals and applications. Renewable and Sustainable Energy Reviews 32:810-853. doi:https://doi.org/10.1016/j.rser.2014.01.012

25. Kirubakaran A, Jain S, Nema RK (2009) A review on fuel cell technologies and power electronic interface. Renewable and Sustainable Energy Reviews 13 (9):2430-2440. doi:https://doi.org/10.1016/j.rser.2009.04.004

26. Carrette L, Friedrich KA, Stimming U (2001) Fuel Cells – Fundamentals and Applications. Fuel Cells 1 (1):5-39. doi:https://doi.org/10.1002/1615-6854(200105)1:1<5::AID-FUCE5>3.0.CO;2-G

27. Mohapatra A, Tripathy S (2018) A Critical Review of the use of Fuel Cells Towards Sustainable Management of Resources. IOP Conference Series: Materials Science and Engineering 377:012135. doi:10.1088/1757-899x/377/1/012135

28. Sun H, Zhu J, Baumann D, Peng L, Xu Y, Shakir I, Huang Y, Duan X (2019) Hierarchical 3D electrodes for electrochemical energy storage. Nature Reviews Materials 4 (1):45-60. doi:10.1038/s41578-018-0069-9

29. Sinha P. KKK (2020) Introduction to Supercapacitors, vol 302. Springer Series in Materials Science.

30. Scibioh MA, Viswanathan B (2020) Chapter 1 - Supercapacitor: an introduction. In: Scibioh MA, Viswanathan B (eds) Materials for Supercapacitor Applications. Elsevier, pp 1-13. doi:https://doi.org/10.1016/B978-0-12-819858-2.00001-9

31. Max Lu FB, Elzbieta Frackowiak (2013) Supercapacitors: Materials, Systems, and Applications. Wiley,

32. Khanna VK (2019) Supercapacitors. Flexible Electronics, Volume 3. IOP Publishing. doi:10.1088/2053-2563/ab0d19ch1

33. Scibioh MA, Viswanathan B (2020) Chapter 2 - Fundamentals and energy storage mechanisms—overview. In: Scibioh MA, Viswanathan B (eds) Materials for Supercapacitor Applications. Elsevier, pp 15-33. doi:https://doi.org/10.1016/B978-0-12-819858-2.00002-0

34. Moftah A (2019) Review of Supercapacitor Technology.

35. Huang S, Zhu X, Sarkar S, Zhao Y (2019) Challenges and opportunities for supercapacitors. APL Materials 7 (10):100901. doi:10.1063/1.5116146

36. Wang S, Wei T, Qi Z (2008) Supercapacitor Energy Storage Technology and its Application in Renewable Energy Power Generation System. In. pp 2805-2809. doi:10.1007/978-3-540-75997-3_566

37. Prasad G, Shetty N, Thakur S, Rakshitha, K B B (2019) Supercapacitor technology and its applications: a review. IOP Conference Series: Materials Science and Engineering 561:012105. doi:10.1088/1757-899X/561/1/012105

38. Vincent CA (1997) 1 - Introduction. In: Vincent CA, Scrosati B (eds) Modern Batteries (Second Edition). Butterworth-Heinemann, Oxford, pp 1-17. doi:https://doi.org/10.1016/B978-034066278-6/50002-4

39. Colin Angus Vincent BS (1997) Modern Batteries: An Introduction to Electrochemical Power Sources. 2 edn. E. Arnold, 1997,

40. Primary batteries (2001). In: Dell RM, Rand DAJ (eds) Understanding Batteries. The Royal Society of Chemistry, pp 52-52. doi:10.1039/9781847552228-00052

41. Kordesch K, Taucher-Mautner W (2009) HISTORY | Primary Batteries. In: Garche J (ed) Encyclopedia of Electrochemical Power Sources. Elsevier, Amsterdam, pp 555-564. doi:https://doi.org/10.1016/B978-044452745-5.00003-4

42. Rechargeable batteries (2001). In: Dell RM, Rand DAJ (eds) Understanding Batteries. The Royal Society of Chemistry, pp 97-99. doi:10.1039/9781847552228-00097

43. Advanced rechargeable batteries and capacitors (2001). In: Dell RM, Rand DAJ (eds) Understanding Batteries. The Royal Society of Chemistry, pp 163-187. doi:10.1039/9781847552228-00163

44. Lithium batteries (2001). In: Dell RM, Rand DAJ (eds) Understanding Batteries. The Royal Society of Chemistry, pp 143-162. doi:10.1039/9781847552228-00143

45. How a battery operates (2001). In: Dell RM, Rand DAJ (eds) Understanding Batteries. The Royal Society of Chemistry, pp 10-21. doi:10.1039/9781847552228-00010

46. Yoshizawa H (2009) SECONDARY BATTERIES – LITHIUM RECHARGEABLE SYSTEMS – LITHIUM-ION | Lithium Vanadium Oxide/Niobium Oxide Batteries. In: Garche J (ed) Encyclopedia of Electrochemical Power Sources. Elsevier, Amsterdam, pp 368-374. doi:https://doi.org/10.1016/B978-044452745-5.00220-3

47. Virtanen S (2009) ELECTROCHEMICAL THEORY | Corrosion. In: Garche J (ed) Encyclopedia of Electrochemical Power Sources. Elsevier, Amsterdam, pp 56-63. doi:https://doi.org/10.1016/B978-044452745-5.00026-5

48. Quartarone E, Mustarelli P (2020) Review—Emerging Trends in the Design of Electrolytes for Lithium and Post-Lithium Batteries. Journal of The Electrochemical Society 167 (5):050508. doi:10.1149/1945-7111/ab63c4

49. Li Q, Chen J, Fan L, Kong X, Lu Y (2016) Progress in electrolytes for rechargeable Li-based batteries and beyond. Green Energy & Environment 1 (1):18-42. doi:https://doi.org/10.1016/j.gee.2016.04.006

50. Francis CFJ, Kyratzis IL, Best AS (2020) Lithium-Ion Battery Separators for Ionic-Liquid Electrolytes: A Review. Advanced Materials 32 (18):1904205. doi:https://doi.org/10.1002/adma.201904205

51. Arora P, Zhang Z (2004) Battery Separators. Chemical Reviews 104 (10):4419-4462. doi:10.1021/cr020738u

52. Writer B (2019) Ionic Conductivity, Polymer Electrolyte, Membranes, Electrochemical Stability, Separators. In: Lithium-Ion Batteries: A Machine-Generated Summary of Current Research. Springer International Publishing, Cham, pp 163-193. doi:10.1007/978-3-030-16800-1_3

53. Chen Z, Zhang W, Yang Z (2019) A review on cathode materials for advanced lithium ion batteries: microstructure designs and performance regulations. Nanotechnology 31 (1):012001. doi:10.1088/1361-6528/ab4447

54. Mohamed N, Allam NK (2020) Recent advances in the design of cathode materials for Li-ion batteries. RSC Advances 10 (37):21662-21685. doi:10.1039/D0RA03314F

55. Chen R, Zhao T, Zhang X, Li L, Wu F (2016) Advanced cathode materials for lithium-ion batteries using nanoarchitectonics. Nanoscale Horizons 1 (6):423-444. doi:10.1039/C6NH00016A

56. Writer B (2019) Cathode Materials, Samples, Pristine, Layered, Doping, Discharge Capacity. In: Lithium-Ion Batteries: A Machine-Generated Summary of Current Research. Springer International Publishing, Cham, pp 73-161. doi:10.1007/978-3-030-16800-1_2

57. K B, S V, Dhanush PC, K B, Nagaraja HS (2020) ZnWO4/SnO2@r-GO nanocomposite as an anode material for high capacity Lithium ion Battery. Electrochimica Acta:136676. doi:https://doi.org/10.1016/j.electacta.2020.136676

58. Pradeep N, Sivasenthil E, Janarthanan B, Sharmila S (2019) A Review of Anode Material for Lithium Ion Batteries. Journal of Physics: Conference Series 1362:012026. doi:10.1088/1742-6596/1362/1/012026

59. Lu J, Chen Z, Pan F, Cui Y, Amine K (2018) High-Performance Anode Materials for Rechargeable Lithium-Ion Batteries. Electrochemical Energy Reviews 1 (1):35-53. doi:10.1007/s41918-018-0001-4

60. Qi W, Shapter JG, Wu Q, Yin T, Gao G, Cui D (2017) Nanostructured anode materials for lithium-ion batteries: principle, recent progress and future perspectives. Journal of Materials Chemistry A 5 (37):19521-19540. doi:10.1039/C7TA05283A

61. Goriparti S, Miele E, De Angelis F, Di Fabrizio E, Proietti Zaccaria R, Capiglia C (2014) Review on recent progress of nanostructured anode materials for Li-ion batteries. Journal of Power Sources 257:421-443. doi:https://doi.org/10.1016/j.jpowsour.2013.11.103

62. Writer B (2019) Anode Materials, SEI, Carbon, Graphite, Conductivity, Graphene, Reversible, Formation. In: Lithium-Ion Batteries: A Machine-Generated Summary of Current Research. Springer International Publishing, Cham, pp 1-71. doi:10.1007/978-3-030-16800-1_1

63. Niu J, Kang S (2019) CHAPTER 1 New High-energy Anode Materials. In: Future Lithium-ion Batteries. The Royal Society of Chemistry, pp 1-25. doi:10.1039/9781788016124-00001

64. Lu Y, Yu L, Lou XW (2018) Nanostructured Conversion-type Anode Materials for Advanced Lithium-Ion Batteries. Chem 4 (5):972-996. doi:https://doi.org/10.1016/j.chempr.2018.01.003

65. Mahmood N, Tang T, Hou Y (2016) Nanostructured Anode Materials for Lithium Ion Batteries: Progress, Challenge and Perspective. Advanced Energy Materials 6 (17):1600374. doi:https://doi.org/10.1002/aenm.201600374

66. Vu A, Qian Y, Stein A (2012) Porous Electrode Materials for Lithium-Ion Batteries – How to Prepare Them and What Makes Them Special. Advanced Energy Materials 2 (9):1056-1085. doi:https://doi.org/10.1002/aenm.201200320

67. Subrahmanyam G, Ermanno M, Zaccaria RP, Claudio C (2018) Nanostructured anode materials. Physical Sciences Reviews 3 (11):20170149. doi:https://doi.org/10.1515/psr-2017-0149

68. Jeevanandam J, Barhoum A, Chan YS, Dufresne A, Danquah MK (2018) Review on nanoparticles and nanostructured materials: history, sources, toxicity and regulations. Beilstein J Nanotechnol 9:1050-1074. doi:10.3762/bjnano.9.98

69. Kaur M, Singh G, Khanna K, Kaur N (2015) Nanotechnology: A Review.

70. Ramsden JJ (2016) Chapter 1 - What is nanotechnology? In: Ramsden JJ (ed) Nanotechnology (Second Edition). William Andrew Publishing, Oxford, pp 1-18. doi:https://doi.org/10.1016/B978-0-323-39311-9.00007-8

71. Ramsden JJ (2016) Chapter 2 - The nanoscale. In: Ramsden JJ (ed) Nanotechnology (Second Edition). William Andrew Publishing, Oxford, pp 19-40. doi:https://doi.org/10.1016/B978-0-323-39311-9.00008-X

72. Mobasser S, Firoozi A (2016) Review of Nanotechnology Applications in Science and Engineering. Journal of Civil Engineering and Urbanism 6:84-93

73. Introduction (2010). In: Introduction to Nanoscience and Nanotechnology. pp 1-10. doi:https://doi.org/10.1002/9780470618837.ch

74. Benelmekki M (2015) An introduction to nanoparticles and nanotechnology. Designing Hybrid Nanoparticles. Morgan & Claypool Publishers. doi:10.1088/978-1-6270-5469-0ch1

75. Size Matters (2010). In: Introduction to Nanoscience and Nanotechnology. pp 11-32. doi:https://doi.org/10.1002/9780470618837.ch1

76. Murty BS, Shankar P, Raj B, Rath BB, Murday J (2013) Unique Properties of Nanomaterials. In: Textbook of Nanoscience and Nanotechnology. Springer Berlin Heidelberg, Berlin, Heidelberg, pp 29-65. doi:10.1007/978-3-642-28030-6_2

77. Nasrollahzadeh M, Issaabadi Z, Sajjadi M, Sajadi SM, Atarod M (2019) Chapter 2 - Types of Nanostructures. In: Nasrollahzadeh M, Sajadi SM, Sajjadi M, Issaabadi Z, Atarod M (eds) Interface Science and Technology, vol 28. Elsevier, pp 29-80. doi:https://doi.org/10.1016/B978-0-12-813586-0.00002-X

78. Bayda S, Adeel M, Tuccinardi T, Cordani M, Rizzolio F (2019) The History of Nanoscience and Nanotechnology: From Chemical-Physical Applications to Nanomedicine. Molecules 25 (1):112. doi:10.3390/molecules25010112

79. Schultze JW, Heidelberg A, Rosenkranz C, Schäpers T, Staikov G (2005) Principles of electrochemical nanotechnology and their application for materials and systems. Electrochimica Acta 51 (5):775-786. doi:https://doi.org/10.1016/j.electacta.2005.04.073

80. Lin Y, Nalwa HS (2009) Handbook of Electrochemical Nanotechnology.

81. Ashrit P (2017) Chapter 2. Introduction to Transition Metal Oxides and Thin Films. In. doi:10.1016/b978-0-08-101747-0.00002-7

82. Chapter 1 Introduction (1989). In: Kung HH (ed) Studies in Surface Science and Catalysis, vol 45. Elsevier, pp 1-5. doi:https://doi.org/10.1016/S0167-2991(08)60924-6

83. Jose Varghese R, Zikalala N, Sakho EHM, Oluwafemi OS (2020) 5 - Green synthesis protocol on metal oxide nanoparticles using plant extracts. In: Thomas S, Tresa Sunny A, Velayudhan P (eds) Colloidal Metal Oxide Nanoparticles. Elsevier, pp 67-82. doi:https://doi.org/10.1016/B978-0-12-813357-6.00006-1

84. Metal Oxide Nanoparticles. In: Encyclopedia of Inorganic and Bioinorganic Chemistry. doi:https://doi.org/10.1002/9781119951438.eibc0331

85. Niu L, Li Z, Xu Y, Sun J, Hong W, Liu X, Wang J, Yang S (2013) Simple Synthesis of Amorphous NiWO4 Nanostructure and Its Application as a Novel Cathode Material for Asymmetric Supercapacitors. ACS applied materials & interfaces 5. doi:10.1021/am402127u

86. Jiang Y, Liu B, Zhai Z, Liu X, Yang B, Liu L, Jiang X (2015) A general strategy toward the rational synthesis of metal tungstate nanostructures using plasma electrolytic oxidation method. Applied Surface Science 356:273-281. doi:https://doi.org/10.1016/j.apsusc.2015.08.080

87. Achary SN, Patwe SJ, Krishna PSR, Sindhe AB, Tyagi AK (2007) Crystal structure analysis of Scheelite and Zircon type thorium germanates: A neutron diffraction study. Journal of Alloys and Compounds 438 (1):274-278. doi:https://doi.org/10.1016/j.jallcom.2006.08.025

88. Siriwong P, Thongtem T, Phuruangrat A, Thongtem S (2011) Hydrothermal synthesis, characterization, and optical properties of wolframite ZnWO4 nanorods. CrystEngComm 13 (5):1564-1569. doi:10.1039/C0CE00402B

89. Chen J, Xu L, Li W, Gou X (2005) α-Fe2O3 Nanotubes in Gas Sensor and Lithium-Ion Battery Applications. Advanced Materials 17 (5):582-586. doi:https://doi.org/10.1002/adma.200401101

90. Guan H, Wang X, Li H, Zhi C, Zhai T, Bando Y, Golberg D (2012) CoO octahedral nanocages for high-performance lithium ion batteries. Chemical Communications 48 (40):4878-4880. doi:10.1039/C2CC30843F

91. Pan JH, Huang Q, Koh ZY, Neo D, Wang XZ, Wang Q (2013) Scalable Synthesis of Urchin- and Flowerlike Hierarchical NiO Microspheres and Their Electrochemical Property for Lithium Storage. ACS Applied Materials & Interfaces 5 (13):6292-6299. doi:10.1021/am401330g

92. Favors Z, Wang W, Bay HH, George A, Ozkan M, Ozkan CS (2014) Stable Cycling of SiO2 Nanotubes as High-Performance Anodes for Lithium-Ion Batteries. Scientific Reports 4 (1):4605. doi:10.1038/srep04605

93. Tang Y, Zhang Y, Deng J, Wei J, Tam HL, Chandran BK, Dong Z, Chen Z, Chen X (2014) Mechanical Force-Driven Growth of Elongated Bending TiO2-based Nanotubular Materials for Ultrafast Rechargeable Lithium Ion Batteries. Advanced Materials 26 (35):6111-6118. doi:https://doi.org/10.1002/adma.201402000

94. Su H, Xu Y-F, Feng S-C, Wu Z-G, Sun X-P, Shen C-H, Wang J-Q, Li J-T, Huang L, Sun S-G (2015) Hierarchical Mn2O3 Hollow Microspheres as Anode Material of Lithium Ion Battery and Its Conversion Reaction Mechanism Investigated by XANES. ACS Applied Materials & Interfaces 7 (16):8488-8494. doi:10.1021/am509198k

95. Yu X-Y, Wu HB, Yu L, Ma F-X, Lou XW (2015) Rutile TiO2 Submicroboxes with Superior Lithium Storage Properties. Angewandte Chemie International Edition 54 (13):4001-4004. doi:https://doi.org/10.1002/anie.201411353

96. Zhang W, Du L, Chen Z, Hong J, Yue L (2016) ZnO Nanocrystals as Anode Electrodes for Lithium-Ion Batteries. Journal of Nanomaterials 2016:8056302. doi:10.1155/2016/8056302

97. Li G-A, Li W-C, Chang W-C, Tuan H-Y (2016) Solution-grown GeO2 nanoparticles with a nearly 100% yield as lithium-ion battery anodes. RSC Advances 6 (101):98632-98638. doi:10.1039/C6RA20171G

98. Faramarzi MS, Abnavi A, Ghasemi S, Sanaee Z (2018) Nanoribbons of SnO2 as a high performance Li-ion battery anode material. Materials Research Express 5 (6):065040. doi:10.1088/2053-1591/aaca07

99. Zhang L, Song J, Liu Y, Yuan X, Guo S (2018) Tailoring nanostructured MnO2 as anodes for lithium ion batteries with high reversible capacity and initial Coulombic efficiency. Journal of Power Sources 379:68-73. doi:https://doi.org/10.1016/j.jpowsour.2018.01.024

100. dos Santos MC, Maynart MC, Aveiro LR, da Paz EC, dos Santos Pinheiro V (2017) Carbon-Based Materials: Recent Advances, Challenges, and Perspectives. In: Reference Module in Materials Science and Materials Engineering. Elsevier. doi:https://doi.org/10.1016/B978-0-12-803581-8.09262-6

101. Chung D (2017) Introduction to Carbon Composites. In. pp 88-160. doi:10.1016/B978-0-12-804459-9.00002-6

102. Ramsden JJ (2011) Chapter 9 - Carbon-Based Nanomaterials and Devices. In: Ramsden JJ (ed) Nanotechnology. William Andrew Publishing, Oxford, pp 189-197. doi:https://doi.org/10.1016/B978-0-08-096447-8.00009-0

103. Khan M, Tahir MN, Adil SF, Khan HU, Siddiqui MRH, Al-warthan AA, Tremel W (2015) Graphene based metal and metal oxide nanocomposites: synthesis, properties and their applications. Journal of Materials Chemistry A 3 (37):18753-18808. doi:10.1039/C5TA02240A

104. Hussain SZ, Ihrar M, Hussain SB, Oh WC, Ullah K (2020) A review on graphene based transition metal oxide composites and its application towards supercapacitor electrodes. SN Applied Sciences 2 (4):764. doi:10.1007/s42452-020-2515-8

105. Jeong GH, Lee S, Baek S, Kim S-W (2016) Recent trend of metal oxide/graphene composites for supercapacitive electrode materials. Chemistry - An Asian Journal 11:n/a-n/a. doi:10.1002/asia.201501072

106. Mallakpour S, Khadem E (2016) Carbon nanotube–metal oxide nanocomposites: Fabrication, properties and applications. Chemical Engineering Journal 302. doi:10.1016/j.cej.2016.05.038

107. Choi SH, Lee J-H, Kang YC (2015) Perforated Metal Oxide–Carbon Nanotube Composite Microspheres with Enhanced Lithium-Ion Storage Properties. ACS Nano 9 (10):10173-10185. doi:10.1021/acsnano.5b03822

108. Li J, Tang S, Lu L, Zeng HC (2007) Preparation of Nanocomposites of Metals, Metal Oxides, and Carbon Nanotubes via Self-Assembly. Journal of the American Chemical Society 129 (30):9401-9409. doi:10.1021/ja071122v

109. Zhou H, Zhang L, Zhang D, Chen S, Coxon PR, He X, Coto M, Kim H-K, Xi K, Ding S (2016) A universal synthetic route to carbon nanotube/transition metal oxide nano-composites for lithium ion batteries and electrochemical capacitors. Scientific Reports 6 (1):37752. doi:10.1038/srep37752

110. Luo Y, Wang K, Luo S, Zhao F, Wu H, Jiang K, Li Q, Fan S, Wang J (2018) Three-Dimensional Carbon Nanotube/Transition-Metal Oxide Sponges as Composite Electrodes with Enhanced Electrochemical Performance. ACS Applied Nano Materials 1 (6):2997-3005. doi:10.1021/acsanm.8b00606

111. Zhi M, Xiang C, Li J, Li M, Wu N (2013) Nanostructured carbon–metal oxide composite electrodes for supercapacitors: a review. Nanoscale 5 (1):72-88. doi:10.1039/C2NR32040A

112. Lin P, She Q, Hong B, Liu X, Shi Y, Shi, Univ ZX, Engn） D, Mat） C, Zheng M-S, Dong Q, 董全峰 (2010) The Nickel Oxide/CNT Composites with High Capacitance for Supercapacitor. Journal of The Electrochemical Society 157. doi:10.1149/1.3425624

113. Andersen N, Serov A, Atanassov P (2015) Metal oxides/CNT nano-composite catalysts for oxygen reduction/oxygen evolution in alkaline media. Applied Catalysis B: Environmental 163:623-627. doi:10.1016/j.apcatb.2014.08.033

114. Cheng Y, Jiang SP (2015) Advances in electrocatalysts for oxygen evolution reaction of water electrolysis-from metal oxides to carbon nanotubes. Progress in Natural Science: Materials International 25 (6):545-553. doi:https://doi.org/10.1016/j.pnsc.2015.11.008

115. Zheng M, Tang H, Hu Q, Zheng S, Li L, Xu J, Pang H (2018) Tungsten-Based Materials for Lithium-Ion Batteries. Advanced Functional Materials 28 (20):1707500. doi:https://doi.org/10.1002/adfm.201707500

116. Yang L, He X, Lv C, Jiang L, Wang B, Shu K (2016) One-step preparation and characterization of zinc tungstate–carbon nanoparticles with application to lithium-ion batteries. Instrumentation Science & Technology 44 (6):603-613. doi:10.1080/10739149.2016.1184160

117. Zhang W-M, Wu X-L, Hu J-S, Guo Y-G, Wan L-J (2008) Carbon Coated Fe3O4 Nanospindles as a Superior Anode Material for Lithium-Ion Batteries. Advanced Functional Materials 18 (24):3941-3946. doi:https://doi.org/10.1002/adfm.200801386

118. Zhang Y, Liu H, Zhu Z, Wong K-w, Mi R, Mei J, Lau W-m (2013) A green hydrothermal approach for the preparation of graphene/α-MnO2 3D network as anode for lithium ion battery. Electrochimica Acta 108:465-471. doi:https://doi.org/10.1016/j.electacta.2013.07.002

119. Song H, Li N, Cui H, Wang C (2014) Monodisperse SnO2 nanocrystals functionalized multiwalled carbon nanotubes for large rate and long lifespan anode materials in lithium ion batteries. Electrochimica Acta 120:46-51. doi:https://doi.org/10.1016/j.electacta.2013.12.052

120. Zhao Y, Chen G, Wang Y (2014) Facile Synthesis of Graphene/ZnO Composite as an Anode with Enhanced Performance for Lithium Ion Batteries. Journal of Nanomaterials 2014:964391. doi:10.1155/2014/964391

121. Jahel A, Darwiche A, Matei Ghimbeu C, Vix-Guterl C, Monconduit L (2014) High cycleability nano-GeO2/mesoporous carbon composite as enhanced energy storage anode material in Li-ion batteries. Journal of Power Sources 269:755-759. doi:https://doi.org/10.1016/j.jpowsour.2014.07.042

122. Ma Y, Sheng L, Zhao H, An K, Yu L, Xu J, Zhao X (2015) Synthesis of NiO/carbon shell/single-walled carbon nanotube composites as anode materials for lithium ion batteries. Solid State Sciences 46:49-55. doi:https://doi.org/10.1016/j.solidstatesciences.2015.05.014

123. Li W, Yoon D, Hwang J, Chang W, Kim J (2015) One-pot route to synthesize SnO2-Reduced graphene oxide composites and their enhanced electrochemical performance as anodes in lithium-ion batteries. Journal of Power Sources 293:1024-1031. doi:https://doi.org/10.1016/j.jpowsour.2015.06.025

124. He X, Hu Y, Shen Z, Chen R, Wu K, Cheng Z, Zhang XW, Pan P (2017) Channelized carbon nanofiber with uniform-dispersed GeO2 as anode for long-lifespan lithium-ion batteries. Journal of Alloys and Compounds 729:313-322. doi:https://doi.org/10.1016/j.jallcom.2017.09.038

125. Yin L-h, Wu M-b, Li Y-p, Wu G-l, Wang Y-k, Wang Y (2017) Synthesis of SiO2@carbon-graphene hybrids as anode materials of lithium-ion batteries. New Carbon Materials 32 (4):311-318. doi:https://doi.org/10.1016/S1872-5805(17)60124-0

126. Jo MS, Ghosh S, Jeong SM, Kang YC, Cho JS (2019) Coral-Like Yolk–Shell-Structured Nickel Oxide/Carbon Composite Microspheres for High-Performance Li-Ion Storage Anodes. Nano-Micro Letters 11 (1):3. doi:10.1007/s40820-018-0234-0

127. Rana M, Sai Avvaru V, Boaretto N, de la Peña O'Shea VA, Marcilla R, Etacheri V, Vilatela JJ (2019) High rate hybrid MnO2@CNT fabric anodes for Li-ion batteries: properties and a lithium storage mechanism study by in situ synchrotron X-ray scattering. Journal of Materials Chemistry A 7 (46):26596-26606. doi:10.1039/C9TA08800H

128. Chen D, Shen G, Tang K, Zheng H, Qian Y (2003) Low-temperature synthesis of metal tungstates nanocrystallites in ethylene glycol. Materials Research Bulletin 38 (14):1783-1789. doi:https://doi.org/10.1016/j.materresbull.2003.09.004

129. Parhi P, Karthik TN, Manivannan V (2008) Synthesis and characterization of metal tungstates by novel solid-state metathetic approach. Journal of Alloys and Compounds 465 (1):380-386. doi:https://doi.org/10.1016/j.jallcom.2007.10.089

130. Montini T, Gombac V, Hameed A, Felisari L, Adami G, Fornasiero P (2010) Synthesis, characterization and photocatalytic performance of transition metal tungstates. Chemical Physics Letters 498 (1):113-119. doi:https://doi.org/10.1016/j.cplett.2010.08.026

131. Shim H-W, Cho I-S, Hong KS, Lim A-H, Kim D-W (2011) Wolframite-type ZnWO4 Nanorods as New Anodes for Li-Ion Batteries. The Journal of Physical Chemistry C 115 (32):16228-16233. doi:10.1021/jp204656v

132. Wang X, Li B, Liu D, Xiong H (2014) ZnWO4 nanocrystals/reduced graphene oxide hybrids: Synthesis and their application for Li ion batteries. Science China Chemistry 57 (1):122-126. doi:10.1007/s11426-013-4983-9

133. Xing L-L, Yuan S, He B, Zhao Y-Y, Wu X-L, Xue X-Y (2013) Synergistic Effect of SnO2/ZnWO4 Core–Shell Nanorods with High Reversible Lithium Storage Capacity. Chemistry – An Asian Journal 8 (7):1530-1535. doi:10.1002/asia.201300337

134. Guan B, Hu L, Zhang G, Guo D, Fu T, Li J, Duan H, Li C, Li Q (2014) Facile synthesis of ZnWO4 nanowall arrays on Ni foam for high performance supercapacitors. RSC Advances 4 (9):4212-4217. doi:10.1039/C3RA45866K

135. Rao L, Xu J, Ao Y, Wang P (2014) In-situ growth of zinc tungstate nanorods on graphene for enhanced photocatalytic performance. Materials Research Bulletin 57:41-46. doi:https://doi.org/10.1016/j.materresbull.2014.05.006

136. Zhang L, Wang Z, Wang L, Xing Y, Li X, Zhang Y (2014) Electrochemical performance of ZnWO4/CNTs composite as anode materials for lithium-ion battery. Applied Surface Science 305:179-185. doi:https://doi.org/10.1016/j.apsusc.2014.03.035

137. Ede SR, Ramadoss A, Nithiyanantham U, Anantharaj S, Kundu S (2015) Bio-molecule Assisted Aggregation of ZnWO4 Nanoparticles (NPs) into Chain-like Assemblies: Material for High Performance Supercapacitor and as Catalyst for Benzyl Alcohol Oxidation. Inorganic Chemistry 54 (8):3851-3863. doi:10.1021/acs.inorgchem.5b00018

138. Yang Y, Zhu J, Shi W, Zhou J, Gong D, Gu S, Wang L, Xu Z, Lu B (2016) 3D nanoporous ZnWO4 nanoparticles with excellent electrochemical performances for supercapacitors. Materials Letters 177:34-38. doi:https://doi.org/10.1016/j.matlet.2016.04.168

139. Shi N, Xiong S, Wu F, Bai J, Chu Y, Mao H, Feng J, Xi B (2017) Hydrothermal Synthesis of ZnWO4 Hierarchical Hexangular Microstars for Enhanced Lithium-Storage Properties. European Journal of Inorganic Chemistry 2017 (3):734-740. doi:10.1002/ejic.201601225

140. Luo L, Liu T, Zhang S, Ke B, Yu L, Hussain S, Lin L (2017) Hierarchical Co3O4@ZnWO4 core/shell nanostructures on nickel foam: Synthesis and electrochemical performance for supercapacitors. Ceramics International 43 (6):5095-5101. doi:https://doi.org/10.1016/j.ceramint.2017.01.022

141. Anitha T, Reddy AE, Durga IK, Rao SS, Nam HW, Kim H-J (2019) Facile synthesis of ZnWO4@WS2 cauliflower-like structures for supercapacitors with enhanced electrochemical performance. Journal of Electroanalytical Chemistry 841:86-93. doi:https://doi.org/10.1016/j.jelechem.2019.04.034

142. Yesuraj J, Suthanthiraraj SA (2019) Bio-molecule templated hydrothermal synthesis of ZnWO4 nanomaterial for high-performance supercapacitor electrode application. Journal of Molecular Structure 1181:131-141. doi:https://doi.org/10.1016/j.molstruc.2018.12.087

143. Yang Y, Matsubara S, Xiong L, Hayakawa T, Nogami M (2007) Solvothermal Synthesis of Multiple Shapes of Silver Nanoparticles and Their SERS Properties. The Journal of Physical Chemistry C 111 (26):9095-9104. doi:10.1021/jp068859b

144. Zhang Y, Li L, Su H, Huang W, Dong X (2015) Binary metal oxide: advanced energy storage materials in supercapacitors. Journal of Materials Chemistry A 3 (1):43-59. doi:10.1039/C4TA04996A

145. Deng D (2015) Li-ion batteries: basics, progress, and challenges. Energy Science & Engineering 3 (5):385-418. doi:https://doi.org/10.1002/ese3.95

146. Xiao J, Li Q, Bi Y, Cai M, Dunn B, Glossmann T, Liu J, Osaka T, Sugiura R, Wu B, Yang J, Zhang J-G, Whittingham MS (2020) Understanding and applying coulombic efficiency in lithium metal batteries. Nature Energy 5 (8):561-568. doi:10.1038/s41560-020-0648-z

147. Günter FJ, Habedank JB, Schreiner D, Neuwirth T, Gilles R, Reinhart G (2018) Introduction to Electrochemical Impedance Spectroscopy as a Measurement Method for the Wetting Degree of Lithium-Ion Cells. Journal of The Electrochemical Society 165 (14):A3249-A3256. doi:10.1149/2.0081814jes

148. Zhao X, Wang G, Zhou Y, Wang H (2017) Flexible free-standing ternary CoSnO3/graphene/carbon nanotubes composite papers as anodes for enhanced performance of lithium-ion batteries. Energy 118:172-180. doi:https://doi.org/10.1016/j.energy.2016.12.018

149. Zhu G, Xu H, Wang H, Lu T, Pan L, Zhang L (2019) In situ growth of sandwich-like NiMoO4 nanowires/reduced graphene oxide hybrid for high-performance lithium storage. Ionics 25 (10):4577-4588. doi:10.1007/s11581-019-03016-2

150. Zheng M, Tang H, Li L, Hu Q, Zhang L, Xue H, Pang H (2018) Hierarchically Nanostructured Transition Metal Oxides for Lithium-Ion Batteries. Advanced Science 5 (3):1700592. doi:10.1002/advs.201700592

151. Roy P, Srivastava SK (2015) Nanostructured anode materials for lithium ion batteries. Journal of Materials Chemistry A 3 (6):2454-2484. doi:10.1039/C4TA04980B

152. Reddy MV, Subba Rao GV, Chowdari BVR (2013) Metal Oxides and Oxysalts as Anode Materials for Li Ion Batteries. Chemical Reviews 113 (7):5364-5457. doi:10.1021/cr3001884

153. Du L, Lin H, Ma Z, Wang Q, Li D, Shen Y, Zhang W, Rui K, Zhu J, Huang W (2019) Using and recycling V2O5 as high performance anode materials for sustainable lithium ion battery. Journal of Power Sources 424:158-164. doi:https://doi.org/10.1016/j.jpowsour.2019.03.103

154. Zhao J, Zhang Y, Wang Y, Li H, Peng Y (2018) The application of nanostructured transition metal sulfides as anodes for lithium ion batteries. Journal of Energy Chemistry 27 (6):1536-1554. doi:https://doi.org/10.1016/j.jechem.2018.01.009

155. Li Z, Li W, Xue H, Kang W, Yang X, Sun M, Tang Y, Lee C-S (2014) Facile fabrication and electrochemical properties of high-quality reduced graphene oxide/cobalt sulfide composite as anode material for lithium-ion batteries. RSC Advances 4 (70):37180-37186. doi:10.1039/C4RA06067A

156. Lopez J, Villarreal J, Cantu J, Parsons J, Alcoutlabi M (2018) Metal Sulfide/Carbon Composite Fibers as Anode Materials for Lithium Ion Batteries. ECS Transactions 85 (13):275-284. doi:10.1149/08513.0275ecst

157. HerÉDy LA, Lai S-C, McCoy LR, Saunders RC (1975) Metal Sulfide Electrodes for Secondary Lithium Batteries. In: New Uses of Sulfur, vol 140. Advances in Chemistry, vol 140. AMERICAN CHEMICAL SOCIETY, pp 203-215. doi:doi:10.1021/ba-1975-0140.ch013

10.1021/ba-1975-0140.ch013
158. Xu Q-T, Li J-C, Xue H-G, Guo S-P (2018) Binary iron sulfides as anode materials for rechargeable batteries: Crystal structures, syntheses, and electrochemical performance. Journal of Power Sources 379:41-52. doi:https://doi.org/10.1016/j.jpowsour.2018.01.022
159. Xue H, Jiao Q, Du J, Wang S, Feng C, Wu Q, Li H, Lu Q, Shi D, Zhao Y (2019) Hollow MoS2/rGO composites as high-performance anode materials for lithium-ion batteries. Ionics 25 (10):4659-4666. doi:10.1007/s11581-019-03041-1
160. Bhosale ME, Chae S, Kim JM, Choi J-Y (2018) Organic small molecules and polymers as an electrode material for rechargeable lithium ion batteries. Journal of Materials Chemistry A 6 (41):19885-19911. doi:10.1039/C8TA04906H
161. Zhou N, Dong H, Xu Y, Luo L, Zhao C, Wang D, Li H, Liu D (2018) Constructing inorganic/polymer microsphere composite as lithium ion battery anode material. Applied Surface Science 433:806-814. doi:https://doi.org/10.1016/j.apsusc.2017.10.125
162. Muench S, Wild A, Friebe C, Häupler B, Janoschka T, Schubert US (2016) Polymer-Based Organic Batteries. Chemical Reviews 116 (16):9438-9484. doi:10.1021/acs.chemrev.6b00070
163. Ulvestad A, Andersen HF, Jensen IJT, Mongstad TT, Mæhlen JP, Prytz Ø, Kirkengen M (2018) Substoichiometric Silicon Nitride – An Anode Material for Li-ion Batteries Promising High Stability and High Capacity. Scientific Reports 8 (1):8634. doi:10.1038/s41598-018-26769-8
164. Ulvestad A, Mæhlen JP, Kirkengen M (2018) Silicon nitride as anode material for Li-ion batteries: Understanding the SiNx conversion reaction. Journal of Power Sources 399:414-421. doi:https://doi.org/10.1016/j.jpowsour.2018.07.109
165. Rowsell JLC, Pralong V, Nazar LF (2001) Layered Lithium Iron Nitride: A Promising Anode Material for Li-Ion Batteries. Journal of the American Chemical Society 123 (35):8598-8599. doi:10.1021/ja0112745
166. de Guzman RC, Yang J, Ming-Cheng Cheng M, Salley SO, Ng KYS (2014) High capacity silicon nitride-based composite anodes for lithium ion batteries. Journal of Materials Chemistry A 2 (35):14577-14584. doi:10.1039/C4TA02596B
167. Wang L, Zhang K, Pan H, Wang L, Wang D, Dai W, Qin H, Li G, Zhang J (2018) 2D molybdenum nitride nanosheets as anode materials for improved lithium storage. Nanoscale 10 (40):18936-18941. doi:10.1039/C8NR05889J
168. Di Lecce D, Andreotti P, Boni M, Gasparro G, Rizzati G, Hwang J-Y, Sun Y-K, Hassoun J (2018) Multiwalled Carbon Nanotubes Anode in Lithium-Ion Battery with LiCoO2, Li[Ni1/3Co1/3Mn1/3]O2, and LiFe1/4Mn1/2Co1/4PO4 Cathodes. ACS Sustainable Chemistry & Engineering 6 (3):3225-3232. doi:10.1021/acssuschemeng.7b03395
169. Fan P, Liu H, Liao L, Fu J, Wang Z, Lv G, Mei L, Hao H, Xing J, Dong J (2017) Flexible and high capacity lithium-ion battery anode based on a carbon nanotube/electrodeposited nickel sulfide paper-like composite. RSC Advances 7 (78):49739-49744. doi:10.1039/C7RA08239H
170. Badi N (2016) Lithium-ion battery anodes of highly dispersed carbon nanotubes, graphene nanoplatelets, and carbon nanofibers. Journal of Materials Science: Materials in Electronics 27 (10):10342-10346. doi:10.1007/s10854-016-5119-8
171. de las Casas C, Li W (2012) A review of application of carbon nanotubes for lithium ion battery anode material. Journal of Power Sources 208:74-85. doi:https://doi.org/10.1016/j.jpowsour.2012.02.013

172. Zhang P, Ru Q, Gao Y, Yan H, Hou X, Chen F, Xianhua H, Zhao L (2019) Porous nano-silicon/TiO2/rGO@carbon architecture with 1000-cycling lifespan as superior durable anodes for lithium-ion batteries. Ionics 25:1-10. doi:10.1007/s11581-019-03050-0

173. Tang Q, Su H, Cui Y, Baker AP, Liu Y, Lu J, Song X, Zhang H, Wu J, Yu H, Qu D (2018) Ternary tin-based chalcogenide nanoplates as a promising anode material for lithium-ion batteries. Journal of Power Sources 379:182-190. doi:https://doi.org/10.1016/j.jpowsour.2018.01.051

174. Chen D, Ji G, Ding B, Ma Y, Qu B, Chen W, Lee JY (2014) Double Transition-Metal Chalcogenide as a High-Performance Lithium-Ion Battery Anode Material. Industrial & Engineering Chemistry Research 53 (46):17901-17908. doi:10.1021/ie503759v

175. Li P, Zhao G, Zheng X, Xu X, Yao C, Sun W, Dou SX (2018) Recent progress on silicon-based anode materials for practical lithium-ion battery applications. Energy Storage Materials 15:422-446. doi:https://doi.org/10.1016/j.ensm.2018.07.014

176. Ashuri M, He Q, Shaw LL (2016) Silicon as a potential anode material for Li-ion batteries: where size, geometry and structure matter. Nanoscale 8 (1):74-103. doi:10.1039/C5NR05116A

177. Yin S, Ji Q, Zuo X, Xie S, Fang K, Xia Y, Li J, Qiu B, Wang M, Ban J, Wang X, Zhang Y, Xiao Y, Zheng L, Liang S, Liu Z, Wang C, Cheng Y-J (2018) Silicon lithium-ion battery anode with enhanced performance: Multiple effects of silver nanoparticles. Journal of Materials Science & Technology 34 (10):1902-1911. doi:https://doi.org/10.1016/j.jmst.2018.02.004

178. Zhou X, Yin Y-X, Wan L-J, Guo Y-G (2012) Facile synthesis of silicon nanoparticles inserted into graphene sheets as improved anode materials for lithium-ion batteries. Chemical communications (Cambridge, England) 48:2198-2200. doi:10.1039/c2cc17061b

179. Bloom I, Dietz Rago N, Sheng Y, Li J, Wood DL, Steele LA, Lamb J, Spangler S, Grosso C, Fenton K (2019) Effect of overcharge on lithium-ion cells: Silicon/graphite anodes. Journal of Power Sources 432:73-81. doi:https://doi.org/10.1016/j.jpowsour.2019.05.080

180. Kim S-H, Lee D, Park C, Kim D-W (2018) Nanocrystalline silicon embedded in an alloy matrix as an anode material for high energy density lithium-ion batteries. Journal of Power Sources 395:328-335. doi:10.1016/j.jpowsour.2018.05.087

181. Xu R, Zhang K, Wei R, Yuan M, Zhang Y, Liang F, Yao Y (2020) High-capacity flour-based nano-Si/C composite anode materials for lithium-ion batteries. Ionics 26 (1):1-11. doi:10.1007/s11581-019-03224-w

182. Obrovac MN, Chevrier VL (2014) Alloy Negative Electrodes for Li-Ion Batteries. Chemical Reviews 114 (23):11444-11502. doi:10.1021/cr500207g

183. Zhang W-J (2011) A review of the electrochemical performance of alloy anodes for lithium-ion batteries. Journal of Power Sources 196 (1):13-24. doi:https://doi.org/10.1016/j.jpowsour.2010.07.020

184. Liang C, Gao M, Pan H, Liu Y, Yan M (2013) Lithium alloys and metal oxides as high-capacity anode materials for lithium-ion batteries. Journal of Alloys and Compounds 575:246-256. doi:https://doi.org/10.1016/j.jallcom.2013.04.001

185. Zhang J, Yu A (2015) Nanostructured transition metal oxides as advanced anodes for lithium-ion batteries. Science Bulletin 60 (9):823-838. doi:https://doi.org/10.1007/s11434-015-0771-6

186. Yan W, Liu X, Hou S, Wang X (2019) Study on micro-nanocrystalline structure control and performance of ZnWO4 photocatalysts. Catalysis Science & Technology 9 (5):1141-1153. doi:10.1039/C8CY02343C

187. Pereira PFS, Gouveia AF, Assis M, de Oliveira RC, Pinatti IM, Penha M, Gonçalves RF, Gracia L, Andrés J, Longo E (2018) ZnWO4 nanocrystals: synthesis, morphology, photoluminescence and photocatalytic properties. Physical Chemistry Chemical Physics 20 (3):1923-1937. doi:10.1039/C7CP07354B

188. Fu S, Hu H, Feng C, Zhang Y, Bi Y (2019) Epitaxial growth of ZnWO4 hole-storage nanolayers on ZnO photoanodes for efficient solar water splitting. Journal of Materials Chemistry A 7 (6):2513-2517. doi:10.1039/C8TA11263K

189. Tang Z, Li X, Yang J, Yu J, Wang J, Tang Z (2014) Mixed potential hydrogen sensor using ZnWO4 sensing electrode. Sensors and Actuators B: Chemical 195:520-525. doi:https://doi.org/10.1016/j.snb.2014.01.086

190. Arularasu MV, Sundaram R (2016) Synthesis and characterization of nanocrystalline ZnWO4-ZnO composites and their humidity sensing performance. Sensing and Bio-Sensing Research 11:20-25. doi:https://doi.org/10.1016/j.sbsr.2016.08.006

191. You L, Cao Y, Sun YF, Sun P, Zhang T, Du Y, Lu GY (2012) Humidity sensing properties of nanocrystalline ZnWO4 with porous structures. Sensors and Actuators B: Chemical 161 (1):799-804. doi:https://doi.org/10.1016/j.snb.2011.11.035

192. Brijesh K, Bindu K, Amudha A, Nagaraja H (2019) Dual electrochemical application of r-GO wrapped ZnWO4/Sb nanocomposite. Materials Research Express

193. Brijesh K, Bindu K, Shanbhag D, Nagaraja HS (2019) Chemically prepared Polypyrrole/ZnWO4 nanocomposite electrodes for electrocatalytic water splitting. International Journal of Hydrogen Energy 44 (2):757-767. doi:https://doi.org/10.1016/j.ijhydene.2018.11.022

194. Mohamed Jaffer Sadiq M, Mutyala S, Mathiyarasu J, Krishna Bhat D (2017) RGO/ZnWO4/Fe3O4 nanocomposite as an efficient electrocatalyst for oxygen reduction reaction. Journal of Electroanalytical Chemistry 799:102-110. doi:https://doi.org/10.1016/j.jelechem.2017.05.051

195. Brijesh K, Nagaraja HS (2019) Lower Band Gap Sb/ZnWO4@r-GO Nanocomposite Based Supercapacitor Electrodes. Journal of Electronic Materials 48 (7):4188-4195. doi:10.1007/s11664-019-07185-8

196. Sreejesh M, Huang NM, Nagaraja HS (2015) Solar Exfoliated Graphene and its Application in Supercapacitors and Electrochemical H2O2 Sensing. Electrochimica Acta 160:94-99. doi:https://doi.org/10.1016/j.electacta.2015.02.005

197. Li Z, Wu G, Liu D, Wu W, Jiang B, Zheng J, Li Y, Li J, Wu M (2014) Graphene enhanced carbon-coated tin dioxide nanoparticles for lithium-ion secondary batteries. Journal of Materials Chemistry A 2 (20):7471-7477. doi:10.1039/C4TA00361F

198. Osotsi MI, Macharia DK, Zhu B, Wang Z, Shen X, Liu Z, Zhang L, Chen Z (2018) Synthesis of ZnWO4–x nanorods with oxygen vacancy for efficient photocatalytic degradation of tetracycline. Progress in Natural Science: Materials International 28 (4):408-415. doi:https://doi.org/10.1016/j.pnsc.2018.01.007

199. Zhan S, Zhou F, Huang N, Liu Y, He Q, Tian Y, Yang Y, Ye F (2017) Synthesis of ZnWO4 Electrode with tailored facets: Deactivating the Microorganisms through Photoelectrocatalytic methods. Applied Surface Science 391:609-616. doi:https://doi.org/10.1016/j.apsusc.2016.06.137

200. Wang F, Li W, Gu S, Li H, Zhou H, Wu X (2015) Novel In2S3/ZnWO4 heterojunction photocatalysts: facile synthesis and high-efficiency visible-light-driven photocatalytic activity. RSC Advances 5 (109):89940-89950. doi:10.1039/C5RA16243B

201. Mohamed JS, Bhat DK (2017) Novel ZnWO4/RGO nanocomposite as high performance photocatalyst. AIMS Materials Science 4 (1):158-171. doi:http://dx.doi.org/10.3934/matersci.2017.1.158

202. Chen L, Xu Z, Li J, Zhou B, Shan M, Li Y, Liu L, Li B, Niu J (2014) Modifying graphite oxide nanostructures in various media by high-energy irradiation. RSC Advances 4 (2):1025-1031. doi:10.1039/C3RA46203J

203. Qu D (2014) Fundamental principals of battery design: Porous electrodes. AIP Conference Proceedings 1597 (1):14-25. doi:10.1063/1.4878477

204. Wu C-H, Pu N-W, Liu Y-M, Chen C-Y, Peng Y-Y, Cheng T-Y, Lin M-H, Ger M-D (2017) Improving rate capability of lithium-ion batteries using holey graphene as the anode material. Journal of the Taiwan Institute of Chemical Engineers 80:511-517. doi:https://doi.org/10.1016/j.jtice.2017.08.019

205. Tian R, Park S-H, King PJ, Cunningham G, Coelho J, Nicolosi V, Coleman JN (2019) Quantifying the factors limiting rate performance in battery electrodes. Nature Communications 10 (1):1933. doi:10.1038/s41467-019-09792-9

206. Cai X, Lai L, Shen Z, Lin J (2017) Graphene and graphene-based composites as Li-ion battery electrode materials and their application in full cells. Journal of Materials Chemistry A 5 (30):15423-15446. doi:10.1039/C7TA04354F

207. Zhang L, Wang Z, Wang L, Xing Y, Zhang Y (2013) Preparation of ZnWO4/graphene composites and its electrochemical properties for lithium-ion batteries. Materials Letters 108:9-12. doi:https://doi.org/10.1016/j.matlet.2013.06.094

208. Gong C, Bai Y-J, Feng J, Tang R, Qi Y-X, Lun N, Fan R-H (2013) Enhanced Electrochemical Performance of FeWO4 by Coating Nitrogen-Doped Carbon. ACS Applied Materials & Interfaces 5 (10):4209-4215. doi:10.1021/am400392t

209. Ilango PR, Prasanna K, Jo YN, Santhoshkumar P, Lee CW (2018) Wet chemical synthesis and characterization of nanocrystalline ZnWO4 for application in Li-ion batteries. Materials Chemistry and Physics 207:367-372. doi:https://doi.org/10.1016/j.matchemphys.2017.12.074

210. Shim H-W, Lim A-H, Lee G-H, Jung H-C, Kim D-W (2012) Fabrication of core/shell ZnWO4/carbon nanorods and their Li electroactivity. Nanoscale Research Letters 7 (1):9. doi:10.1186/1556-276x-7-9

211. Peng T, Liu C, Hou X, Zhang Z, Wang C, Yan H, Lu Y, Liu X, Luo Y (2017) Control Growth of Mesoporous Nickel Tungstate Nanofiber and Its Application as Anode Material for Lithium-Ion Batteries. Electrochimica Acta 224:460-467. doi:https://doi.org/10.1016/j.electacta.2016.11.154

212. Liu H, Wang G, Park J, Wang J, Liu H, Zhang C (2009) Electrochemical performance of α-Fe2O3 nanorods as anode material for lithium-ion cells. Electrochimica Acta 54 (6):1733-1736. doi:https://doi.org/10.1016/j.electacta.2008.09.071

213. Chien W-M, Chandra D, Joshua HL (2008) X-ray diffraction studies of Li-based complex hydrides after pressure cycling.

214. Lim S-Y (2019) Amorphous-silicon nanoshell on artificial graphite composite as the anode for lithium-ion battery. Solid State Sciences 93:24-30. doi:https://doi.org/10.1016/j.solidstatesciences.2019.05.002

215. He Z-K, Sun Q, Xie K, Lu P, Shi Z, Kamali AR (2019) Reactive molten salt synthesis of natural graphite flakes decorated with SnO2 nanorods as high performance, low cost anode material for lithium ion batteries. Journal of Alloys and Compounds 792:1213-1222. doi:https://doi.org/10.1016/j.jallcom.2019.04.022

216. Simsir H, Eltugral N, Frohnhoven R, Ludwig T, Gönüllü Y, Karagoz S, Mathur S (2018) Anode performance of hydrothermally grown carbon nanostructures and their molybdenum chalcogenides for Li-ion batteries. MRS Communications 8 (2):610-616. doi:10.1557/mrc.2018.71

217. Yu N, Zou L, Li C, Guo K (2019) In-situ growth of binder-free hierarchical carbon coated CoSe2 as a high performance lithium ion battery anode. Applied Surface Science 483:85-90. doi:https://doi.org/10.1016/j.apsusc.2019.03.258

218. Kim H, Nguyen QH, Kim IT, Hur J (2019) Scalable synthesis of high-performance molybdenum diselenide-graphite nanocomposite anodes for lithium-ion batteries. Applied Surface Science 481:1196-1205. doi:https://doi.org/10.1016/j.apsusc.2019.03.165

219. Yuan H, Kong L, Li T, Zhang Q (2017) A review of transition metal chalcogenide/graphene nanocomposites for energy storage and conversion. Chinese Chemical Letters 28 (12):2180-2194. doi:https://doi.org/10.1016/j.cclet.2017.11.038

220. Bai J, Wu H, Wang S, Zhang G, Feng C, Liu H (2019) Synthesis of CoSe2-SnSe2 nanocube-coated nitrogen-doped carbon (NC) as anode for lithium and sodium ion batteries. Applied Surface Science 488:512-521. doi:https://doi.org/10.1016/j.apsusc.2019.05.096

221. Jia N, Zhang M, Li B, Li C, Liu Y, Zhang Y, Yu T, Liu Y, Cui D, Tao X (2019) Ternary chalcogenide LiInSe2: A promising high-performance anode material for lithium ion batteries. Electrochimica Acta 320:134562. doi:https://doi.org/10.1016/j.electacta.2019.134562

222. Mei J, Liao T, Sun Z (2018) Two-dimensional metal oxide nanosheets for rechargeable batteries. Journal of Energy Chemistry 27 (1):117-127. doi:https://doi.org/10.1016/j.jechem.2017.10.012

223. Zhao J, Yao S, Hu C, Li Z, Wang J, Feng X (2019) Porous ZnO/Co3O4/CoO/Co composite derived from Zn-Co-ZIF as improved performance anodes for lithium-ion batteries. Materials Letters 250:75-78. doi:https://doi.org/10.1016/j.matlet.2019.04.104

224. Chen X, Huang Y, Zhang K, Feng X, Wang M (2018) Porous TiO2 nanobelts coated with mixed transition-metal oxides Sn3O4 nanosheets core-shell composites as high-performance anode materials of lithium ion batteries. Electrochimica Acta 259:131-142. doi:https://doi.org/10.1016/j.electacta.2017.10.180

225. Zhang Y, Lian F, Lu J, Ma L, Chen N, Chen Y, Xia D (2020) Identification of reversible insertion-type lithium storage reaction of manganese oxide with long cycle lifespan. Journal of Energy Chemistry 46 (2095-4956):144. doi:https://doi.org/10.1016/j.jechem.2019.10.022

226. Nagalakshmi M, Kalaiselvi N (2019) Mesoporous dominant cashewnut sheath derived bio-carbon anode for LIBs and SIBs. Electrochimica Acta 304:175-183. doi:https://doi.org/10.1016/j.electacta.2019.02.123

227. Zhang J, Liu G, Hu H, Wu L, Wang Q, Xin X, Li S, Lu P (2019) Graphene-like carbon-nitrogen materials as anode materials for Li-ion and mg-ion batteries. Applied Surface Science 487:1026-1032. doi:https://doi.org/10.1016/j.apsusc.2019.05.155

228. Sankar S, Saravanan S, Ahmed ATA, Inamdar AI, Im H, Lee S, Kim DY (2019) Spherical activated-carbon nanoparticles derived from biomass green tea wastes for anode material of lithium-ion battery. Materials Letters 240:189-192. doi:https://doi.org/10.1016/j.matlet.2018.12.143

229. Wu Z, Wang L, Huang J, Zou J, Chen S, Cheng H, Jiang C, Gao P, Niu X (2019) Loofah-derived carbon as an anode material for potassium ion and lithium ion batteries. Electrochimica Acta 306:446-453. doi:https://doi.org/10.1016/j.electacta.2019.03.165

230. Qu X, Huang G, Xing B, Si D, Xu B, Chen Z, Zhang C, Cao Y (2019) Core-shell carbon composite material as anode materials for lithium-ion batteries. Journal of Alloys and Compounds 772:814-822. doi:https://doi.org/10.1016/j.jallcom.2018.09.036

231. Zheng H, Qu Q, Zhang L, Liu G, Battaglia VS (2012) Hard carbon: a promising lithium-ion battery anode for high temperature applications with ionic electrolyte. RSC Advances 2 (11):4904-4912. doi:10.1039/C2RA20536J

232. He J, Wang N, Cui Z, Du H, Fu L, Huang C, Yang Z, Shen X, Yi Y, Tu Z, Li Y (2017) Hydrogen substituted graphdiyne as carbon-rich flexible electrode for lithium and sodium ion batteries. Nature Communications 8 (1):1172. doi:10.1038/s41467-017-01202-2

233. Dong C, Guo L, He Y, Chen C, Qian Y, Chen Y, Xu L (2018) Sandwich-like Ni2P nanoarray/nitrogen-doped graphene nanoarchitecture as a high-performance anode for sodium and lithium ion batteries. Data Brief 20:1999-2002. doi:10.1016/j.dib.2018.08.158

234. Wang J, Deng Q, Li M, Jiang K, Zhang J, Hu Z, Chu J (2017) Copper ferrites@reduced graphene oxide anode materials for advanced lithium storage applications. Scientific Reports 7 (1):8903. doi:10.1038/s41598-017-09214-0

235. Islam M, Ali G, Jeong M-G, Choi W, Chung KY, Jung H-G (2017) Study on the Electrochemical Reaction Mechanism of NiFe2O4 as a High-Performance Anode for Li-Ion Batteries. ACS Applied Materials & Interfaces 9 (17):14833-14843. doi:10.1021/acsami.7b01892

236. Luo L, Li D, Zang J, Chen C, Zhu J, Qiao H, Cai Y, Lu K, Zhang X, Wei Q (2017) Carbon-Coated Magnesium Ferrite Nanofibers for Lithium-Ion Battery Anodes with Enhanced Cycling Performance. Energy Technology 5 (8):1364-1372. doi:10.1002/ente.201600686

237. Karthigayan N, Manimuthu P, Priya M, Sagadevan S (2017) Synthesis and characterization of NiFe2O4, CoFe2O4 and CuFe2O4 thin films for anode material in Li-ion batteries. Nanomaterials and Nanotechnology 7:1847980417711084. doi:10.1177/1847980417711084

238. Chu Y-Q, Fu Z-W, Qin Q-Z (2004) Cobalt ferrite thin films as anode material for lithium ion batteries. Electrochimica Acta 49 (27):4915-4921. doi:https://doi.org/10.1016/j.electacta.2004.06.012

239. Salah M, Murphy P, Hall C, Francis C, Kerr R, Fabretto M (2019) Pure silicon thin-film anodes for lithium-ion batteries: A review. Journal of Power Sources 414:48-67. doi:https://doi.org/10.1016/j.jpowsour.2018.12.068

240. Lin G, Wang H, Zhang L, Cheng Q, Gong Z, Ostrikov K (2019) Graphene nanowalls conformally coated with amorphous/ nanocrystalline Si as high-performance binder-free nanocomposite anode for lithium-ion batteries. Journal of Power Sources 437:226909. doi:https://doi.org/10.1016/j.jpowsour.2019.226909

241. Chen T, Wu J, Zhang Q, Su X (2017) Recent advancement of SiOx based anodes for lithium-ion batteries. Journal of Power Sources 363:126-144. doi:https://doi.org/10.1016/j.jpowsour.2017.07.073

242. Domi Y, Usui H, Yamaguchi K, Yodoya S, Sakaguchi H (2019) Silicon-Based Anodes with Long Cycle Life for Lithium-Ion Batteries Achieved by Significant Suppression of Their Volume Expansion in Ionic-Liquid Electrolyte. ACS Applied Materials & Interfaces 11 (3):2950-2960. doi:10.1021/acsami.8b17123

243. An W, Gao B, Mei S, Xiang B, Fu J, Wang L, Zhang Q, Chu PK, Huo K (2019) Scalable synthesis of ant-nest-like bulk porous silicon for high-performance lithium-ion battery anodes. Nature Communications 10 (1):1447. doi:10.1038/s41467-019-09510-5

244. Ette PM, Bhargav PB, Ahmed N, Chandra B, Rayarfrancis A, Ramesha K (2020) Nanocrystalline silicon embedded highly conducting phosphorus doped silicon thin film as high power lithium ion battery anode. Electrochimica Acta 330:135318. doi:https://doi.org/10.1016/j.electacta.2019.135318

245. Chen Y, Li Y, Wang Y, Fu K, Danner VA, Dai J, Lacey SD, Yao Y, Hu L (2016) Rapid, in Situ Synthesis of High Capacity Battery Anodes through High Temperature Radiation-Based Thermal Shock. Nano Letters 16 (9):5553-5558. doi:10.1021/acs.nanolett.6b02096

246. Amin K, Mao L, Wei Z (2019) Recent Progress in Polymeric Carbonyl-Based Electrode Materials for Lithium and Sodium Ion Batteries. Macromolecular Rapid Communications 40 (1):1800565. doi:10.1002/marc.201800565

247. Li C, Hu X, Lou X, Chen Q, Hu B (2016) Bimetallic coordination polymer as a promising anode material for lithium-ion batteries. Chemical Communications 52 (10):2035-2038. doi:10.1039/C5CC07151H

248. Fang M, Yao X, Li W, Li Y, Shui M, Shu J (2018) The investigation of lithium doping perovskite oxide LiMnO3 as possible LIB anode material. Ceramics International 44 (7):8223-8231. doi:https://doi.org/10.1016/j.ceramint.2018.02.002

249. Vicente N, Garcia-Belmonte G (2017) Methylammonium Lead Bromide Perovskite Battery Anodes Reversibly Host High Li-Ion Concentrations. The Journal of Physical Chemistry Letters 8 (7):1371-1374. doi:10.1021/acs.jpclett.7b00189

250. Kostopoulou A, Vernardou D, Savva K, Stratakis E (2019) All-inorganic lead halide perovskite nanohexagons for high performance air-stable lithium batteries. Nanoscale 11 (3):882-889. doi:10.1039/C8NR10009H

251. Wang Q, Yang T, Wang H, Zhang J, Guo X, Yang Z, Lu S, Qin W (2019) Morphological and chemical tuning of lead halide perovskite mesocrystals as long-life anode materials in lithium-ion batteries. CrystEngComm 21 (6):1048-1059. doi:10.1039/C8CE01779D

252. Veerappan G, SunyoungYoo, Zhang K, Ma M, Kang B, Park JH (2016) High-reversible capacity of Perovskite BaSnO3/rGO composite for Lithium-Ion Battery Anodes. Electrochimica Acta 214:31-37. doi:https://doi.org/10.1016/j.electacta.2016.07.076

253. Zhu S, Liu J, Sun J (2019) Growth of ultrathin SnO2 on carbon nanotubes by atomic layer deposition and their application in lithium ion battery anodes. Applied Surface Science 484:600-609. doi:https://doi.org/10.1016/j.apsusc.2019.04.163

254. Li H, Su Q, Kang J, Huang M, Feng M, Feng H, Huang P, Du G (2018) Porous SnO2 hollow microspheres as anodes for high-performance lithium ion battery. Materials Letters 217:276-280. doi:https://doi.org/10.1016/j.matlet.2018.01.015

255. Li Z, Pan H, Wei W, Dong A, Zhang K, Lv H, He X (2019) Bismuth metal–organic frameworks derived bismuth selenide nanosheets/nitrogen–doped carbon hybrids as anodes for Li–ion batteries with improved cyclic performance. Ceramics International 45 (9):11861-11867. doi:https://doi.org/10.1016/j.ceramint.2019.03.068

256. Cui D, Zheng Z, Peng X, Li T, Sun T, Yuan L (2017) Fluorine-doped SnO2 nanoparticles anchored on reduced graphene oxide as a high-performance lithium ion battery anode. Journal of Power Sources 362:20-26. doi:https://doi.org/10.1016/j.jpowsour.2017.07.024

257. Sun L, Si H, Zhang Y, Shi Y, Wang K, Liu J, Zhang Y (2019) Sn-SnO2 hybrid nanoclusters embedded in carbon nanotubes with enhanced electrochemical performance for advanced lithium ion batteries. Journal of Power Sources 415:126-135. doi:https://doi.org/10.1016/j.jpowsour.2019.01.063

258. Huang B, Pan Z, Su X, An L (2018) Tin-based materials as versatile anodes for alkali (earth)-ion batteries. Journal of Power Sources 395:41-59. doi:https://doi.org/10.1016/j.jpowsour.2018.05.063

259. Wang L, Han J, Kong D, Tao Y, Yang Q-H (2019) Enhanced Roles of Carbon Architectures in High-Performance Lithium-Ion Batteries. Nano-Micro Letters 11 (1):5. doi:10.1007/s40820-018-0233-1

260. Kuribayashi I, Yokoyama M, Yamashita M (1995) Battery characteristics with various carbonaceous materials. Journal of Power Sources 54 (1):1-5. doi:https://doi.org/10.1016/0378-7753(94)02030-7

261. Brijesh K, Nagaraja HS (2020) ZnWO4/r-GO nanocomposite as high capacity anode for lithium-ion battery. Ionics. doi:10.1007/s11581-020-03480-1

262. Amudha A, Shashikala HD, Asiq Rahman OS, Keshri AK, Nagaraja HS (2019) Effect of graphene oxide loading on plasma sprayed alumina-graphene oxide composites for improved anticorrosive and hydrophobic surface. Surface Topography: Metrology and Properties 7 (2):024003. doi:10.1088/2051-672x/ab2707

263. Brijesh K, Bindu K, Shanbhag D, Nagaraja HS (2018) Chemically prepared Polypyrrole/ZnWO4 nanocomposite electrodes for electrocatalytic water splitting. International Journal of Hydrogen Energy. doi:https://doi.org/10.1016/j.ijhydene.2018.11.022

264. Li M, Meng Q, Li S, Li F, Zhu Q, Kim B-N, Li J-G (2019) Photoluminescent and photocatalytic ZnWO4 nanorods via controlled hydrothermal reaction. Ceramics International 45 (8):10746-10755. doi:https://doi.org/10.1016/j.ceramint.2019.02.148

265. Minh NV, Hung NM, Xuan Thao DT, Roeffaers M, Hofkens J (2013) Structural and Optical Properties of ZnWO4:Er3+ Crystals. Journal of Spectroscopy 2013:424185. doi:10.1155/2013/424185

266. Rumyantseva MN, Gaskov AM, Rosman N, Pagnier T, Morante JR (2005) Raman Surface Vibration Modes in Nanocrystalline SnO2: Correlation with Gas Sensor Performances. Chemistry of Materials 17 (4):893-901. doi:10.1021/cm0490470

267. Li W, Guo J, Cai L, Qi W, Sun Y, Xu J-L, Sun M, Zhu H, Xiang L, Xie D, Ren T (2019) UV light irradiation enhanced gas sensor selectivity of NO2 and SO2 using rGO functionalized with hollow SnO2 nanofibers. Sensors and Actuators B: Chemical 290:443-452. doi:https://doi.org/10.1016/j.snb.2019.03.133

268. Stefanov P, Atanasova G, Manolov E, Raicheva Z, Lazarova V (2008) Preparation and characterization of SnO2films for sensing applications. Journal of Physics: Conference Series 100 (8):082046. doi:10.1088/1742-6596/100/8/082046

269. Jiang S, Huang R, Zhu W, Li X, Zhao Y, Gao Z, Gao L, Zhao J (2019) Free-Standing SnO2@rGO Anode via the Anti-solvent-assisted Precipitation for Superior Lithium Storage Performance. Frontiers in Chemistry 7 (878). doi:10.3389/fchem.2019.00878

270. Song D, Wang S, Liu R, Jiang J, Jiang Y, Huang S, Li W, Chen Z, Zhao B (2019) Ultra-small SnO2 nanoparticles decorated on three-dimensional nitrogen-doped graphene aerogel for high-performance bind-free anode material. Applied Surface Science 478:290-298. doi:https://doi.org/10.1016/j.apsusc.2019.01.143

271. Nowak AP (2018) Composites of tin oxide and different carbonaceous materials as negative electrodes in lithium-ion batteries. Journal of Solid State Electrochemistry 22 (8):2297-2304. doi:10.1007/s10008-018-3942-y

272. Pei M, Wu Y, Qi Z, Mei D (2020) Synthesis and electrochemical performance of NiO/Fe3O4/rGO as anode material for lithium ion battery. Ionics. doi:10.1007/s11581-020-03545-1

273. Liu G, Sun W-j, Tang S-s, Liang S-q, Liu J (2015) Synthesis of α-Fe2O3@SnO2 core-shell nanoparticles via low-temperature molten salt reaction route. Transactions of Nonferrous Metals Society of China 25 (11):3651-3656. doi:https://doi.org/10.1016/S1003-6326(15)64076-6

274. Gu C, Guan W, Shim J-J, Fang Z, Huang J (2017) Size-controlled synthesis and electrochemical performance of porous Fe2O3/SnO2 nanocubes as an anode material for lithium ion batteries. CrystEngComm 19 (4):708-715. doi:10.1039/C6CE02288J

275. Yang H, Song T, Lee S, Han H, Xia F, Devadoss A, Sigmund W, Paik U (2013) Tin indium oxide/graphene nanosheet nanocomposite as an anode material for lithium ion batteries with enhanced lithium storage capacity and rate capability. Electrochimica Acta 91:275-281. doi:https://doi.org/10.1016/j.electacta.2012.12.070

276. Deng Y, Tang S, Zhang Q, Shi Z, Zhang L, Zhan S, Chen G (2011) Controllable synthesis of spinel nano-ZnMn2O4via a single source precursor route and its high capacity retention as anode material for lithium ion batteries. Journal of Materials Chemistry 21 (32):11987-11995. doi:10.1039/C1JM11575H

277. Sreejesh M, Shenoy S, Sridharan K, Kufian D, Arof AK, Nagaraja HS (2017) Melt quenched vanadium oxide embedded in graphene oxide sheets as composite electrodes for amperometric dopamine sensing and lithium ion battery applications. Applied Surface Science 410:336-343. doi:https://doi.org/10.1016/j.apsusc.2017.02.246

278. Fang S, Bresser D, Passerini S (2020) Transition Metal Oxide Anodes for Electrochemical Energy Storage in Lithium- and Sodium-Ion Batteries. Advanced Energy Materials 10 (1):1902485. doi:10.1002/aenm.201902485

279. Beitollahi H, Movahedifar F, Tajik S, Jahani S (2019) A Review on the Effects of Introducing CNTs in the Modification Process of Electrochemical Sensors. Electroanalysis 31 (7):1195-1203. doi:10.1002/elan.201800370

280. Deng X, Li J, Ma L, Sha J, Zhao N (2019) Three-dimensional porous carbon materials and their composites as electrodes for electrochemical energy storage systems. Materials Chemistry Frontiers 3 (11):2221-2245. doi:10.1039/C9QM00425D

281. Liu Y, Wang J, Xu Y, Zhu Y, Bigio D, Wang C (2014) Lithium–tellurium batteries based on tellurium/porous carbon composite. Journal of Materials Chemistry A 2 (31):12201-12207. doi:10.1039/C4TA02075H

282. Gu X, Tang T, Liu X, Hou Y (2019) Rechargeable metal batteries based on selenium cathodes: progress, challenges and perspectives. Journal of Materials Chemistry A 7 (19):11566-11583. doi:10.1039/C8TA12537F

283. Zhou H, Li X, Li Y, Zheng M, Pang H (2019) Applications of MxSey (M = Fe, Co, Ni) and Their Composites in Electrochemical Energy Storage and Conversion. Nano-Micro Letters 11 (1):40. doi:10.1007/s40820-019-0272-2

284. Yue B, Hu Q, Ji L, Wang Y, Liu J (2019) Facile synthesis of perovskite CeMnO3 nanofibers as an anode material for high performance lithium-ion batteries. RSC Advances 9 (65):38271-38279. doi:10.1039/C9RA07660C

285. Zhang C, Wu C, Zhang Z, Shen Y, Liu W (2020) LaNiO3 as a Novel Anode for Lithium-Ion Batteries. Transactions of Tianjin University 26 (2):142-147. doi:10.1007/s12209-020-00232-0

286. Wei G, Wei L, Wang D, Chen Y, Tian Y, Yan S, Mei L, Jiao J (2017) Reversible control of the magnetization of spinel ferrites based electrodes by lithium-ion migration. Scientific Reports 7 (1):12554. doi:10.1038/s41598-017-12948-6

287. Liu Z, Yu Q, Zhao Y, He R, Xu M, Feng S, Li S, Zhou L, Mai L (2019) Silicon oxides: a promising family of anode materials for lithium-ion batteries. Chemical Society Reviews 48 (1):285-309. doi:10.1039/C8CS00441B

288. Silicon anode supported by carbon scaffold for high performance lithium ion micro-battery (2015). MEMS 2015:130

289. Wang H, Lin J, Shen ZX (2016) Polyaniline (PANi) based electrode materials for energy storage and conversion. Journal of Science: Advanced Materials and Devices 1 (3):225-255. doi:https://doi.org/10.1016/j.jsamd.2016.08.001

290. Yoon S, Jung S-H, Jung K-N, Woo S-G, Cho W, Jo Y-N, Cho KY (2016) Preparation of nanostructured Ge/GeO2 composite in carbon matrix as an anode material for lithium-ion batteries. Electrochimica Acta 188:120-125. doi:https://doi.org/10.1016/j.electacta.2015.11.132

291. Lim S-Y, Jang W, Yun S, Yoon W-S, Choi J-Y, Whang D (2019) Amorphous germanium oxide nanobubbles for lithium-ion battery anode. Materials Research Bulletin 110:24-31. doi:https://doi.org/10.1016/j.materresbull.2018.10.007

292. Wei W, Xu J, Xu M, Zhang S, Guo L (2018) Recent progress on Ge oxide anode materials for lithium-ion batteries. Science China Chemistry 61 (5):515-525. doi:10.1007/s11426-018-9244-0

293. Wei W, Jia F, Qu P, Huang Z, Wang H, Guo L (2017) Morphology memory but reconstructing crystal structure: porous hexagonal GeO2 nanorods for rechargeable lithium-ion batteries. Nanoscale 9 (11):3961-3968. doi:10.1039/C7NR00599G

294. Wang X-L, Han W-Q, Chen H, Bai J, Tyson TA, Yu X-Q, Wang X-J, Yang X-Q (2011) Amorphous Hierarchical Porous GeOx as High-Capacity Anodes for Li Ion Batteries with Very Long Cycling Life. Journal of the American Chemical Society 133 (51):20692-20695. doi:10.1021/ja208880f

295. Li L, Yang H, Zhou D, Zhou Y (2014) Progress in application of CNTs in lithium-ion batteries. J Nanomaterials 2014:Article 9. doi:10.1155/2014/187891

296. Liu X-M, Huang Zd, Oh Sw, Zhang B, Ma P-C, Yuen MMF, Kim J-K (2012) Carbon nanotube (CNT)-based composites as electrode material for rechargeable Li-ion batteries: A review. Composites Science and Technology 72 (2):121-144. doi:https://doi.org/10.1016/j.compscitech.2011.11.019

297. Wu GT (1999) Structure and Lithium Insertion Properties of Carbon Nanotubes. Journal of The Electrochemical Society 146 (5):1696. doi:10.1149/1.1391828

298. Liu B, Abouimrane A, Balasubramanian M, Ren Y, Amine K (2014) GeO2–SnCoC Composite Anode Material for Lithium-Ion Batteries. The Journal of Physical Chemistry C 118 (8):3960-3967. doi:10.1021/jp411462v

299. Choi SH, Lee SJ, Kim HJ, Park SB, Choi JW (2018) Li2O–B2O3–GeO2 glass as a high performance anode material for rechargeable lithium-ion batteries. Journal of Materials Chemistry A 6 (16):6860-6866. doi:10.1039/C8TA00934A

300. Brijesh K, Dhanush PC, Vinayraj S, Nagaraja HS (2020) Monoclinic Wolframite ZnWO4/SiO2 nanocomposite as an anode material for lithium ion battery. Materials Letters 275:128108. doi:https://doi.org/10.1016/j.matlet.2020.128108

301. Giri PK, Dhara S (2012) Freestanding Ge/GeO2 core-shell nanocrystals with varying sizes and shell thicknesses: microstructure and photoluminescence studies. J Nanomaterials 2012:Article 6. doi:10.1155/2012/905178

302. Wu M-S, Zheng Z-B, Lai Y-S, Jow J-J (2015) Nickel cobaltite nanograss grown around porous carbon nanotube-wrapped stainless steel wire mesh as a flexible electrode for high-performance supercapacitor application. Electrochimica Acta 182:31-38. doi:https://doi.org/10.1016/j.electacta.2015.09.049

303. Venkataraman A, Amadi EV, Chen Y, Papadopoulos C (2019) Carbon Nanotube Assembly and Integration for Applications. Nanoscale Research Letters 14 (1):220. doi:10.1186/s11671-019-3046-3

304. Kajita T, Itoh T (2016) Electrochemical Performance of Amorphous GeOxPowder Synthesized by Oxidation of NaGe Serving as an Anode for Lithium Ion Batteries. Journal of The Electrochemical Society 163 (3):A552-A556. doi:10.1149/2.0931603jes

305. Wei W, Tian A, Jia F, Wang K, Qu P, Xu M (2016) Green synthesis of GeO2/graphene composites as anode material for lithium-ion batteries with high capacity. RSC Advances 6 (90):87440-87445. doi:10.1039/C6RA14819K

306. Zhou M, Gordin ML, Chen S, Xu T, Song J, Lv D, Wang D (2013) Enhanced performance of SiO/Fe2O3 composite as an anode for rechargeable Li-ion batteries. Electrochemistry Communications 28:79-82. doi:https://doi.org/10.1016/j.elecom.2012.12.013

307. Favors Z, Wang W, Bay HH, George A, Ozkan M, Ozkan CS (2014) Stable Cycling of SiO2 Nanotubes as High-Performance Anodes for Lithium-Ion Batteries. Scientific Reports 4:4605. doi:10.1038/srep04605

308. Miyachi M, Yamamoto H, Kawai H, Ohta T, Shirakata M (2005) Analysis of SiO Anodes for Lithium-Ion Batteries. Journal of The Electrochemical Society 152 (10):A2089. doi:10.1149/1.2013210

LIST OF PUBLICATIONS AND CONFERENCES

PEER-REVIEWED JOURNAL PUBLICATIONS

1. **K Brijesh**, K Bindu, Dhanush Shanbhag, HS Nagaraja "Chemically prepared Polypyrrole/ZnWO4 nanocomposite electrodes for electrocatalytic water splitting", International Journal of Hydrogen Energy 44 (2) (2019) 757-767. DOI link: https://doi.org/10.1016/j.ijhydene.2018.11.022

2. **K Brijesh**, HS Nagaraja, "Lower Band Gap Sb/ZnWO4/r-GO Nanocomposite Based Supercapacitor Electrodes" Journal of Electronic Materials 48 (7), 4188-4195 (2019). DOI link: https://doi.org/10.1007/s11664-019-07185-8

3. **K Brijesh**, K Bindu, A Amudha, HS Nagaraja, "Dual electrochemical application of r-GO wrapped ZnWO4/Sb nanocomposite" Materials Research Express 6 (11), 115030 (2019) DOI link: https://doi.org/10.1088/2053-1591/ab4644

4. **K Brijesh**, HS Nagaraja, "ZnWO4/r-GO nanocomposite as high capacity anode for lithium-ion battery", Ionics (2020) DOI link: https://doi.org/10.1007/s11581-020-03480-1

5. **K Brijesh**, PC Dhanush, S Vinayraj, HS Nagaraja, "Monoclinic Wolframite ZnWO4/SiO2 nanocomposite as an anode material for Lithium ion Battery" Materials Letters, 128108 (2020). DOI link: https://doi.org/10.1016/j.matlet.2020.128108

6. PC Dhanush, **K Brijesh**, S Vinayraj, HS Nagaraja, "High stable zinc tungstate electrode for electrochemical supercapacitor", AIP Conference Proceedings 2247 (1), 040011 (2020). DOI link : https://doi.org/10.1063/5.0004023

7. **K Brijesh**, S Vinayraj, PC Dhanush, K Bindu, HS Nagaraja, "ZnWO4/SnO2@ r-GO nanocomposite as an anode material for high capacity lithium ion battery", Electrochimica Acta 354, 136676 (2020). DOI link: https://doi.org/10.1016/j.electacta.2020.136676

8. **K Brijesh**, HS Nagaraja, "GeO2/ZnWO4@CNT nanocomposite as a novel anode material for lithium-ion battery" Journal of Solid State Electrochemistry 24 (10), 2525-2533 (2020). DOI link: https://doi.org/10.1007/s10008-020-04798-6

9. S Vinayaraj, **K Brijesh**, PC Dhanush, HS Nagaraja, "ZnWO4/SnO2 composite for supercapacitor applications", Physica B: Condensed Matter 596, 412369 (2020). DOI link: https://doi.org/10.1016/j.physb.2020.412369

10. **K. Brijesh**, M. K. Prajil and H. S. Nagaraja, "Fabrication of AgWO4/CNT nanomaterial for high capacity lithium-ion battery", Materials Technology (2020) DOI link: 10.1080/10667857.2020.1859051

WORKSHOP AND CONFERENCE ATTENDED

1. JNCASR-I2CAM School-2017 on Clean and Renewable Energy Technologies via Chemical Route held at JNCASR on 27th November - 2nd December 2017

2. International conference on Nanotechnology: Ideas Innovations & Initiatives -2017 held from December 06 - 08, 2017 at IIT Roorkee

3. International Conference on "Nanotechnology for Better Living" NBL-2019 held at NIT Srinagar in collaboration with IIT Kharagpur on 7-11 April, 2019.

4. SECOND INTERNATIONAL CONFERENCE ON DESIGN, MATERIALS & MANUFACTURE, ICDEM 2019, December 6-8, 2019 held at National Institute of Technology Karnataka, Surathkal

5. International Conference on "Current Trends in Functional Materials" on 15-17th January 2020 held at National Institute of Technology Karnataka

CURRICULUM VITAE

Brijesh K

Research Scholar

Department of Physics

National Institute of Technology Karnataka, Surathkal

Mangalore – 575 025, India.

Mobile: 9164585090

Email: brijeshphy89@gmail.com

Education qualification:

- o **Ph.D. Physics** (2016-present): National Institute of Technology Karnataka (NITK), Surathkal, India.
- o **M.Sc. Physics**, (2013), Mangalore University, India.
- o **B.Sc. Physics, Computer science and Mathematics** (2011) Mangalore University, India.